The intrinsically disordered cytoplasmic tail of a dendrite branching receptor uses two distinct mechanisms to regulate the actin cytoskeleton

Daniel A. Kramer[1], Heidy Y. Narvaez-Ortiz[2], Urval Patel[1], Rebecca Shi[3,4], Kang Shen[3,5], Brad J. Nolen[2], Julien Roche[1#], and Baoyu Chen[1#]

Affiliations:

[1]Roy J Carver Department of Biochemistry, Biophysics, and Molecular Biology, Iowa State University, Ames, IA 50014, USA.

[2]Department of Chemistry and Biochemistry, Institute of Molecular Biology, University of Oregon, Eugene, OR 97403, USA.

[3]Department of Biology, Stanford University, Stanford, CA, 94305, USA

[4]Neurosciences IDP, Stanford University, Stanford, CA, 94305, USA

[5]Howard Hughes Medical Institute, Stanford University, Stanford, CA, 94305, USA

[#]Correspondence to: stone@iastate.edu; jroche@iastate.edu

Abstract

Dendrite morphogenesis is essential for neural circuit formation, yet the molecular mechanisms underlying complex dendrite branching remain elusive. Previous studies on the highly branched *C. elegans* PVD sensory neuron identified a membrane co-receptor complex that links extracellular signals to intracellular actin remodeling machinery, promoting high-order dendrite branching. In this complex, the claudin-like transmembrane protein HPO-30 recruits the WAVE regulatory complex (WRC) to dendrite branching sites, stimulating the Arp2/3 complex to polymerize actin. We report here our biochemical and structural analysis of this interaction, revealing that the intracellular domain (ICD) of HPO-30 is intrinsically disordered and employs two distinct mechanisms to regulate the actin cytoskeleton. First, HPO-30 ICD binding to the WRC requires dimerization and involves the entire ICD sequence, rather than a short linear peptide motif. This interaction enhances WRC activation by the GTPase Rac1. Second, HPO-30 ICD directly binds to the sides and barbed end of actin filaments. Binding to the barbed end requires ICD dimerization and inhibits both actin polymerization and depolymerization, resembling the actin capping protein CapZ. These dual functions provide an intriguing model of how membrane proteins can integrate distinct mechanisms to fine-tune local actin dynamics.

Introduction

Neurons exhibit a variety of shapes, but they all share a fundamental architecture comprising a cell body, a primary axon, and many branching dendrites adorned with numerous tiny projections called spines (Burianek and Soderling, 2013; Jan and Jan, 2003; Lefebvre et al., 2015). Dendrite and spine formation is critical for nervous system development, as they establish the majority of post-synaptic connections in animals and define the intricate wiring of neural circuits (Hotulainen and Hoogenraad, 2010; Scott and Luo, 2001; Tavosanis, 2012). Actin and microtubule filaments are essential for initiating and promoting the outgrowth of newly formed neurites during dendrite development (Cheng and Poo, 2012; Zhao et al., 2017). Disruptions in actin cytoskeleton regulation can alter dendrite morphology and neural connections, contributing to various neurodevelopmental disorders such as autism, mental retardation, and schizophrenia (Yan et al., 2016).

A primary mechanism by which neurons regulate actin polymerization involves the Arp2/3 complex, a seven-protein assembly that binds to the sides of existing actin filaments and promotes the formation of branched actin filament networks (Goley and Welch, 2006; Hasegawa et al., 2022; Machesky et al., 1994; Pollard, 2007). The Arp2/3 complex is intrinsically inactive and requires activation by nucleation promoting factors (NPFs), which primarily consist of the Wiskott-Aldrich Syndrome Protein (WASP) family proteins (Alekhina et al., 2017; Kramer et al., 2022; Pollitt and Insall, 2009; Takenawa and Suetsugu, 2007). These proteins contain a conserved WCA (WH2-central-acidic) sequence at their C terminus, which can directly bind to and activate Arp2/3. The N-terminal sequences of these proteins vary greatly and define their regulatory mechanism and cellular function (Alekhina et al., 2017; Kramer et al., 2022; Machesky and Insall, 1998).

WAVE (Wiskott-Aldrich Verprolin homology) belongs to the WASP family and is part of a multi-protein assembly known as the WAVE regulatory complex (WRC). Consisting of five subunits—Sra1, Nap1, Abi2, HSPC300, and WAVE (or their corresponding orthologs in vertebrates) (Chen et al., 2010; Eden et al., 2002; Gautreau et al., 2004; Polesskaya et al., 2021; Rottner et al., 2021)—the WRC facilitates actin polymerization downstream of membrane signaling in neurons. This activity is crucial for various neuronal processes, including growth cone formation, axon branching, dendrite branching, synapse formation, and axon guidance and projection (Chia et al., 2014; Chou and Wang, 2016; Pilpel and Segal, 2005; Racz and Weinberg,

65 2008; Soderling et al., 2007; Stephan et al., 2011; Tahirovic et al., 2010; Yamazaki et al., 2005;
66 Yokoyama et al., 2011). Disruption of WRC function can profoundly affect the nervous system
67 in animals, resulting in altered spine morphology and density, intellectual disability, and
68 embryonic death (Dahl et al., 2003; Soderling et al., 2003). Mutations in WAVE and other WRC
69 subunits have been linked to various neurodevelopmental disorders in humans, including
70 neurodevelopmental disorder with absent language and variable seizures (NEDALVS),
71 developmental and epileptic encephalopathy-65 (DEE-65), and Alzheimer's disease (Begemann
72 et al., 2021; Conway et al., 2018; Ito et al., 2018; Kirkpatrick et al., 2017; Kramer et al., 2022;
73 Kumar et al., 2013; Olive et al., 2020; Rottner et al., 2021; Shimojima Yamamoto et al., 2021;
74 Sims et al., 2017; Srivastava et al., 2021; Zhao et al., 2021; Zweier et al., 2019).
75 The WRC inhibits WAVE activity by sequestering its C-terminal WCA to a conserved
76 surface formed by the Sra1 and WAVE subunits (Chen et al., 2017, 2010; Eden et al., 2002;
77 Kramer et al., 2022). Various molecules can recruit the WRC to the membrane and/or
78 simultaneously activate it through direct interactions, releasing the WCA to promote Arp2/3-
79 mediated actin polymerization. These ligands include small GTPases (e.g., Rac1 and Arf), acidic
80 phospholipids (e.g., PIP_3), adaptor proteins, and a wide array of membrane proteins containing
81 the WIRS motif (WRC interacting receptor sequence, defined as Φ-x-T/S-F-x-x, where Φ is a
82 bulky hydrophobic residue and x is any residue) (Chen et al., 2017, 2014a, 2010; Ding et al.,
83 2022b; Eden et al., 2002; Kobayashi et al., 1998; Koronakis et al., 2011; Lebensohn and
84 Kirschner, 2009; Rottner et al., 2021; Yang et al., 2022). Many WIRS-containing membrane
85 proteins, such as SYG-1, Robo, DCC, Neogenin, TMEM132, neuroligins, and various
86 protocadherins, are essential neuronal receptors that depend on the WIRS-WRC interaction to
87 regulate diverse neural development processes (Chaudhari et al., 2022, 2021; Chia et al., 2014;
88 Fan et al., 2018; Lee et al., 2016; Wang et al., 2021; Xing et al., 2018).
89 In previous studies, the claudin-like receptor HPO-30 was identified as a novel WRC-
90 binding protein, which does not contain a WIRS motif. The HPO-30-WRC interaction is
91 essential for high-order dendrite branching in the PVD sensory neuron in *C. elegans* (Zou et al.,
92 2016). HPO-30 acts as a co-receptor with the cell adhesion molecule DMA-1. The extracellular
93 domain of DMA-1 forms a multi-ligand complex with the secreted protein LECT-2 and the
94 extracellular domains of the epidermal cell receptors SAX-7 and MNR-1, providing spatial cues
95 for initiating dendrite branching in PVD neurons (Dong et al., 2013; Zou et al., 2018, 2016). The

intracellular domain (ICD) of HPO-30 directly binds to the WRC, while the ICD of DMA-1 binds the Rac guanine nucleotide exchange factor (GEF) TIAM-1, increasing the local concentration of activated Rac1, the canonical activator of WRC (Tang et al., 2019; Zou et al., 2018). Together, the HPO-30-DMA-1 co-receptor organizes a multi-protein complex that bridges extracellular cues to the intracellular actin remodeling machinery to regulate high-order dendrite branching (Zou et al., 2018).

The interaction mechanism between HPO-30 ICD and the WRC remains elusive, and it is uncertain if the ICD has additional functions beyond its WRC binding activity. Unlike other WRC-binding membrane proteins, HPO-30 ICD lacks a WIRS motif and uses a non-WIRS mechanism for WRC interaction. Prior research has shown that deletion of the C-terminal half of the HPO-30 ICD strongly affects WRC binding *in vitro* and high-order dendrite branching *in vivo*. However, it is unclear whether the HPO-30 ICD uses a linear peptide motif analogous to the WIRS motif for WRC binding (Zou et al., 2018). Although HPO-30 shares homology with mammalian tight junction claudin proteins, its ICD sequence is conserved only in nematode worms. Intriguingly, HPO-30 ICD binds to both *C. elegans* and human WRC, suggesting a conserved interaction mechanism across species (Zou et al., 2018). Thus, understanding the HPO-30-WRC interaction is critical for identifying other potential membrane proteins that regulate the WRC in humans through the same interaction surface.

In this study, we conducted biochemical and structural analyses of the HPO-30-WRC interaction. Our findings reveal that the HPO-30 ICD differs from other WRC-interacting receptors, as the entire ICD sequence—rather than a short peptide motif like the WIRS—is involved in the interaction. We also discovered that dimerization is necessary for HPO-30 ICD to bind to the WRC, which works cooperatively with Rac1 to promote WRC activation. Surprisingly, we found that the HPO-30 ICD directly interacts with actin filaments in a dimerization-dependent manner. The dimeric form of HPO-30 ICD binds to both the side and the barbed end of actin filaments, inhibiting both actin polymerization and depolymerization, resembling the activity of the actin capping protein CapZ. These dual activities of HPO-30 ICD present a fascinating example of how a membrane receptor can regulate local actin dynamics by simultaneously controlling the localization and activity of a central actin nucleation factor and directly binding to and modulating actin filaments to support an essential biological process.

127 **Results**

128 **HPO-30 ICD uses the entire sequence, rather than a short peptide motif, to bind the WRC**

129 The HPO-30 ICD lacks a WIRS motif, which led us to hypothesize that it might use a
130 different linear motif to bind the WRC. To identify this potential sequence motif, we divided
131 HPO-30 ICD sequence into continuous segments of five amino acids (a.a.) (Δ1-10 in **Figure 1A**)
132 and mutated all a.a. in each segment to alanines. We then used GST pull-down assays to assess
133 the impact of each segment on WRC binding (**Figure 1B**). Interestingly, we found that mutating
134 nearly any segment reduced the binding to WRC, with the middle region of the ICD showing the
135 most significant effect (Δ5, 6, 7 in **Figure 1A,B**, lanes 7-9). This finding supports the previous
136 qualitative data obtained under suboptimal pull-down conditions (Zou et al., 2018). It is worth
137 noting that while most mutants contained a N-terminal GST-tag, several mutations near the C-
138 terminus of the ICD used a C-terminal GST-tag to improve the yield of full-length protein (Δ8-
139 Δ10 in **Figure 1**, lanes 10-13 in **Figure 1B**).

140 It is interesting that none of the alanine-scan mutations completely abolished the binding
141 to WRC, unlike WIRS-mediated binding where single amino acid mutations in the WIRS motif
142 can readily eliminate the interaction (Chen et al., 2014a). In line with this finding, the wild type
143 (WT) ICD had a dissociation constant (K_D) of ~1.69 μM, as measured by an equilibrium pull-
144 down (EPD) assay (**Figure 1D,** black and **Figure 1 – figure supplement 1A**), while the alanine-
145 scan mutant Δ5, which had the strongest effect in the non-equilibrium GST pull-down assay
146 (**Figure 1A,B,** lane 7), only mildly increased the K_D to ~5.06 μM, still maintaining significant
147 residual binding (**Figure 1D**, light yellow and **Figure 1 – figure supplement 1B**) (Chen et al.,
148 2017; Kuzmic, 1996; Pollard, 2010). More extensive mutations in the ICD, either in the N-
149 terminal, middle, or C-terminal regions, more severely disrupted the binding (**Figure 1A,C** Δ11-
150 14). These data suggest the entire ICD sequence is involved in interacting with the WRC. This is
151 distinct from WIRS-containing membrane proteins where the WIRS motif is essential for
152 binding the WRC, and sequences outside the WIRS motif have only marginal contributions, if
153 any (Chen et al., 2014a).

154

155 **HPO-30 ICD contains residual structural elements, but is predominantly disordered in**
156 **solution**

157 Two potential models could explain how the entire ICD of HPO-30 binds to the WRC:
158 either the ICD might fold into a three-dimensional structure to bind, or the ICD might exist as an
159 extended linear peptide that makes an extensive contact with the WRC. To distinguish between
160 these two models and understand how the binding occurs, we investigated the structure of the
161 ICD using various approaches.

162 First, we submitted the sequence of ICD to multiple *in silico* structural prediction
163 software. These programs include secondary structure analyses (JPred, PredictProtein, PSIPred,
164 and SABLE) and *ab initio* tertiary structure predictions (LOMETS, QUACK, RaptorX, Rosetta,
165 AlphaFold 2.0, and RoseTTAFold) (**Figure 1—figure supplement 2)** (Adamczak et al., 2004;
166 Bernhofer et al., 2021; Bonneau et al., 2001; Drozdetskiy et al., 2015; Jumper et al., 2021;
167 Källberg et al., 2012; McGuffin et al., 2000; Minkyung et al., 2021; Wu and Zhang, 2007).
168 Nearly all programs predicted that the ICD contains a short alpha helix followed by two short
169 beta strands (**Figure 1A**). This is distinct from WIRS-containing proteins, where the WIRS motif
170 must reside in unstructured sequences for proper binding. It is noteworthy that the sequences
171 most critical for binding, such as Δ5, Δ6, and Δ7 in **Figure 1**, are within or close to these
172 secondary structural elements. In contrast to the consistent secondary structure prediction,
173 however, tertiary structure predictions yielded varied results, in which the secondary structural
174 elements are folded differently depending on the program and the context of ICD sequence
175 (isolated ICD vs. full-length HPO-30) used for the predictions (**Figure 1—figure supplement**
176 **2**). The variability observed in the predictions suggests that the ICD may not adopt a well-
177 defined three-dimensional structure, but rather may exist as a large and heterogeneous
178 conformational ensemble.

179 To further assess these structural predictions, we performed a series of all-atom
180 molecular dynamics (MD) simulations using the AMBER99SB-disp force field, which combines
181 a new generation of water model with parameters specifically designed to capture the behavior of
182 partially disordered proteins in solution (Robustelli et al., 2018). The top-ranking conformations
183 from all eight predictions were subjected to 200-ns simulations to assess the conformational
184 stability of the predicted structural models. The trajectories showed significant conformational
185 fluctuations, with large root mean square deviation (RMSD) up to 20 Å from their corresponding
186 initial models **(Figure 1 – figure supplement 3)**. The snapshots of the simulated molecules
187 revealed major random reorganization of the structural elements, suggesting that the predicted

188 tertiary structures were transient or unstable conformations, or may require specific conditions or
189 contexts to exist. Notably, in almost all simulated structures, the alpha-helical region remained
190 relatively stable, supporting its presence in the largely disordered ICD **(Figure 1 – figure**
191 **supplement 3)**. Taken together, these *in silico* analyses suggest that while the ICD may contain
192 structural elements, it is likely disordered and does not possess a stable conformation in solution.
193
194

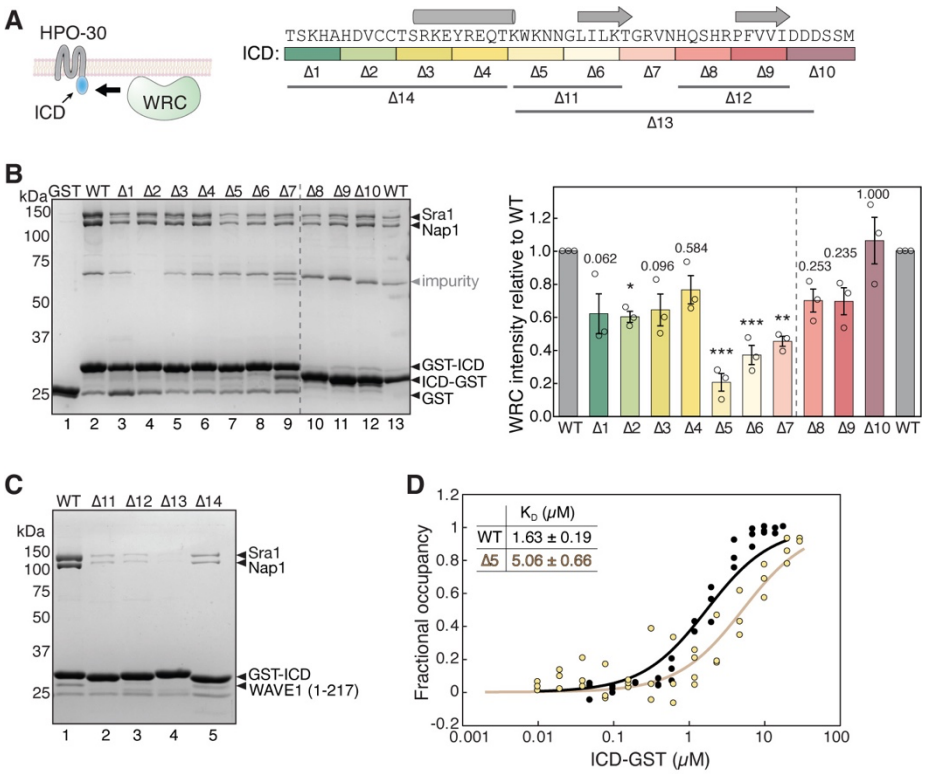

Figure 1. HPO-30 ICD binds to the WRC using its entire sequence. (A) Left: cartoon representation of HPO-30 as a four-pass transmembrane protein, with the ICD binding to the WRC. Right: annotation of HPO-30 ICD sequence and mutants used in this study. In each mutant, the corresponding amino acids were replaced with alanines (for Δ1-10) or (GGS)n (for Δ11-14). The regions are color coded according to the alanine mutations, and the consensus secondary structural elements from multiple secondary structure predictions are indicated above. **(B)** Representative Coomassie blue-stained SDS PAGE gel (left) and quantification (right) of three independent experiments showing GST-ICD (lane 2-9, 200 pmol) and ICD-GST (lane 10-13, 200 pmol) pulling down $WRC^{230\Delta WCA}$ (150 pmol). Sra1/Nap1 band intensity was used to quantify the pull-down signals of WRC. Signals from GST-ICD or ICD-GST pull-downs were normalized to the corresponding WT ICD (lane 2 and 13, respectively). Error bars represent standard error, * $p < 0.05$, ** $p < 0.005$, *** $p < 0.001$ from ANOVA with Tukey test. **(C)** Coomassie blue-stained SDS PAGE gel showing GST-ICD Δ11-14 mutants (200 pmol) pulling down $WRC^{217\Delta WCA}$ (300 pmol). **(D)** Fitted curves of the dissociation constant (K_D) of the interaction between ICD-GST and WRC. Data were pooled from three independent repeats and globally fitted to a one-site binding model using DynaFit.

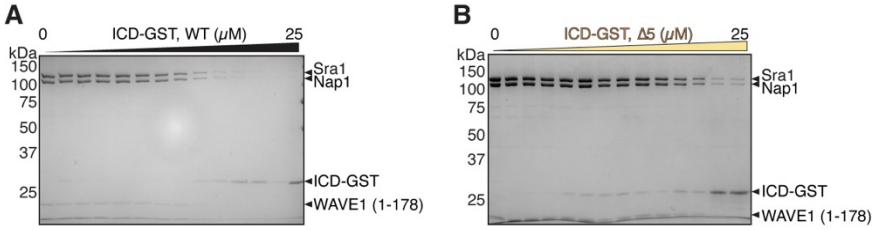

Figure 1 – figure supplement 1. Equilibrium pull-down assay of ICD-GST and WRC. (A-B) Representative Coomassie blue-stained SDS-PAGE EPD gels used to quantify the dissociation constants shown in Figure 1D for ICD WT (A) and Δ5 (B).

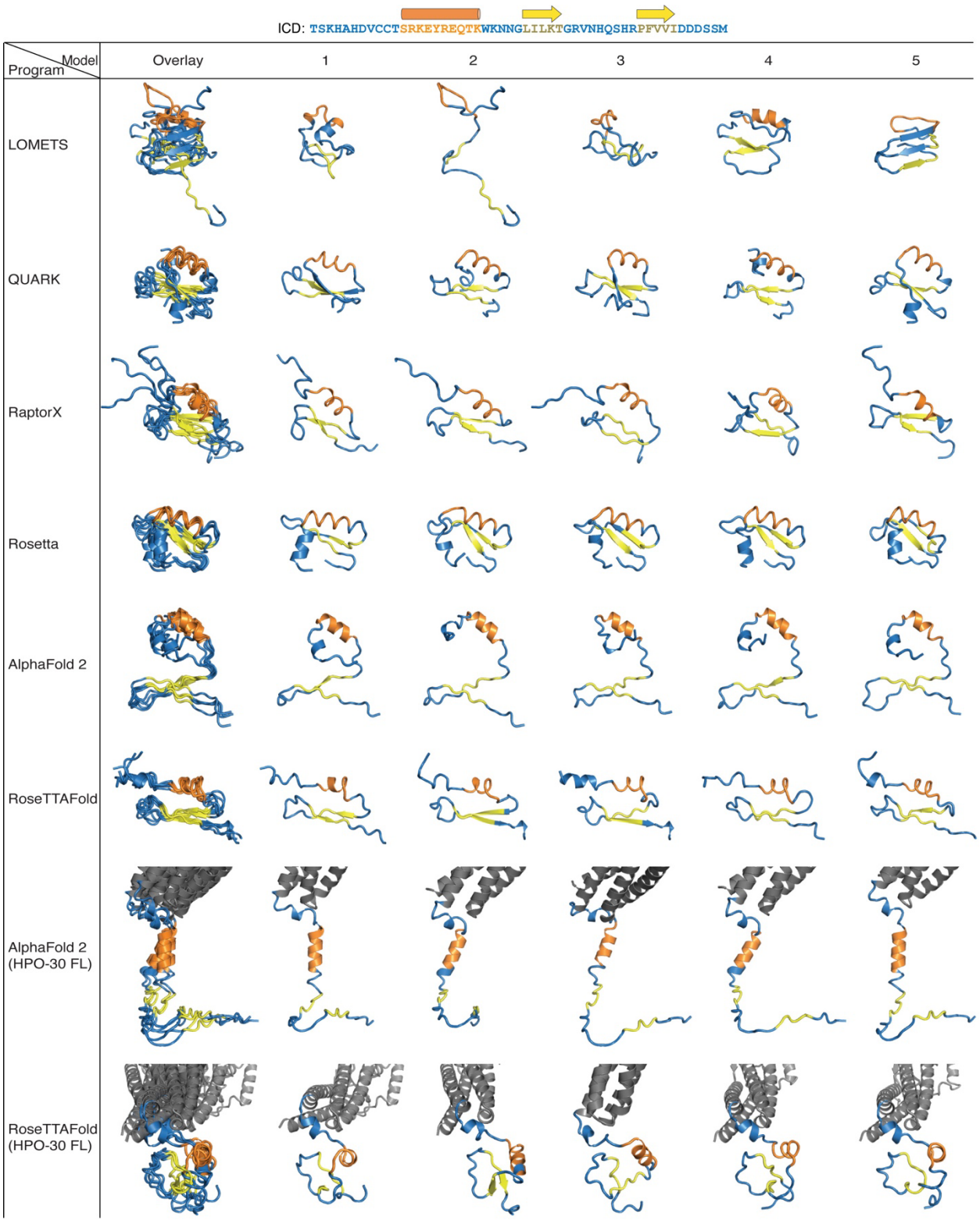

Figure 1—figure supplement 2. *Ab initio* structure prediction of HPO-30 ICD. Top five ranked structures of HPO-30 ICD predicted by the indicated programs are shown.

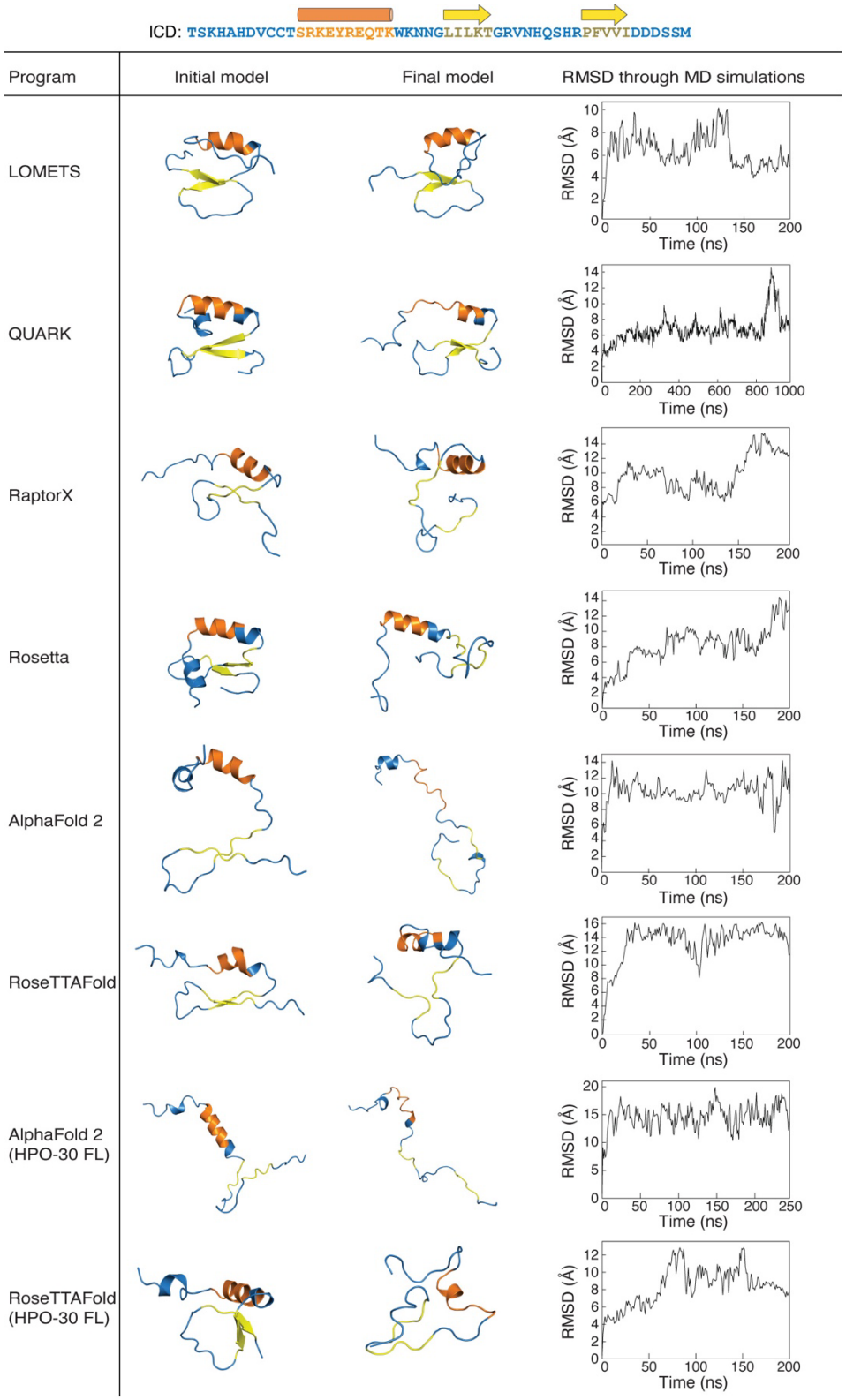

Figure 1—figure supplement 3. MD simulations of predicted ICD structures. All-atom molecular dynamics simulations were conducted for the top ranked structural models generated by indicated programs. Left, the

initial structure prediction fed into the MD simulations. Middle, the final structure after the MD simulations ended. Right, RMSD of the backbone of the HPO-30 ICD over the course of the MD simulation, relative to the starting structure.

227 To experimentally validate the above computational analyses, we used circular dichroism
228 (CD) spectroscopy to evaluate HPO-30 ICD secondary structure composition in solution. In
229 agreement with the MD simulations, the CD spectrum of ICD did not display major peaks at the
230 wavelengths characteristic of either alpha helices (positive at 193 nm and negative at 218 and
231 222 nm) or beta sheets (positive at 195 nm and negative at 217 nm), clearly distinct from the CD
232 spectrum of bovine serum albumin (BSA) obtained under the same conditions (**Figure 2A**).
233 Adding an osmolyte, trimethylamine N-oxide (TMAO), which is commonly used to promote
234 protein folding, did not significantly alter the CD spectrum or enhance the ICD-WRC interaction
235 (**Figure 2—figure supplement 1A,B**) (Baskakov et al., 1999). Yet careful examination of the
236 CD spectrum revealed that the ICD is different from unstructured proteins, which typically
237 exhibit a positive peak at 222 nm (Hwang and Waite, 2012). This suggests that the HPO-30 ICD
238 might contain some structural elements, possibly a helical region, as reflected by the negative
239 peak at 222 nm.

240 Being unable to grow crystals of the ICD (either by itself, attached to solubility tags, or
241 together with the WRC), we used solution nuclear magnetic resonance (NMR) spectroscopy to
242 further investigate the structural features of the ICD. The ^{1}H-^{15}N heteronuclear single quantum
243 coherence (HSQC) spectra of untagged ^{15}N-labeled ICD were well resolved, from which we
244 identified 50 distinct amide crosspeaks, out of the 51 expected (**Figure 2B**). The narrow ^{1}H
245 chemical shift dispersion was consistent with our CD spectroscopy analysis and suggested that
246 the ICD is predominantly disordered in solution. Fusing the ICD to two different solubility tags,
247 including the monomeric 56-a.a. tag GB1 (B1 domain of Streptococcal protein G, commonly
248 used in NMR) (Zhou and Wagner, 2010) and the dimeric GST-tag, did not cause any significant
249 chemical shift changes to the ICD crosspeaks **(Figure 2C**, **Figure 2 – figure supplement 1D,E)**,
250 suggesting that solubility tags and dimerization do not promote ICD folding. Moreover, the
251 NMR spectra were nearly identical at different protein concentrations (50 – 700 μM) and
252 temperatures (283 K – 298 K), suggesting that the ICD alone does not undergo concentration-
253 dependent structural changes (data not shown).

254 While the 2D ^{1}H-^{15}N NMR spectroscopy can provide an overall assessment of the degree
255 of structural disorder based on the magnitude of the ^{1}H chemical shift dispersion, a precise
256 characterization of secondary structure content requires measuring the chemical shifts values of
257 individual backbone nuclei. ^{13}C chemical shift values measured for carbons alpha are particularly

258 strong indicators of secondary structure motifs. We therefore collected a set of conventional 3D
259 triple resonance experiments [HNCA, HNCO, and HN(CO)CA] and were able to assign the
260 backbone chemical shifts (^{1}H, ^{15}N, and ^{13}C) of 41 out of 51 amino acids of the ICD (**Figure 2 –**
261 **figure supplement 1F**). The overall measured ^{13}Cα chemical shifts show little deviation (<1
262 ppm) from idealized random coil chemical shifts (**Figure 2D**) (Kjaergaard et al., 2011;
263 Kjaergaard and Poulsen, 2011), indicating that the ICD is predominantly disordered in solution,
264 consistent with the MD simulations, the CD data, and the initial assessment based on the 2D
265 NMR spectra. However, we observed small but consistent positive secondary Cα chemical shifts,
266 suggesting the presence of a transient (~25-30%) alpha-helical motif in the same region that was
267 predicted to form an alpha helix in many of the *ab initio* predictions **(Figure 2D)**. Although we
268 could not obtain adequate signals for Cß atoms, the chemical shift of CO was consistent with the
269 Cα chemical shift data, further confirming that the same region of the ICD contained ~25-30%
270 helical motif **(Figure 2 – figure supplement 1G)**.
271 Together, our data suggest that the HPO-30 ICD is predominantly disordered in solution,
272 although it does contain some local secondary structures that could potentially fold into different
273 conformations. The exact nature of these conformations is unclear, and it remains challenging to
274 determine whether the entire ICD binds to the WRC as an extended linear peptide or as a
275 compact folded structure.
276
277

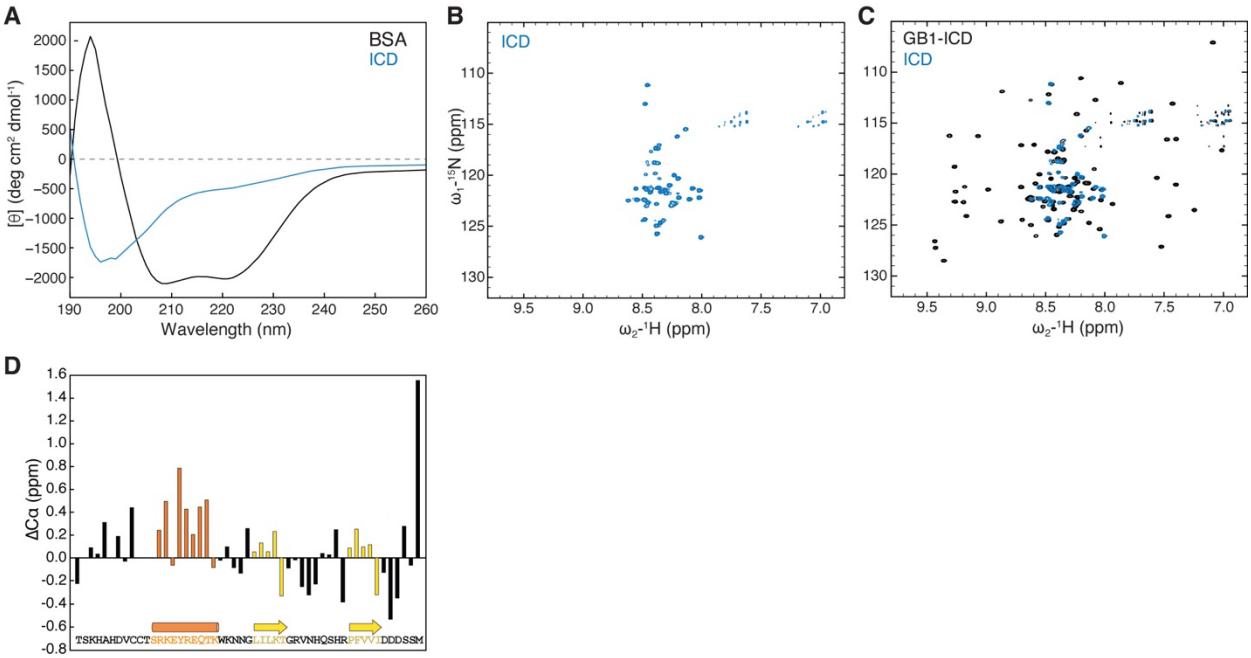

Figure 2. HPO-30 ICD is largely disordered but may contain secondary structural elements. (**A)** CD spectrum of 2 mg/mL untagged HPO-30 ICD or BSA in identical buffer conditions (see Methods and Materials). **(B-C)** 2D TROSY spectra of untagged HPO-30 ICD (B) and GB1-ICD (C) in the same buffer condition (100 mM NaCl, 10 mM HEPES pH 7.0, and 5% glycerol). **(D)** Secondary Cα chemical shift showing the deviation from idealized random coils of Cα chemical shifts measured for HPO-30 ICD.

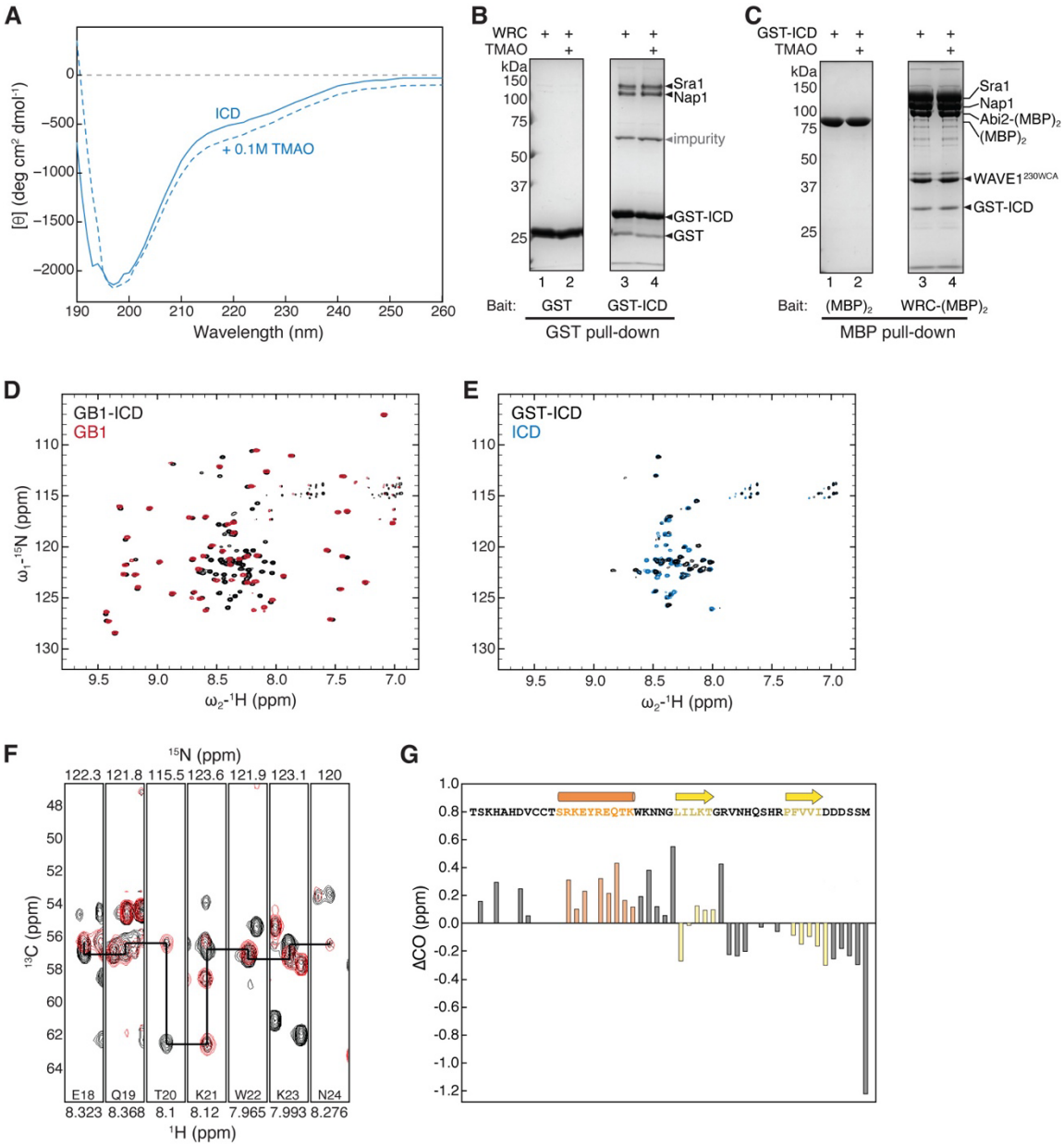

Figure 2—figure supplement 1. HPO-30 ICD is largely disordered. (A) CD spectrum of 2 mg/mL HPO-30 ICD in the absence or presence of 0.1 M TMAO. **(B-C)** Coomassie blue-stained SDS PAGE gels showing GST-ICD (200 pmol) pulling down WRC$^{230\Delta WCA}$ (150 pmol) (B) or WRC:Abi2-(MBP)$_2$ (60 pmol) pulling down GST-ICD (600 pmol) (C), with and without TMAO. **(D-E)** 2D TROSY spectra of the GB1 tag compared to the HPO-30 ICD (D) and GST-ICD (E) in the same buffer condition (100 mM NaCl, 10 mM HEPES pH 7.0, and 5% glycerol). **(F)** Representative strip plots generated in SPARKYNMR showing an overlay of the 3D HNCA and HN(CO)CA spectra (in black and red respectively). The straight lines indicate the sequential connection between the ^{13}Cα crosspeaks of residues (i) and (i-1). **(G)** Secondary CO chemical shift showing the deviation from idealized random coils of CO chemical shifts measured for HPO-30 ICD.

295 **HPO-30 ICD requires dimerization to bind WRC**

296 During our investigation of the interaction between the HPO-30 ICD and the WRC, we
297 noticed that GST-tagged ICD exhibited robust binding to WRC, whereas MBP (maltose binding
298 protein)-tagged ICD showed much weaker binding (**Figure 3A**). Note that both constructs
299 contained extensive flexible linkers of at least 16 a.a. between the tag and the ICD to prevent
300 steric hindrance from the tag. Given that GST is a constitutive dimer while MBP is a monomer,
301 we hypothesized that efficient binding of the HPO-30 ICD to WRC may require dimerization.

302 We explored a variety of strategies to test this hypothesis. We first developed a new
303 WRC construct in which a dual MBP-tag, $(MBP)_2$, was tethered to the WRC. This $(MBP)_2$-WRC
304 would allow us to immobilize the WRC on amylose beads to pull down different monomeric vs.
305 dimeric forms of HPO-30 ICD. Out of three different designs of $(MBP)_2$-WRC, only the one
306 with an $(MBP)_2$ tag tethered to the C-terminus of Abi2 through sortase-mediated protein ligation
307 (Chen et al., 2011) effectively pulled down GST-HPO-30 ICD [herein referred to as WRC:Abi2-
308 $(MBP)_2$, **Figure 3—figure supplement 1B**], while the other two versions substantially interfered
309 with the interaction. One construct, WRC:$(MBP)_2$-HSPC300, has an $(MBP)_2$ tag fused to the N-
310 terminus of HSPC300 [which was previously used to immobilize the WRC and pull down
311 WIRS-containing proteins (Chen et al., 2014a)] (**Figure 3—figure supplement 1B**, lane 6 vs. 8),
312 and the other, WRC:$(MBP)_2$-Abi2, has $(MBP)_2$ fused to the N-terminus of Abi2 (**Figure 3—
313 figure supplement 1A**). Thus, it is possible the regions near the N-terminus of HSPC300 or
314 Abi2 are close to the HPO-30 ICD binding surface (but not the WIRS binding surface).

315 Using WRC:Abi2-$(MBP)_2$, we compared the binding of ICDs that carry various
316 monomeric vs. dimeric tags. We observed that the dimeric form of GB1-ICD [referred to as
317 GB1-CC-ICD, in which we inserted a homo-dimeric coiled-coil sequence between GB1 and the
318 ICD (O'Shea et al., 1999)] exhibited much stronger binding than the monomeric GB1-ICD
319 **(Figure 3B)**. To rule out the possibility that the tag sequences, rather than dimerization,
320 influenced protein binding, we introduced chemically inducible dimerization (CID) tags, FKBP
321 and FRB, to the ICD (with the GB1 tag at the N-terminus) (Banaszynski et al., 2005) (**Figure
322 3C**). In the presence of the dimerizing agent rapamycin, GB1-FKBP-ICD and GB1-FRB-ICD
323 could form a tight heterodimer, as confirmed by size exclusion chromatography in the presence
324 and absence of rapamycin (**Figure 3—figure supplement 1C-E**). Consistent with results from
325 the constitutive dimeric tags, the addition of rapamycin to dimerize GB1-FKBP/FRB-ICD (F/F-

326 ICD for short hereafter) clearly promoted the binding of HPO-30 ICD (**Figure 3C**, lanes 2 vs. 3).
327 In fact, we observed robust binding of all dimeric constructs we tested, including GST-ICD,
328 ICD-GST, and DLC8-ICD (DLC8 is a constitutive dimer from the dynein light chain) (Wang et
329 al., 2003). In contrast, all monomeric constructs, including GB1-ICD, sumo-ICD, and mEGFP-
330 ICD exhibited very weak, if any, binding (**Figure 3 – figure supplement 2A, B**).
331 ICD binding relies on the dimerization tags to bring two copies of ICD in close
332 proximity, because a heterodimer containing only one copy of ICD (formed by mixing GB1-
333 FKBP-ICD with GB1-FRB tag) was unable to support binding (**Figure 3D**, lane 5-6). Similarly,
334 a heterodimer containing one WT ICD and one mutant ICD (alanine Δ5 mutation in Figure 1)
335 had weakened binding (**Figure 3—figure supplement 2F**). It is important to note that when
336 using the heterodimeric ICDs, we maintained the same total monomeric concentration of the WT
337 ICD between heterodimers and homodimers. Thus, the lack of binding from heterodimers was
338 due to the absence of the WT ICD dimer rather than a reduction in WT ICD concentration.
339 Various competition assays further support the observation that only dimeric form of the
340 ICD can effectively bind to WRC. For example, even when added in 5000-fold excess, the
341 chemically synthesized HPO-30 ICD peptide could not compete off GST-ICD binding (**Figure**
342 **3—figure supplement 2C**). In contrast, both F/F-ICD and DLC8-ICD binding to the WRC
343 could be effectively competed off by GST-ICD in a dose-dependent manner (**Figure 3—figure**
344 **supplement 2D**). Moreover, F/F-ICD was able to compete off GST-ICD binding to WRC only
345 in the presence of rapamycin, but not in its absence (**Figure 3—figure supplement 2E**, lanes 4
346 and 5). Taken together, our data strongly suggest that dimerization of the HPO-30 ICD is critical
347 for its binding to the WRC.
348

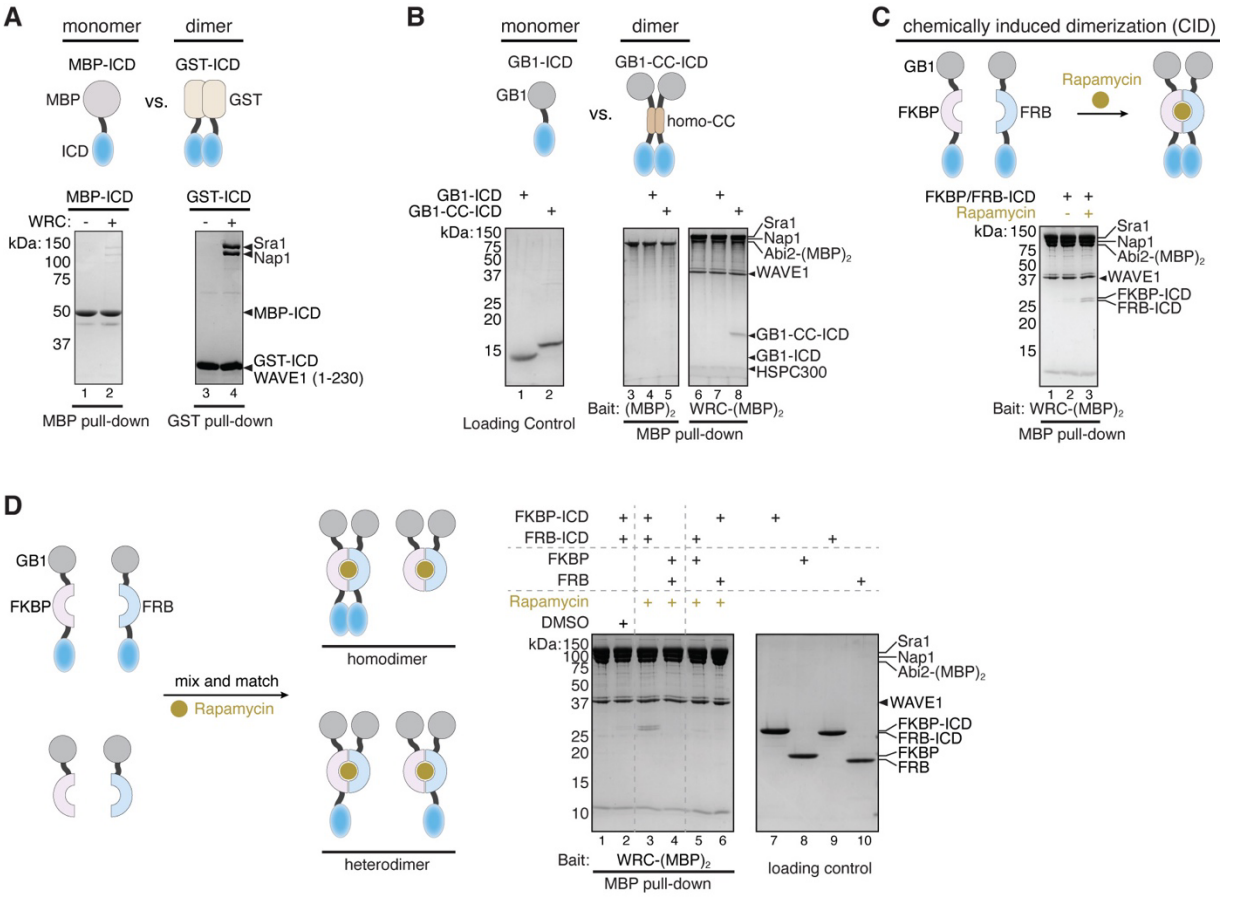

Figure 3. Dimerization tags enhance HPO-30 ICD binding to the WRC. (A-C) Top, schematic of monomeric and dimeric HPO-30 ICD constructs used in pull-downs. Bottom, Coomassie blue-stained SDS-PAGE gels showing (A) MBP-ICD or GST-ICD (200 pmol) pulling down $WRC^{230\Delta WCA}$ (200 pmol), (B) WRC:Abi2-$(MBP)_2$ (60 pmol) pulling down GB1-ICD or GB1-CC-ICD (600 pmol), and (C) WRC:Abi2-$(MBP)_2$ (60 pmol) pulling down FKBP/FRB-ICD in the absence or presence of rapamycin. Where it is noted, 5 µM rapamycin (or equal volume of DMSO as a negative control) was used to induce dimerization. For clarity, GB1-FKBP-ICD and GB1-FRB-ICD were referred to as FKBP-ICD and FRB-ICD, respectively. **(D)** Schematic of the assembly of homo- and heterodimers of HPO-30 ICD (left) and Coomassie blue-stained SDS PAGE gels (right) showing WRC:Abi2-$(MBP)_2$ (60 pmol) pulling down indicated homo- and heterodimers. In homo- and heterodimers, 1200 pmol of WT ICD monomeric unit was included to ensure the total number of WT ICD molecules remained the same.

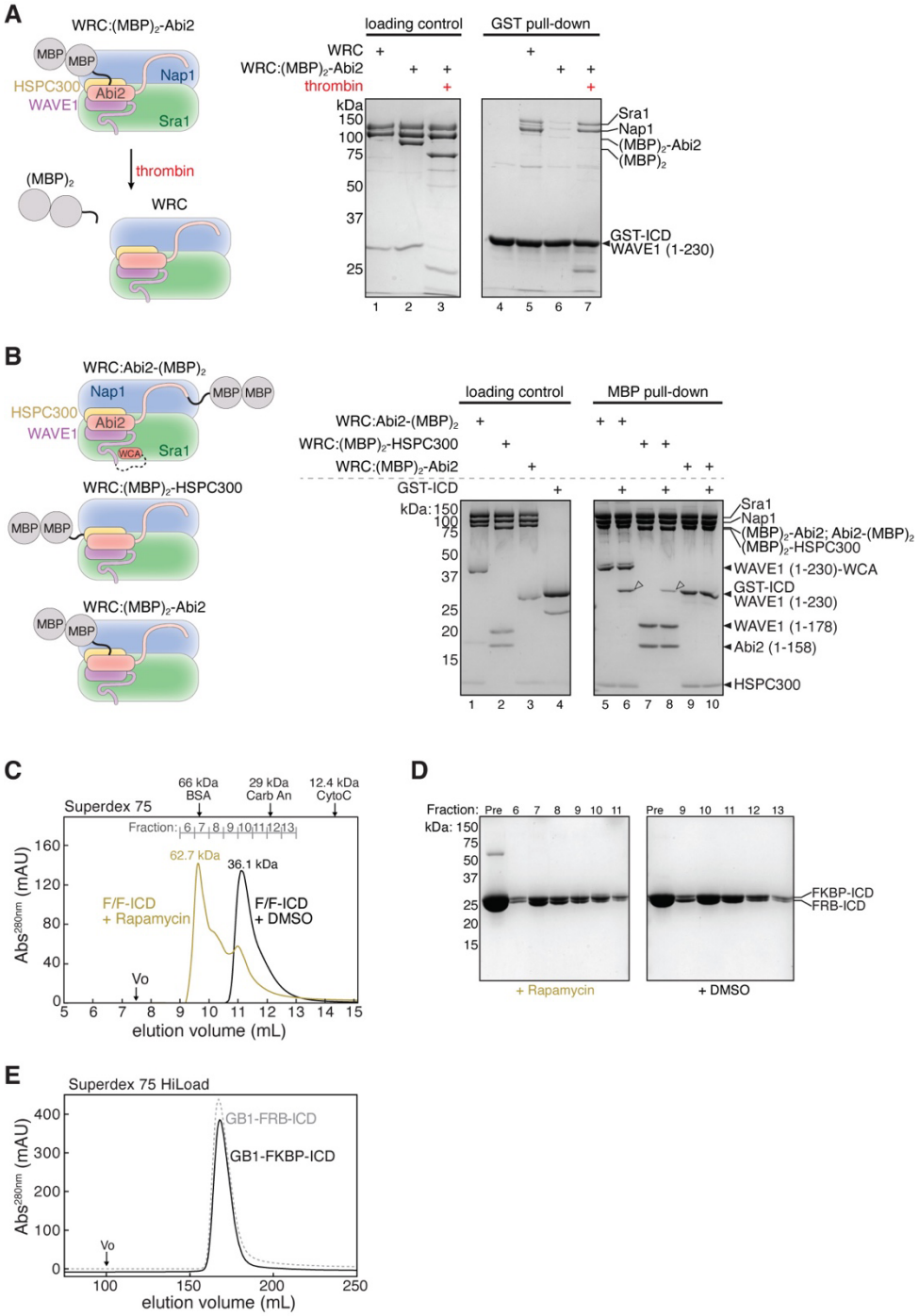

Figure 3—figure supplement 1. Protein quality control for dimerization experiments. (A) Schematic of removing $(MBP)_2$ tag from WRC:$(MBP)_2$-Abi2 by thrombin cleavage (left) and Coomassie blue-stained SDS PAGE gels (right) comparing GST-ICD (200 pmol) pulling down WRC:$(MBP)_2$-Abi2 (150 pmol) before or after removal of the $(MBP)_2$ tag. **(B)** Schematic of $(MBP)_2$-tagged WRC constructs (left) and Coomassie blue-stained SDS PAGE gels showing indicated $(MBP)_2$-tagged WRC (60 pmol) pulling down GST-ICD (600 pmol). Open arrowheads indicated pull-down signals. **(C)** Gel filtration chromatograms of equimolar GB1-FKBP-ICD and GB1-FRB-ICD in the presence or absence of 5 µM rapamycin (or equal volume of DMSO). Molecular weights determined from a

369 standard curve (see Materials and Methods) are indicated above the chromatogram. **(D)** Coomassie blue-stained
370 SDS-PAGE gels of the indicated gel filtration fractions from (C). **(E)** Gel filtration chromatograms of individual
371 GB1-FKBP-ICD and GB1-FRB-ICD proteins.
372
373

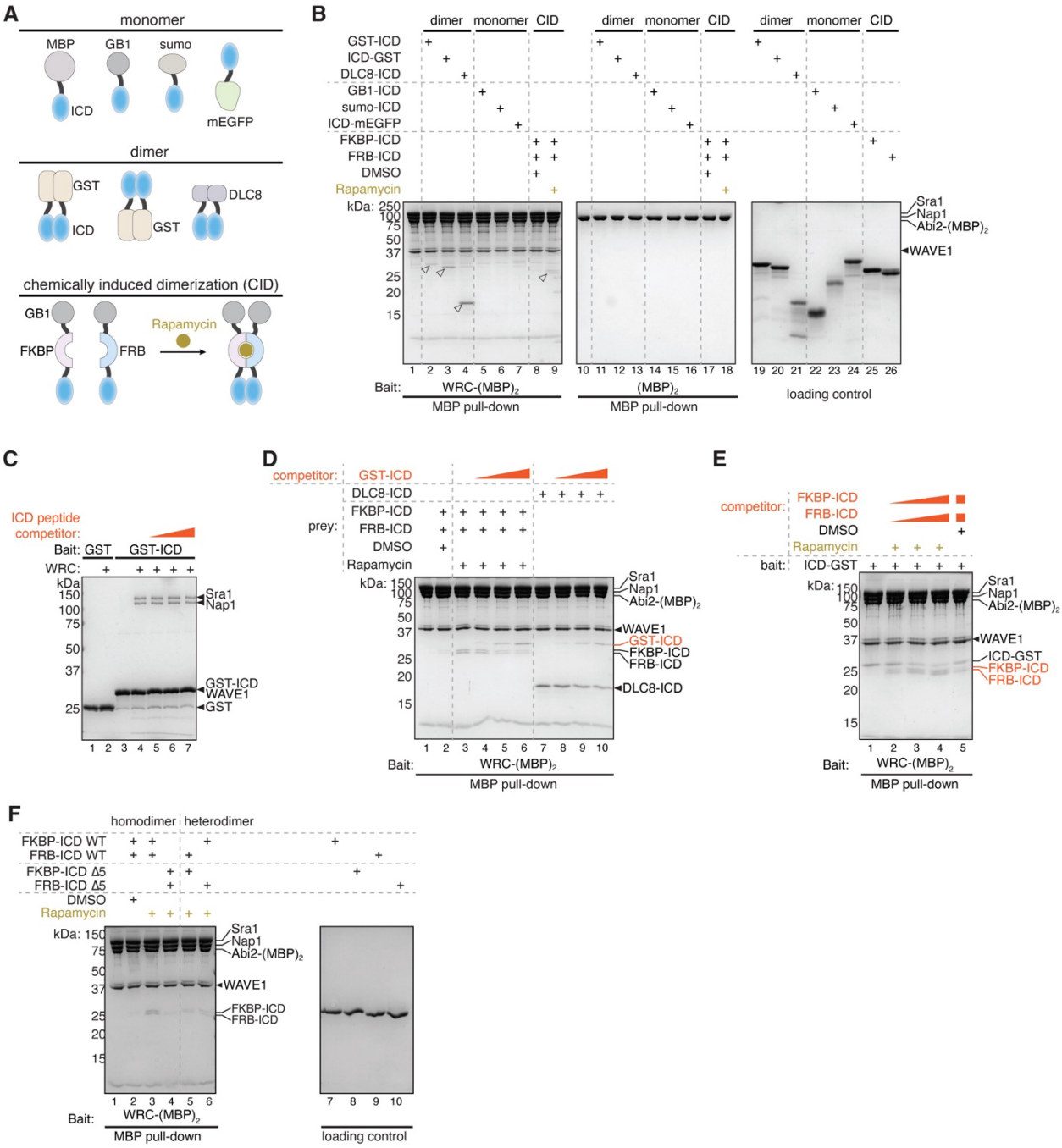

Figure 3—figure supplement 2. HPO-30 ICD binding to WRC requires dimerization tags. (A) Schematic of monomeric and dimeric HPO-30 ICD constructs used in pull-downs. **(B)** Coomassie blue-stained SDS PAGE gels showing WRC:Abi2-$(MBP)_2$ or $(MBP)_2$ (60 pmol) pulling down various monomeric and dimeric HPO-30 ICD (600 pmol) constructs indicated in (A). Where it is noted, 5 µM rapamycin (vs. equal volume of DMSO as a negative control) was used to induce dimerization. Open arrowheads indicate pull-down signals. For clarity, GB1-FKBP-ICD and GB1-FRB-ICD were referred to as FKBP-ICD and FRB-ICD, respectively. **(C)** Coomassie blue-stained SDS PAGE gel showing GST-ICD (200 pmol) pulling down $WRC^{230\Delta WCA}$ (150 pmol) in the presence of a chemically synthesized HPO-30 ICD peptide as a competitor (18-100 nmol). **(D)** Coomassie blue-stained SDS PAGE gels

383 showing WRC-$(MBP)_2$ (60 pmol) pulling down different dimeric HPO-30 ICD (600 pmol) in the presence of GST-
384 ICD as a competitor (600 to 6000 pmol). **(E)** Coomassie blue-stained SDS PAGE gel showing WRC-$(MBP)_2$ (60
385 pmol) pulling down ICD-GST (600 pmol) in the presence of FKBP/FRB-ICD as a competitor (600 – 6000 pmol).
386 **(F)** Coomassie blue-stained SDS PAGE gels showing WRC:Abi2-$(MBP)_2$ (60 pmol) pulling down different
387 combinations of homo- and heterodimers of WT and Δ5 HPO-30 ICD. In homo- and heterodimers, 1200 pmol of
388 WT ICD monomeric unit was included to ensure the total number of WT ICD molecules remained the same.

HPO-30 ICD can self-associate

How do dimeric tags promote ICD binding to WRC? We hypothesized that dimeric tags facilitate ICD dimerization, and only dimerized ICD can bind to WRC. To test this hypothesis, we first examined whether the ICD could interact with another copy of ICD, which would indicate the potential for ICD dimerization. Indeed, we found GST-ICD effectively pulled down MBP-ICD, indicating self-interaction **(Figure 4A)**. This is consistent with our co-immunoprecipitation assay, which showed that HA-tagged full-length HPO-30 retained Myc-tagged full-length HPO-30 when co-expressed in *Drosophila* S2 cells (**Figure 4—figure supplement 1B)**. The ICD-ICD interaction was readily disrupted by increased salt concentration (not shown) or higher pH **(Figure 4—figure supplement 1A)**, suggesting that the interaction likely involves electrostatic interactions. We further asked which region in the HPO-30 ICD was important for the ICD-ICD interaction. Using the same alanine scan mutants as in Figure 1A, we found that mutations in various regions impaired the ICD-ICD interaction, especially the N-terminal (Δ1 and Δ2) and the central regions (Δ5, Δ6, and Δ7) of the ICD **(Figure 4B)**. It is remarkable that Δ5, Δ6, and Δ7 sequences are also crucial for binding to WRC **(Figure 1B)**, suggesting that ICD dimerization is closely linked to the WRC interaction.

Due to technical challenges, we were unable to measure the binding affinity of the ICD-ICD interaction using intrinsic tryptophan fluorescence **(Figure 4—figure supplement 2A)**. Our structural predictions using AlphaFold Multimer (AFM) generated several different models, depending on the context of the ICD sequence used (**Figure 4—figure supplement 3A,B**) (Evans et al., 2022; Jumper et al., 2021). The isolated ICD was consistently predicted to form a homodimer (**Figure 3—figure supplement 3A**). In contrast, the full-length HPO-30 was predicted to form two distinct dimers, one mediated by the transmembrane helix 2 (H2) and the beta strand 4 (b4) in the extracellular domain, and the other mediated by the transmembrane helix 3 (H3) and the first helix of the ICD (**Figure 4—figure supplement 3B**). In both conformations, the ICD was predicted to form a long helix, without the two beta strands predicted for the monomeric ICD (**Figure 1A**; **Figure 1—figure supplement 2**; **Figure 4—figure supplement 3A**). All-atom MD simulations conducted on the dimeric structural models indicate that the dimer conformations are not stable over the course of 200 ns, suggesting that the limited helical interface between the two ICDs is not sufficient to form a stable complex **(Figure 4—figure supplement 3C)**.

420 In summary, our data suggest that HPO-30 ICD requires dimerization to interact with the
421 WRC. However, before to binding the WRC, the dimerized ICD may not have a stable
422 quaternary structure.
423
424

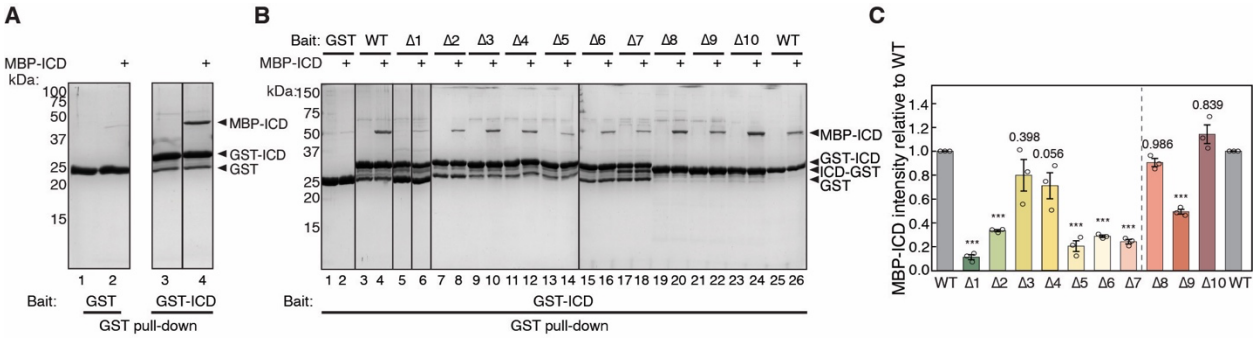

Figure 4. HPO-30 ICD can self-associate. (A) Coomassie blue-stained SDS-PAGE gels showing GST-ICD (300 pmol) pulling down MBP-ICD (6000 pmol). **(B)** Representative Coomassie blue-stained SDS-PAGE gels of three independent experiments showing GST-ICD alanine mutations (shown in Figure 1A) (300 pmol) pulling down MBP-ICD (6000 pmol). **(C)** Quantification of (B). The MBP-ICD band intensity was used to quantify the pull-down signal. Signals from GST-ICD or ICD-GST pull-downs were normalized to corresponding WT ICD (lane 4 and 26, respectively). Error bars represent standard error, * $p < 0.05$, ** $p < 0.005$, *** $p < 0.001$ from ANOVA on ranks.

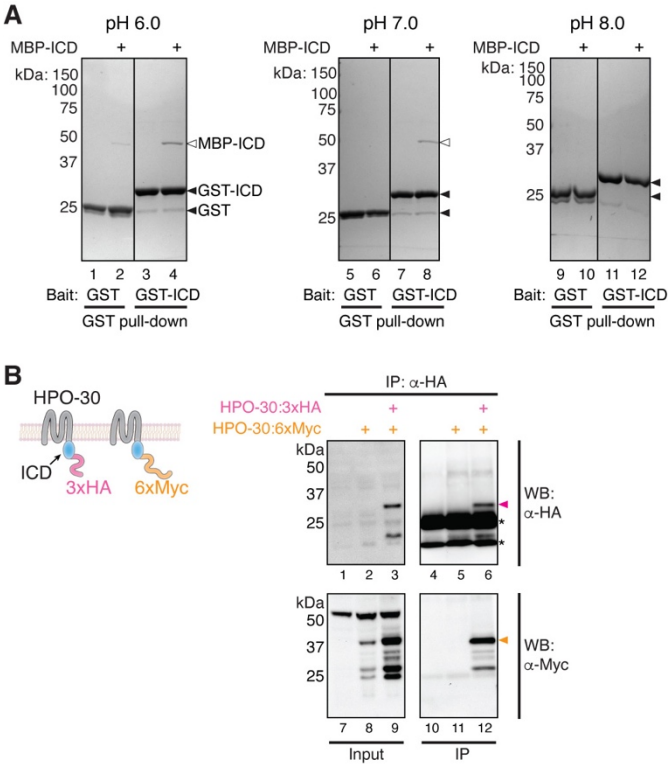

Figure 4 – figure supplement 1. HPO-30 ICD can interact with itself. (A) Coomassie blue-stained SDS-PAGE gels showing GST-ICD (300 pmol) pulling down MBP-ICD (6000 pmol) at pH 6.0 (left), pH 7.0 (middle), and pH 8.0 (right). **(B)** Schematic of full-length HPO-30 constructs co-expressed in *Drosophila* S2 cells (left) and Western blot images (right) showing co-immunoprecipitation of 3xHA-tagged HPO-30 (pink arrowhead) with 6xMyc-tagged HPO-30 (orange arrowhead). Asterisks indicate light and heavy chain of antibody.

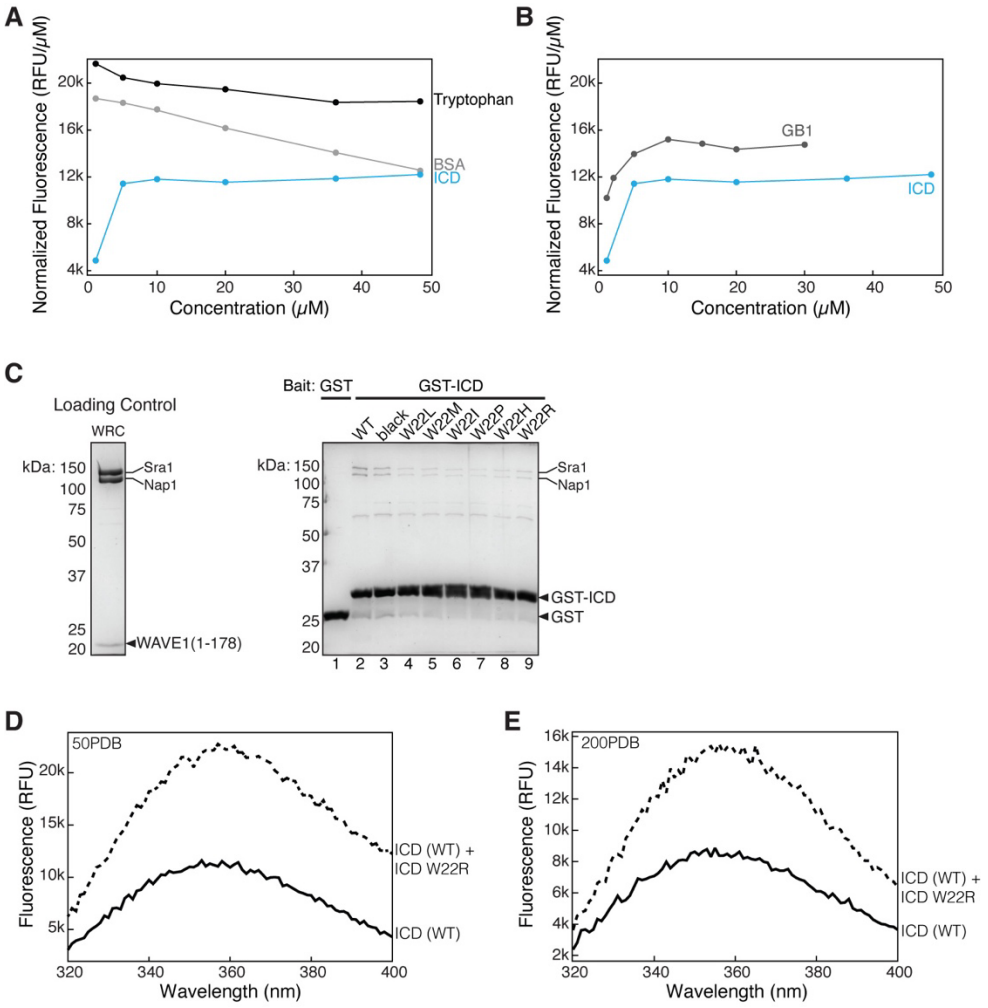

Figure 4 – figure supplement 2. Tryptophan fluorescence cannot be used to monitor the self-association of HPO-30 ICD. (A) Normalized intrinsic tryptophan fluorescence of free tryptophan (black), BSA (gray), and ICD (blue) at different concentrations. **(B)** Normalized intrinsic tryptophan fluorescence of GB1 tag (gray) and ICD (blue) at different concentrations. Note that the ICD curve is identical for both (A) and (B). ICD Trp fluorescence increases in the same manner as GB1, suggesting that the increase is not due to dimerization. **(C)** Coomassie blue-stained SDS-PAGE gels showing GST-ICD WT and various tryptophan mutants (W22X) (200 pmol) pulling down WRC[178] (200 pmol). **(D-E)** Raw intrinsic tryptophan fluorescence curves of ICD WT (solid line) and ICD WT + 250 μM ICD "black" (dashed lines) at 50 mM NaCl (D) and 200 mM NaCl (E). The increase in Trp fluorescence seen after addition of HPO-30 "black" ICD is not abolished in high salt conditions, suggesting it is non-specific to ICD-ICD dimerization.

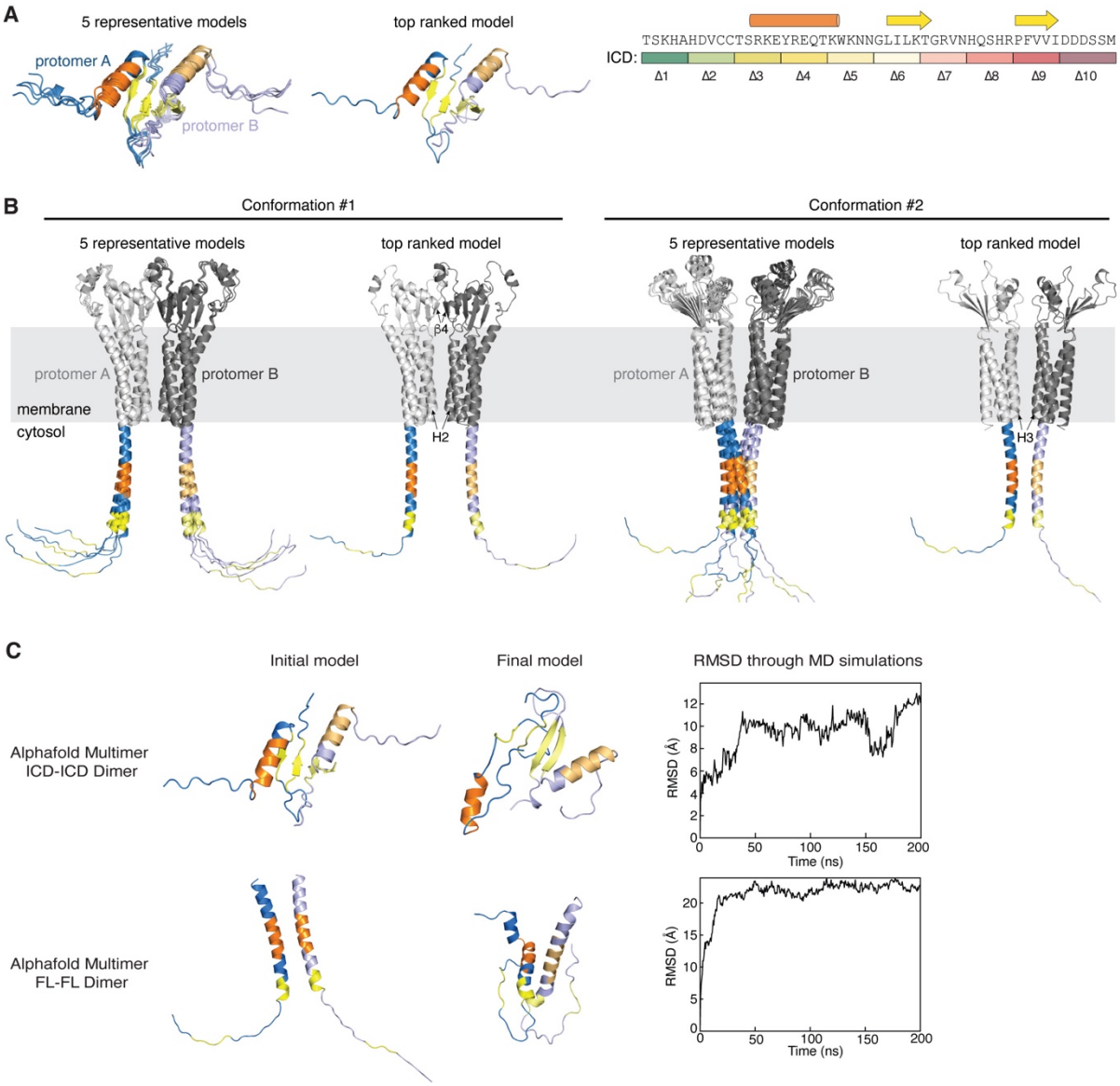

Figure 4—figure supplement 3. Structural predictions of HPO-30 ICD self-association. (A) AlphaFold Multimer predictions of the isolated HPO-30 ICD dimer. Protomer A secondary structure is colored using the same scheme shown on the top right, while protomer B is shown in lighter colors. **(B)** Two distinct dimer conformations of the full-length HPO-30 predicted by AlphaFold Multimer. **(C)** Molecular dynamics simulations of the predicted ICD dimers using an amber-99sb-ILDN forcefield. Left, the initial structure prediction fed into the MD simulations. Middle, the final structure after the MD simulations ended. Right, RMSD of the backbone of the HPO-30 ICD over the course of the MD simulation, relative to the starting structure.

463 **HPO-30 ICD inhibits actin polymerization, but promotes Rac1-mediated WRC activation**

464 Rac1 GTPase is the canonical activator of the WRC, and various WIRS-containing
465 receptors can further fine-tune WRC activation by Rac1 (Chen et al., 2014a), either positively or
466 negatively. We wondered how HPO-30 ICD binding could influence WRC activity in promoting
467 Arp2/3-mediated actin polymerization (Cooper et al., 1983; Doolittle et al., 2013a; Kouyama and
468 Mihashi, 1981). For this, we compared the effect of monomeric and dimeric ICD on WRC
469 activity using an optimized buffer in the pyrene-actin polymerization assay (**Figure 5—figure**
470 **supplement 1A**). The chemically inducible dimerization FKBP/FRB-ICD constructs (shown in
471 **Figure 3C**) allowed us to directly compare the monomeric vs. dimeric ICD by switching
472 between DMSO and rapamycin, instead of using different tags (**Figure 3—supplement figure**
473 **1C, D**). Importantly, rapamycin alone did not have any effect on actin polymerization (**Figure**
474 **5—figure supplement 1B**), allowing us to focus on the effect of dimerizing HPO-30 ICD.
475 Unexpectedly, we observed that HPO-30 ICD strongly inhibits Rac1-WRC-mediated actin
476 polymerization (**Figure 5A**, blue vs. purple curves), with the dimerized ICD exhibiting a more
477 potent effect (**Figure 5A**, solid vs. dashed curves). This effect was dose-dependent, with 10 μM
478 ICD having a stronger effect than 5 μM ICD **(Figure 5—figure supplement 1D)**. In contrast,
479 the dimerized FKBP/FRB tag at the highest concentration only had a mild effect (**Figure 5—**
480 **figure supplement 1D**, grey curve). Importantly, the presence of ICD did not nonspecifically
481 quench pyrene fluorescence from either G-actin or F-actin **(Figure 5—figure supplement 1C)**.
482 Therefore, the observed inhibition was due to HPO-30 ICD preventing actin polymerization.

483 Interestingly, we noticed that the ICD inhibited actin polymerization to a level lower than
484 the basal level of actin polymerization from Arp2/3 alone, indicating that the inhibitory effect
485 was likely not through WRC. This is supported by our observation that the ICD similarly
486 inhibited actin polymerization induced by the isolated, constitutively active WCA peptide, with
487 the dimerized ICD again showing more potent inhibition (**Figure 5B**). In fact, the HPO-30 ICD
488 was able to inhibit spontaneous actin polymerization in the absence of any activator, including
489 the Arp2/3 complex **(Figure 5C**, **Figure 5—figure supplement 1E)**. Therefore, our data suggest
490 that the inhibitory effect of the ICD is likely a direct effect on actin, rather than through WRC,
491 Rac1, WCA, or Arp2/3.

492 The strong, WRC-independent inhibitory effect of the ICD on actin polymerization made
493 it difficult to directly examine how ICD binding influences WRC activity. To overcome this

494 challenge, we reduced the ICD concentration to 1 μM to minimize its inhibitory effect. At this
495 concentration, we did not observe HPO-30 ICD activating WRC alone **(Figure 5D)**. Previous
496 studies on the WIRS-containing ICD from the cell adhesion membrane protein protocadherin 10
497 (PCDH10) found that the PCDH10 ICD itself could not activate WRC but could enhance WRC
498 activation induced by low concentrations of Rac1 (Chen et al., 2014a). We tested if HPO-30 ICD
499 might act similarly to PCDH10, enhancing activity when WRC is mildly activated by Rac1.
500 Interestingly, in this condition, we found that 1 μM monomeric ICD slightly, but robustly,
501 increased Rac1-WRC-mediated actin polymerization (**Figure 5E**, dashed blue vs. solid light pink
502 curves). Since only dimerized ICD can readily bind WRC, we speculated that the enhanced
503 activity was due to a small fraction of dimeric ICD existing in equilibrium with the monomeric
504 form (**Figure 4**, **Figure 4—figure supplement 1**). To test this hypothesis (while avoiding the
505 dominant inhibitory effect of rapamycin-dimerized ICD observed even at 1 μM, **Figure 5E**, solid
506 blue curve), we reduced the dimerized ICD concentration to 0.1 μM. Consistent with our
507 hypothesis, at this low concentration, the dimerized ICD similarly promoted Rac1-WRC-
508 medicated actin polymerization (**Figure 5E**, solid green curve). This activating effect was
509 specific to Rac1-activated WRC, as free WCA could not be further activated by dimerized ICD
510 (**Figure 5F**). Although we could not test higher concentrations of ICD due to its strong inhibitory
511 effect on actin polymerization, low concentrations of dimeric ICD could enhance Rac1-WRC
512 activity, suggesting ICD binding cooperates with Rac1 to promote WRC activation.
513 The cooperativity between Rac1 and the HPO-30 ICD in activating WRC suggests that
514 the ICD has a preference for binding to activated WRC. Supporting this hypothesis, our
515 equilibrium pull-down (EPD) assay showed that GST-ICD pulled down more WRC in the
516 presence of saturating concentrations of Rac1 (which was manifested by less WRC remaining in
517 the pull-down supernatant, **Figure 5— figure supplement 1G**, lane 2 vs. 4) (Yang et al., 2022).
518 Taken together, our data demonstrate that, while the HPO-30 ICD cannot activate the WRC by
519 itself, it can synergistically cooperate with Rac1 to promote WRC activation, similar to the
520 WIRS receptor PCDH10 (Chen et al., 2014a). Our unexpected finding that the HPO-30 ICD
521 strongly inhibits actin polymerization suggests that the ICD directly interacts with actin.
522

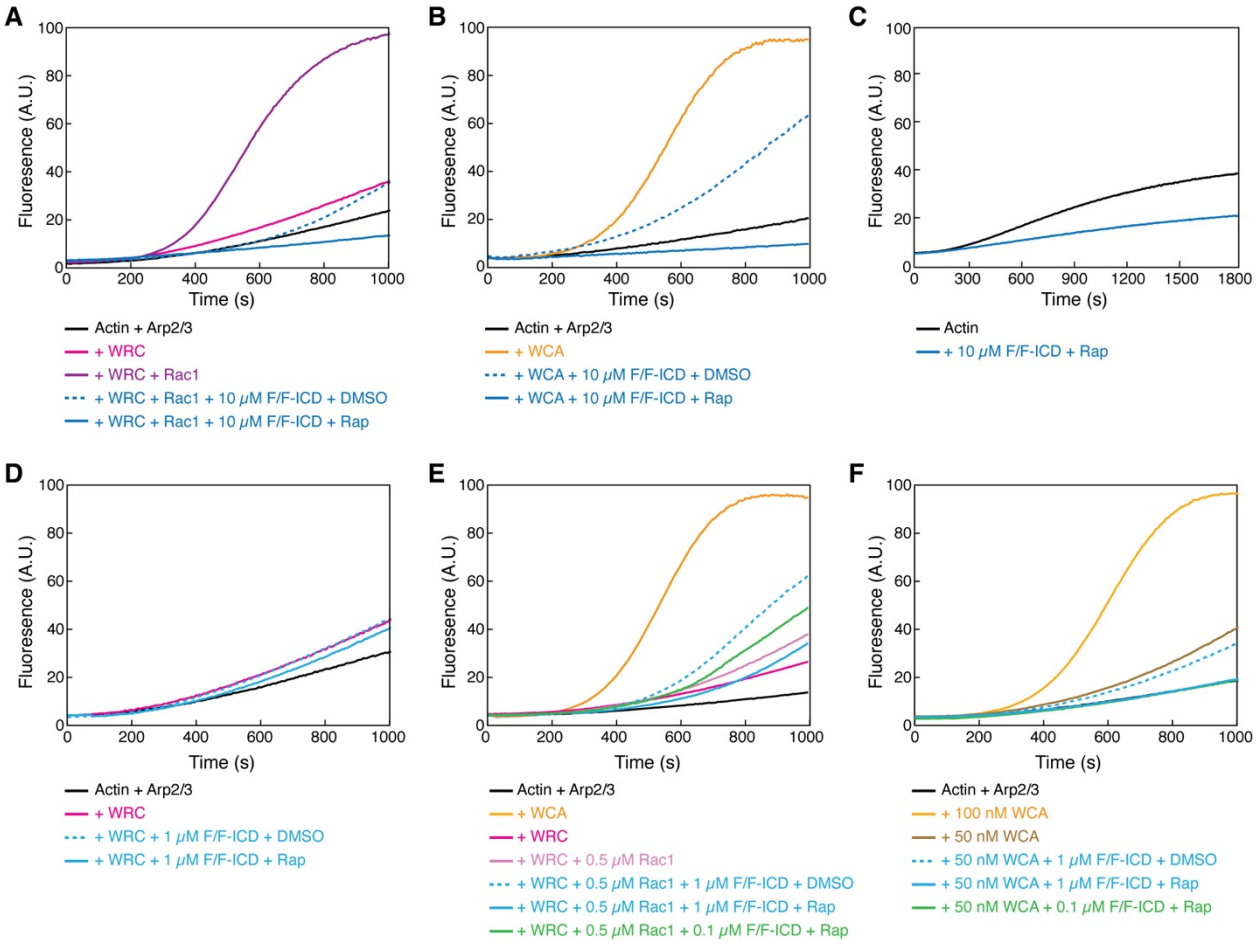

Figure 5. HPO-30 ICD inhibits actin polymerization but promotes Rac1-WRC activation. (A-F) Pyrene-actin polymerization assays of indicated conditions. Reactions contain 2 µM actin (10% pyrene-labeled) (A-B, D-F), 10 nM Arp2/3 complex, 100 nM WRC^{230WCA} or isolated WCA, $Rac1^{QP}$, indicated concentrations of equimolar GB1-FKBP-ICD and GB1-FRB-ICD, and 5 µM rapamycin or equal volume of DMSO. (C) contains 4 µM actin (5% pyrene-labeled), indicated concentration of equimolar GB1-FKBP-ICD and GB1-FRB-ICD, and 5 µM rapamycin.

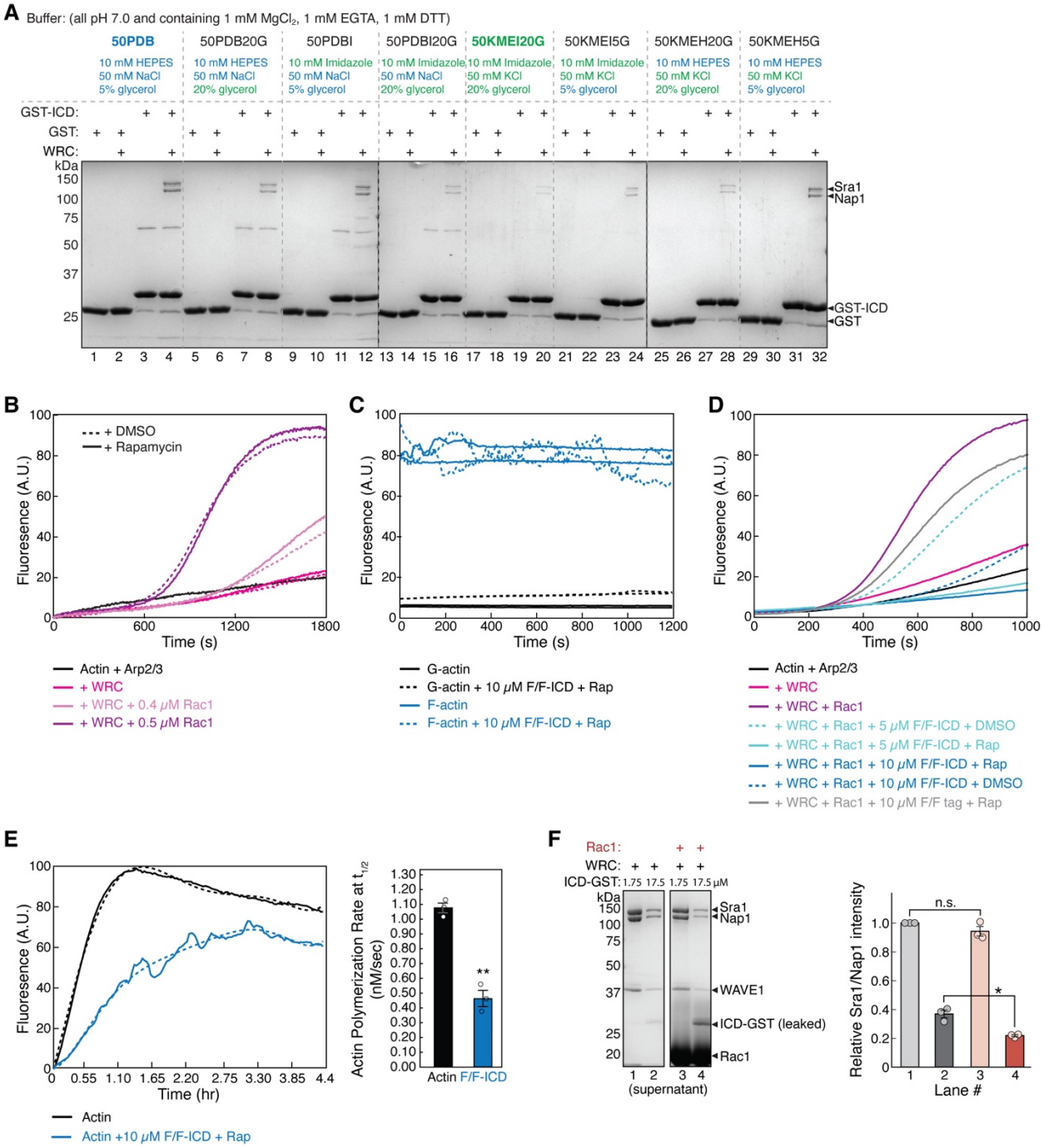

Figure 5—figure supplement 1. HPO-30 ICD inhibits actin polymerization. (A) Coomassie blue-stained SDS PAGE gels showing GST-ICD (200 pmol) pulling down WRC$^{230\Delta WCA}$ (150 pmol) in indicated buffer conditions, with 50PDB being the buffer used in the majority of pull-down reactions herein and 50KMEI20G being the buffer commonly used in pyrene-actin polymerization assays in previous studies of the WRC. All buffers contained 1 mM DTT and 0.05% Triton X-100. **(B)** Pyrene-actin polymerization assays showing rapamycin and DMSO did not affect WRC activity. Reactions contain 4 µM actin (5% pyrene-labeled), 10 nM Arp2/3 complex, 100 nM WRC^{230WCA}, Rac1^{QP}, and 5 µM rapamycin or equal volume of DMSO. **(C)** Fluorescence profiles of 4 µM actin (5% pyrene-

538 labeled) in the monomeric or polymerized state, with and without dimerized GB1-FKBP-ICD/GB1-FRB-ICD.
539 Reactions include 5 μM rapamycin. **(D)** Pyrene-actin polymerization assays of indicated conditions. Reactions
540 contain 2 μM actin (10% pyrene-labeled), 10 nM Arp2/3 complex, 100 nM WRC^{230WCA}, $Rac1^{QP}$, indicated
541 concentrations of equimolar GB1-FKBP-ICD and GB1-FRB-ICD, and 5 μM rapamycin or equal volume of DMSO.
542 Note that part of these data are also shown Figure 5A. **(E)** Left, long-term pyrene-actin polymerization assays,
543 containing 4 μM actin (5% pyrene-labeled), indicated concentration of equimolar GB1-FKBP-ICD and GB1-FRB-
544 ICD, and 5 μM rapamycin. Solid lines represent the actual data and dashed lines represent a fitted curve, using a
545 sixth-order polynomial fit from Excel, in order to derive reaction rate. **Right,** quantification of the actin
546 polymerization rate from (E) at $t_{1/2}$. **(F)** Coomassie blue-stained SDS PAGE gels (left) and quantification from three
547 independent repeats (right) showing the equilibrium pull-down of WRC^{230WCA} by two concentrations of ICD-GST in
548 the presence or absence of 40 μM $Rac1^{QP}$. Error bars represent standard error, * $p < 0.05$, from Student's paired t-
549 test.
550
551

552 **HPO-30 ICD binds to F-actin and inhibits actin depolymerization similar to CapZ**

553 The strong inhibitory effect of the HPO-30 ICD on actin polymerization suggests the ICD
554 could directly bind and sequester monomeric G-actin. However, we could not detect binding
555 between GST-ICD or dimerized F/F-ICD and G-actin (**Figure 6—figure supplement 1A, B**).
556 We next wondered if the ICD inhibited actin polymerization by binding to F-actin. In our F-actin
557 co-pelleting assay (Heier et al., 2017), we found that, compared to BSA, F/F tag, or the capping
558 protein CapZ (which only binds to the barbed ends of F-actin), F/F-ICD more robustly bound to
559 F-actin (**Figure 6A,B**). Interestingly, both the monomeric and dimeric F/F-ICD showed
560 significant binding to F-actin (**Figure 6A,B**, blue, +DMSO vs. +Rap), although the dimeric ICD
561 showed significantly stronger binding. This suggests that the monomeric ICD, while not as
562 effective in inhibiting actin polymerization as the dimeric form, is also capable of binding to
563 actin filaments. An equilibrium actin pelleting assay suggested a K_D of ~1.69 μM for the binding
564 between the dimerized ICD and F-actin **(Figure 6—figure supplement 1C)** (Avery et al., 2017).

565 To identify the critical region(s) of the ICD required for its interaction with actin
566 filaments, we introduced the same alanine scan mutations used in Figure 1 into both SNAP-
567 tagged FKBP-ICD and FRB-ICD constructs, which we used for all subsequent actin-related
568 experiments. Interestingly, we found that the same regions crucial for ICD's interaction with the
569 WRC **(Figure 1B)** and with itself **(Figure 4B,C)**, including Δ1, Δ5, Δ6, and Δ7, were also the
570 most essential for binding to F-actin **(Figure 6— figure supplement 1D,E)**.

571 The above data strongly suggest that the HPO-30 ICD inhibits actin polymerization by
572 directly binding to F-actin. Proteins with similar activity include capping proteins, such as CapZ.
573 Capping proteins bind to the barbed end of actin filaments to impede both actin polymerization
574 and depolymerization from the barbed end (Caldwell et al., 1989; Weeds and Maciver, 1993). To
575 test whether the HPO-30 ICD may function as a capping protein, we used a depolymerization
576 assay that is commonly utilized to measure CapZ activity (Caldwell et al., 1989; Cooper and
577 Pollard, 1985). We found that the ICD, like CapZ, inhibited actin depolymerization (**Figure
578 6C,D**). This inhibitory activity was both concentration- and dimerization-dependent, suggesting
579 that dimerization is critical for this capping-like activity. This aligns with our observation that
580 dimeric ICD more potently inhibited actin polymerization than monomeric ICD (**Figure 5**,
581 **Figure 5 – figure supplement 1E**). To determine which region(s) of the ICD are important for
582 this capping-like activity, we tested the same alanine scan mutations used in Figure 1 and Figure

583 6 – figure supplement 1D,E. As anticipated, the regions most critical for the depolymerization
584 activity of the ICD were the same as those crucial for binding to actin filaments **(Figure 6 –**
585 **figure supplement 1F-G)**. Collectively, our results suggest that the HPO-30 ICD behaves
586 analogously to capping proteins in obstructing both depolymerization and polymerization of F-
587 actin **(Figure 5**, **Figure 6)**.
588
589

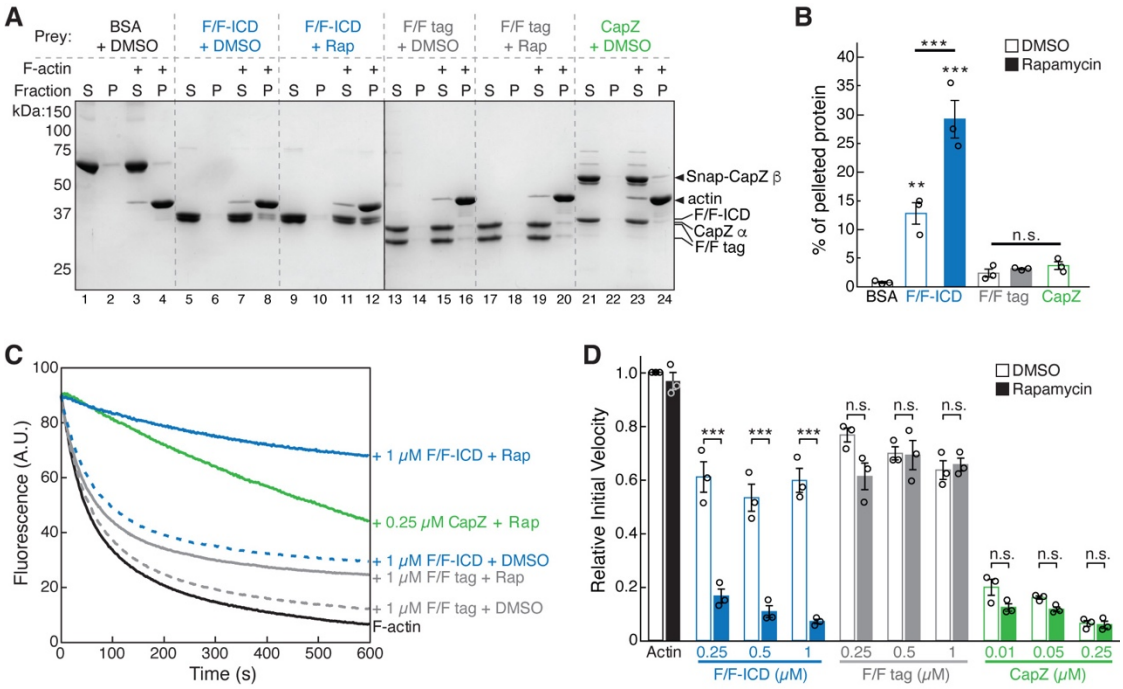

Figure 6. HPO-30 ICD binds to F-actin and inhibits actin depolymerization. (A) Representative Coomassie blue-stained SDS PAGE gels showing F-actin co-pelleting assays of indicated F/F-ICD and CapZ in the presence or absence of 5 μM rapamycin (or equal volume of DMSO). S: supernatant, P: pellet. **(B)** Quantification of (A) from three independent repeats, showing percentage of proteins in the pellet. Bars represent standard error, ** $p < .005$, *** $p < 0.001$, ANOVA with Tukey test. **(C)** Representative F-actin depolymerization assay fluorescence curves of indicated conditions. Each reaction contained 5 μM pre-polymerized actin (70% pyrene labeled), diluted 20-fold into depolymerization buffer containing indicated proteins in the presence or absence of 5 μM rapamycin (or equal volume of DMSO). **(D)** Quantification of the initial velocity of fluorescence curves shown in (C). Initial velocity was normalized to F-actin alone in the presence of DMSO. Error bars represent standard error, n = 3 independent repeats, *** $p < 0.001$, ANOVA with Tukey test.

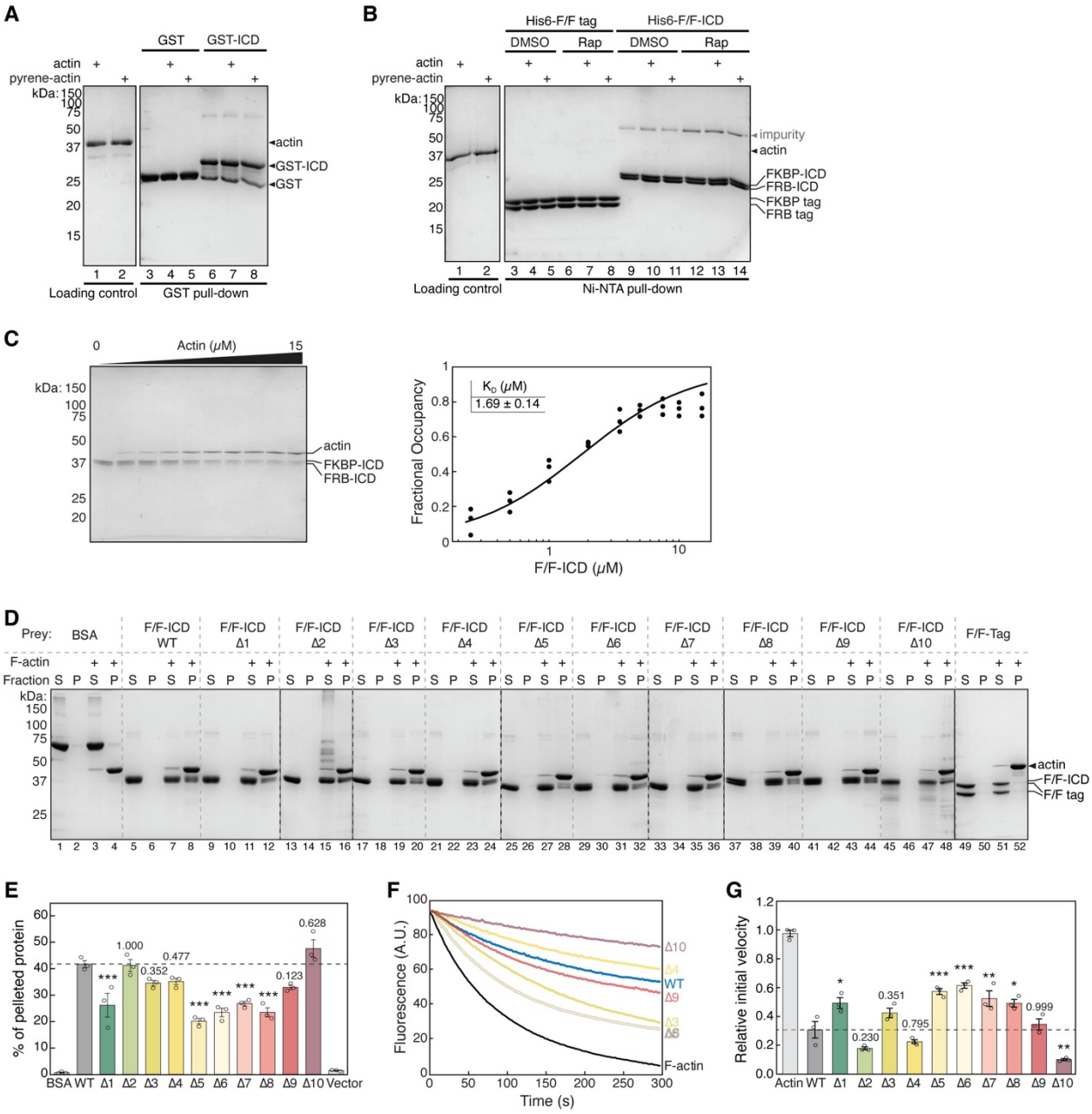

Figure 6—figure supplement 1. HPO-30 ICD binds to F-actin, but not G-actin, and inhibits F-actin depolymerization. (A-B) Coomassie blue-stained SDS PAGE gels showing GST-ICD (200 pmol) (A) or His6-F/F-ICD (300 pmol) (B) pulling down actin or pyrene labeled actin (500 pmol) in G buffer (2 mM Tris-HCl pH 8, 0.5 mM DTT, 0.2 mM ATP, 0.1 mM $CaCl_2$, 1 mM NaN_3), in the presence of 5 μM rapamycin (or equal volume of DMSO). **(C)** Representative Coomassie blue-stained SDS-PAGE gel (left) and quantification (right) of three independent actin pelleting assays to determine the dissociation constant of actin binding. Data were pooled from three independent repeats and fitted to a one-site binding model using DynaFit. **(D)** Representative Coomassie blue-stained SDS-PAGE gels of actin pelleting assays using SNAP-FKBP-ICD and SNAP-FRB-ICD alanine scan mutants (as shown in Figure 1A) from three independent experiments. Both FKBP and FRB contained the same

alanine scan mutation. **(E)** Quantification of (D) from three independent repeats, showing percentage of protein in the pellet. Bars represent standard error, *** $p < 0.001$, ANOVA with Tukey test. **(F)** Representative F-actin depolymerization assay fluorescence curves of indicated conditions from three independent experiments. Each reaction contained 5 μM pre-polymerized actin (70% pyrene labeled), diluted 20-fold into depolymerization buffer containing 200 nM of the indicated proteins in the presence of 5 μM rapamycin. Assays were performed using all ten SNAP-FKBP-ICD and SNAP-FRB-ICD alanine scan mutants (as shown in Figure 1A). Only several selected curves are shown here for clarity. Both FKBP and FRB contained the same alanine scan mutation. **(G)** Quantification of the initial velocity of F-actin depolymerization assays. Initial velocity was normalized to F-actin alone in the presence of rapamycin. Error bars represent standard error, n = 3 independent repeats, * $p < 0.05$, ** $p < 0.005$, *** $p < 0.001$, ANOVA with Tukey test.

623 **HPO-30 ICD binds to both the side and barbed end of actin filaments**

624 In the above bulk solution assays, the binding of the ICD to F-actin was not dependent on
625 dimerization (**Figure 6A,B**), but its inhibition of F-actin polymerization and depolymerization
626 was dependent on dimerization (**Figure 5A-C, 6C,D**). This suggests that the HPO-30 ICD may
627 have two distinct activities on actin filaments, with only the dimerization-dependent activity
628 resembling that of CapZ. This hypothesis could explain why more ICD co-pelleted with F-actin
629 than CapZ did (**Figure 6A,B**), as CapZ only binds to the barbed end of actin filaments (albeit
630 with high affinity) (Caldwell et al., 1989), while the ICD may bind to both the barbed end (in a
631 dimerization-dependent manner) and other surfaces of the actin filaments (in a dimerization-
632 independent manner).

633 To understand how the HPO-30 ICD binds F-actin, we used single-molecule total internal
634 reflection fluorescence (smTIRF) microscopy to directly visualize the interaction. For this assay,
635 we first attached a SNAP tag to the N-terminus of various FKBP/FRB constructs or the CapZ β-
636 subunit, and then labeled the SNAP tag using different SNAP-Surface® AlexaFluor® dyes
637 (hereafter referred to as AF followed by the corresponding excitation wavelength). Actin was
638 directly labeled with AF647 using previously established methods (Hansen et al., 2013). We
639 verified that the SNAP-tagged F/F-ICDs bound to the WRC in a rapamycin-dependent manner
640 and to a level similar to the GB1-tagged F/F-ICD, suggesting that the SNAP tag did not affect
641 ICD function (**Figure 7—figure supplement 1A**, lane 1-4). The labeled CapZ and F/F-ICD
642 proteins exhibited capping activity comparable to their counterparts used in bulk solution assays
643 (except for the AF647-labeled F/F-ICD, which was subsequently excluded from smTIRF assays
644 described below) (**Figure 7—figure supplement 1B,C**).

645 In the smTIRF experiments, $SNAP^{AF488}$-CapZ (at 5 nM) was found to stably bind to the
646 barbed end of filaments, and the binding stopped filament growth (**Figure 7A** top; **7C** green;
647 **Video 1,2**), consistent with the high affinity and very slow off-rate of CapZ at the barbed end
648 shown in previous studies (Caldwell et al., 1989). In contrast, $SNAP^{AF546}$-F/F-ICD (15 nM, with
649 8-fold molar excess of rapamycin) mainly bound to the side of actin filaments, instead of the
650 barbed end (**Figure 7A** bottom; **7B**; **Video 3-4**) (see below). While we occasionally observed an
651 ICD appearing to bind to the barbed end of a filament (see **Figure 7A** bottom for an example, at
652 time 39.0 s), the filament continued to grow beyond the bound ICD, leaving the ICD bound to
653 the same location on the filament. We could conclude that the ICD molecule bound to the

654 filament and not the PEG-coated surface, because it moved together with the filament (**Video**
655 **3,4**). By using stringent criteria to prevent misidentification of nonspecific background signals as
656 binding events, we found that 33% of filaments had at least one binding event for SNAP-F/F-
657 ICD over the 15-minute duration of the experiment, which was significantly higher than the
658 number of events for the SNAP-F/F tag under identical conditions (**Figure 6B**).
659 We found it difficult to increase the concentration of fluorescently labeled ICD to
660 observe more barbed end binding events, as this resulted in high background in smTIRF
661 experiments. Therefore, we used higher concentrations of unlabeled ICD to see if it could inhibit
662 actin filament growth as shown in the bulk solution assays in Figure 6C,D **(Figure 7C**; **Video 5)**.
663 We found that 1 μM dimerized F/F-ICD significantly decreased the actin elongation rate from
664 2.3 ± 0.5 subunits/sec to 1.5 ± 0.3 subunits/sec (Kuhn and Pollard, 2005) (**Figure 7C**, black vs.
665 solid blue). The same concentration of monomeric F/F-ICD also slowed down actin elongation,
666 but to a lesser extent (2.0 ± 0.4 subunits/sec) (**Figure 7C**, open blue). This could be due to either
667 the side-binding activity of ICD or the presence of dimeric ICD in equilibrium with monomeric
668 ICD, which could bind to the barbed end. Importantly, dimerized F/F tag did not significantly
669 affect actin polymerization (2.1 ± 0.4 subunits/sec) (**Figure 7C**, grey). Unfortunately, we could
670 not increase the unlabeled ICD concentration further to observe stronger inhibitory effects due to
671 limitations in the volume of high-concentration protein stock that we could add to the microfluid
672 chamber. In contrast, CapZ strongly inhibited actin polymerization, even at 5 nM (0.3 ± 0.1
673 subunits/sec). Further examination of the kymographs of individual actin filaments revealed that
674 in the absence of ICD or CapZ, filaments typically grew at a uniform rate. In the presence of
675 dimeric F/F-ICD, filaments grew more slowly and with occasional pausing (**Figure 7E**; **Figure 7**
676 **– figure supplement 2A,B)**. In the presence of CapZ, filaments exhibited almost no growth most
677 of the time over the course of the video (**Figure 7E**; **Figure 7 – figure supplement 2C).** Taken
678 together, our data suggest that HPO-30 ICD and CapZ have similar inhibitory effects on actin
679 filament elongation, although at the same concentration, the ICD exhibits less potent activity.
680 In the above smTIRF experiments, we encountered several technical challenges that
681 prevented us from observing stable binding of the ICD to the barbed end, in contrast to the stable
682 binding observed with CapZ. These challenges include: limited concentrations of fluorophore-
683 labeled ICD (nM, instead of μM that we could use in bulk solution assays), potential low affinity
684 and fast off-rate of the ICD binding to the barbed end, difficulty in distinguishing barbed end

685 binding from side binding due to light diffraction limit, lower than expected concentration of
686 dimeric ICD [the dissociation constant of FKBP-rapamycin binding to FRB is ~12 nM
687 (Banaszynski et al., 2005)], and fast binding/dissociation events potentially beyond the data
688 acquisition speed (50 or 100 ms exposure time). To further investigate whether the ICD binds to
689 the barbed end, we used a competition co-pelleting assay to determine if dimeric F/F-ICD could
690 compete with CapZ for binding to the barbed end of F-actin (**Figure 7D**). Our results showed
691 that the dimerized F/F-ICD, when applied at about ten times the concentration of CapZ,
692 significantly decreased CapZ binding by ~ 60%. In contrast, neither the monomeric F/F-ICD nor
693 the dimerized F/F tag had an impact on CapZ binding (**Figure 7D**). This result suggests that
694 dimeric ICD binds to the barbed end and can block CapZ binding, consistent with our findings
695 that dimeric ICD is more effective in inhibiting actin polymerization (**Figure 5A,B**) and
696 depolymerization (**Figure 6C,D**).
697 Combining our single molecule and bulk solution results, we conclude that HPO-30 ICD
698 monomers preferentially bind to the side of actin filaments, while dimers can bind to both the
699 sides and the barbed end of filaments. Only the barbed end binding by dimeric ICD can inhibit
700 actin filament growth in a manner similar to CapZ. These findings reveal a surprising function of
701 the HPO-30 ICD in directly regulating actin cytoskeletal remodeling.

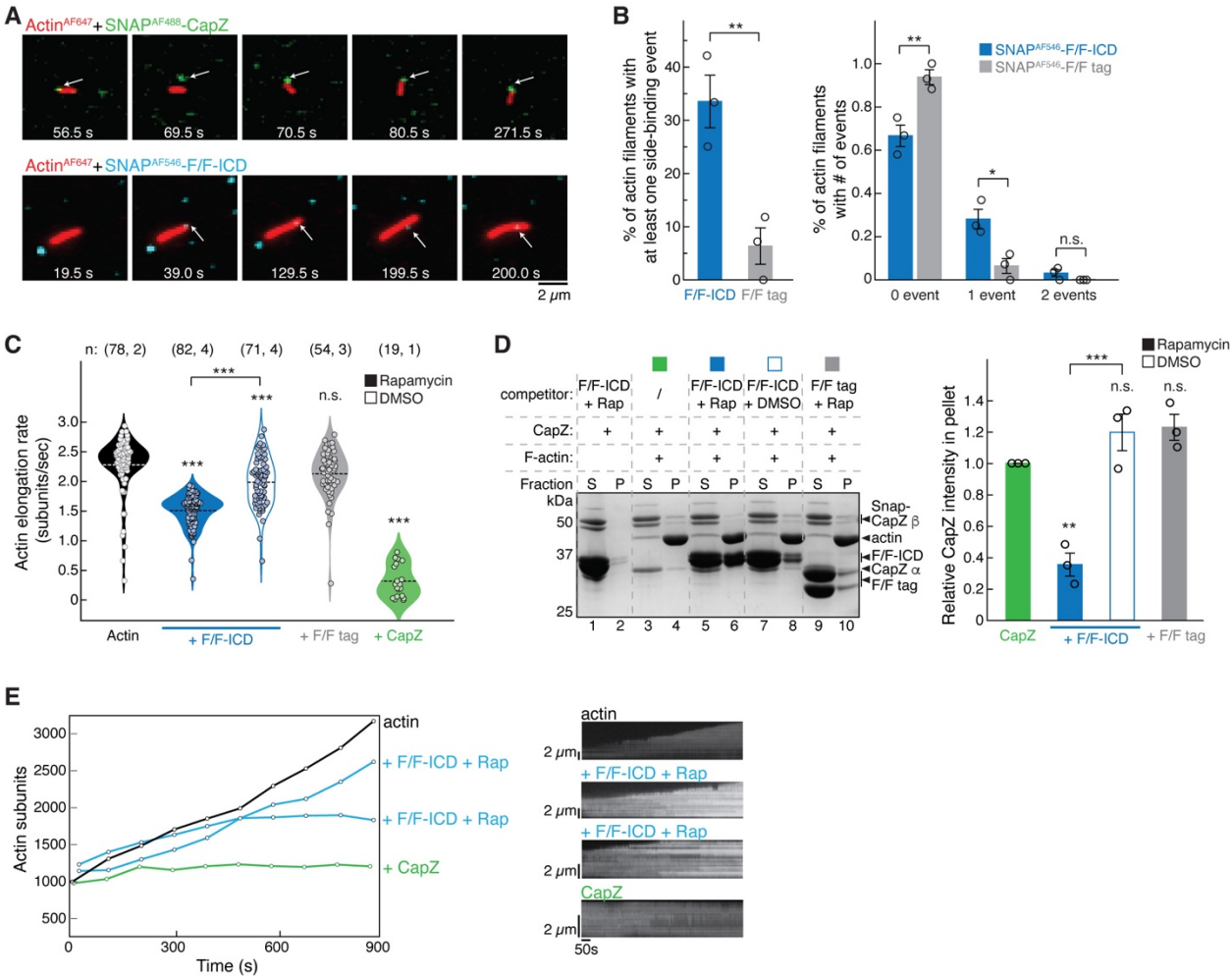

Figure 7. HPO-30 ICD binds both the side and barbed end of actin filaments and slows polymerization. **(A)** Examples of time lapse images from smTIRF experiments. Top: a capping event of SNAP^{AF488}-CapZ (green, 5 nM) and actin^{AF647} (red). Bottom: a side-binding event of SNAP^{AF546}-F/F-ICD (cyan, 15 nM) and actin^{AF647} (red). Note that in smTIRF time-lapses, sometimes a lag was observed between signals at the two channels. For example, in the top row, the filament and SNAP^{AF488}-CapZ puncta were displaced at 69.5 s, but aligned again at 70.5 s. The lagging was due to image acquisition conditions, where, to prevent photobleaching of AF647, images in the 640 nm-channel for actin^{AF647} were taken every 20 acquisitions of the 488 nm-channel for SNAP^{AF488}-CapZ (see Materials and Methods). **(B)** Quantification of the frequency of side binding events from smTIRF imaging. Left: comparison of overall side binding events. Right: comparison of the percentage of filaments with 0, 1, and 2 events. Data were from three independent repeats, at least 15 filaments per video. Bars represent standard error. * $p < 0.05$, ** $p < 0.01$, Student's paired t-test. **(C)** Violin plot of the elongation rate of actin filaments measured by smTIRF imaging. Total number of filaments pooled from the number of independent repeats for each sample are indicated in the paratheses on top of each column, respectively. *** $p < 0.001$, ANOVA with Tukey test. **(D)** Representative Coomassie blue-stained SDS PAGE gel (left) and quantification of pelleted CapZ from three independent repeats (right) showing F-actin (2 μM) co-pelleting

718 with CapZ (0.6 μM), with the indicated F/F-ICD or F/F tag as a competitor (5 μM) in the presence or absence
719 of 5 μM rapamycin (or equivalent volume DMSO). S: supernatant, P: pellet. Bars represent standard error, **
720 $p < 0.01$, *** $p < 0.001$, ANOVA with Tukey test. **(E)** Left, representative traces of actin filament length
721 determined manually from individual frames. Filaments were chosen that were the closest to the average rate
722 of elongation, with one additional filament for the ICD reactions with a reduced elongation rate. Right,
723 kymographs of the filaments displayed on the left.
724
725

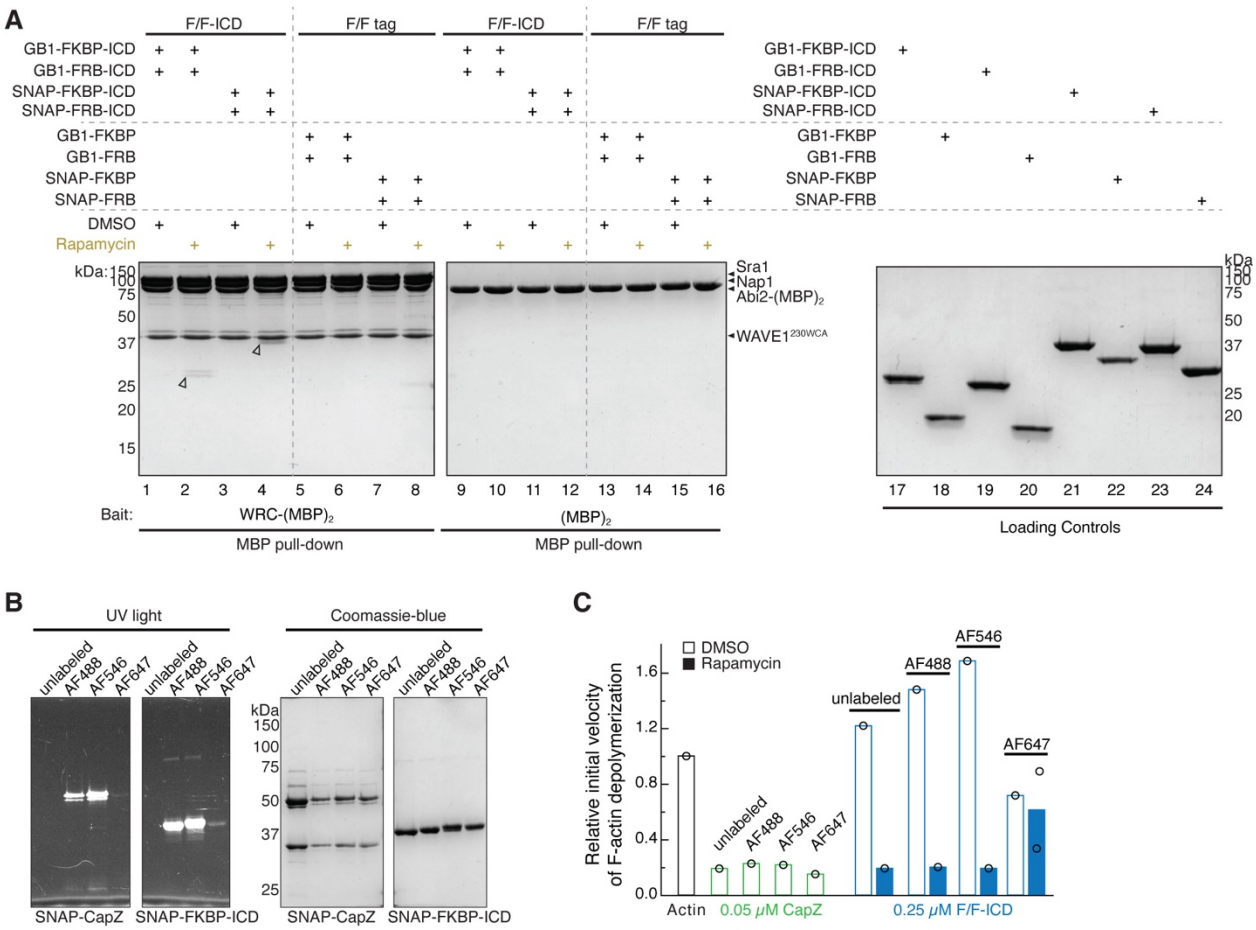

Figure 7—figure supplement 1. SNAP tag and fluorophore-labeling did not affect HPO-30 ICD function. **(A)** Coomassie blue-stained SDS PAGE gel showing WRC:Abi2-$(MBP)_2$ (60 pmol) pulling down GB1-tagged vs. SNAP-tagged HPO-30 ICD (600 pmol) in the presence or absence of 5 µM rapamycin. **(B)** SDS PAGE gels of SNAP-tag labeling of CapZ, FKBP-ICD, and FKBP tag with indicated SNAP-Surface© AlexaFluor© dyes. Left: UV light with Alexa-488 filter. Right: Coomassie blue stain. **(C)** Relative initial velocities from actin depolymerization assays of SNAP-Alexa labeled proteins, in conditions identical to Figure 6C,D.

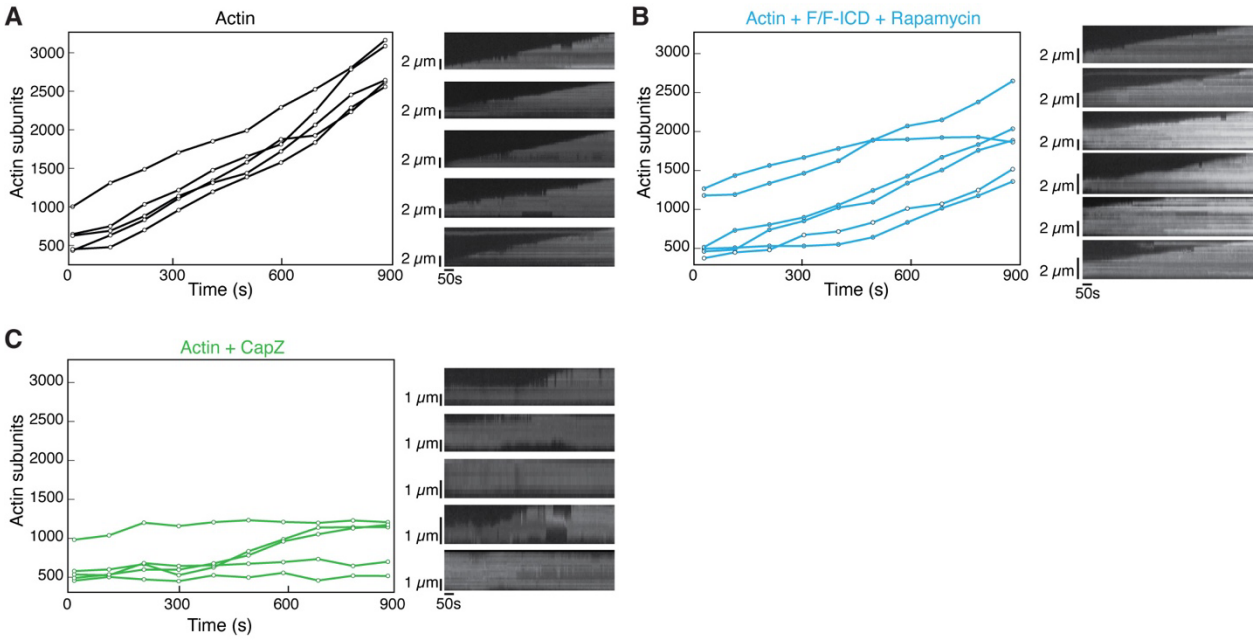

Figure 7—figure supplement 2. HPO-30 ICD affects actin polymerization rate. (A-C) Left, representative traces of actin filament length determined manually from individual frames. Displayed are filaments that were the closest to the average rate of elongation. Right, kymographs of the filaments displayed on the left.

738 **Discussion**

739 HPO-30 is a claudin-like membrane protein with a crucial role in higher order dendrite
740 branching in *C. elegans* PVD neurons (Smith et al., 2013; Tang et al., 2019; Zou et al., 2018,
741 2015). At branching sites, HPO-30 forms a co-receptor with the cell-adhesion transmembrane
742 protein DMA-1, which together transduce extracellular signals (from the epidermal proteins
743 SAX-7, MNR-1, and muscle secreted LECT-2) to the intracellular actin cytoskeleton (**Figure 8**,
744 left). Previous studies showed that this process required the HPO-30 intracellular domain (ICD)
745 to bind to the WRC, which in turn could activate Arp2/3 to generate branched actin networks to
746 deform the membrane and promote new dendrite formation (Zou et al., 2018). In this study, our
747 multifaceted analyses reveal two novel mechanisms employed by the HPO-30 ICD to regulate
748 local actin dynamics. First, the ICD undergoes dimerization to bind the WRC, which, in addition
749 to recruiting the WRC to local dendrite branching sites, can cooperate with Rac1 to enhance
750 WRC activation (**Figure 8**, step 2). This mechanism can work synergistically with DMA-1, as
751 the cytoplasmic tail of DMA-1 directly recruits the Rac-GEF, TIAM1, which would increase the
752 local concentration of active GTP-Rac1 (Zou et al., 2018). Second, the HPO-30 ICD directly
753 binds to actin filaments to modulate actin dynamics, with monomeric and dimeric forms binding
754 to the side of filaments, and the dimeric ICD alone binding to the barbed end to inhibit both actin
755 polymerization and depolymerization, similar to CapZ activity (**Figure 8**, step 1 and 2). These
756 seemingly contradictory actin regulatory mechanisms may enable exquisite control of local actin
757 dynamics necessary for dendrite branching (**Figure 8**, right, and see discussion below).

758 HPO-30 presents a unique example of a transmembrane protein capable of interacting
759 with the WRC, distinct from the previously identified WIRS peptide-containing receptors such
760 as SYG-1, Robo, DCC, Neogenin, TMEM132, neuroligins, and various protocadherins
761 (Chaudhari et al., 2021; Chia et al., 2014; Fan et al., 2018; Lee et al., 2016; Wang et al., 2021;
762 Xing et al., 2018). Unlike these receptors, the HPO-30 ICD does not use a WIRS motif or a
763 similar short peptide motif to bind WRC. Instead, our structure-function analyses show that the
764 entire ICD sequence is necessary for binding to the WRC, and dimerization of the ICD is crucial
765 for this interaction. This novel WRC-binding mechanism should be conserved across animals, as
766 the HPO-30 ICD is present only in nematodes but can bind to both *C. elegans* and human WRCs
767 (Zou et al., 2018). Thus, HPO-30 represents a new class of transmembrane proteins that interact

768 with the WRC using a distinct mechanism from the WIRS-containing receptors identified
769 previously (Chen et al., 2014a).
770 Without a high-resolution structure of the ICD complexed with WRC, the exact
771 conformation that the ICD adopts and how dimerization mediates WRC binding remain to be
772 determined. Our computational and biophysical analyses consistently indicate that the
773 monomeric ICD contains transient helical structure, but it is overall predominantly disordered in
774 solution. Two possible mechanisms could explain how the ICD binds to WRC and why
775 dimerization appears important for the interaction. In the first mechanism, the ICD may have one
776 binding surface on the WRC. The dimerized ICD acts as one structural entity, which undergoes
777 induced folding and adopts a stable conformation to bind the WRC. Induced folding has been
778 proposed for many DNA-binding proteins and cell-signaling molecules, such as the interaction
779 between E-cadherin and ß-catenin or between *Tg*IST and STAT1 (Dyson and Wright, 2002;
780 Huang et al., 2022; Huber et al., 2001; Huber and Weis, 2001; Turjanski et al., 2008). In the
781 second mechanism, the ICD may have two separate binding surfaces on the WRC. Dimerization
782 tags attached to the ICD provide an avidity effect that promotes simultaneous binding of two
783 copies of ICD to the two surfaces on the same WRC. Because ICD can directly bind to another
784 ICD, we favor the first mechanism, but our data cannot rule out the second mechanism. The
785 above two mechanisms can also explain how the ICD binds to the barbed end of actin filaments
786 in a dimerization-dependent manner. Regardless of which mechanism is used, it is likely the ICD
787 adopts two distinct conformations when binding to WRC vs. binding to the barbed end of F-
788 actin. Such structural plasticity has been observed for signaling molecules with versatile
789 functions (Bürgi et al., 2016; Dishman and Volkman, 2018; Okuda et al., 2022). Resolving the
790 high-resolution structures and identifying the key residues responsible for each binding event
791 would allow us to differentiate the two functions of HPO-30 ICD more precisely.
792 The requirement of ICD dimerization for both WRC-binding and F-actin capping
793 suggests an intriguing mechanism of how HPO-30 regulates actin remodeling at dendrite
794 branching sites. Clustering of membrane receptors is a common mechanism to increase local
795 signaling molecule concentration (Johannes et al., 2018). The enrichment of HPO-30 at
796 developing PVD neuron dendrites correlates with the high level of F-actin in these branches (Zou
797 et al., 2018). In addition to increasing its local membrane density, clustering of HPO-30 may
798 facilitate dimerization of its ICD, which can in turn activate its ability to recruit the WRC and

799 cap actin filaments. This dimerization-mediated functional switch can help the cell to distinguish
800 signal from noise and achieve sharp spatiotemporal control of actin polymerization in response
801 to upstream stimuli. It is worth noting that the regions of the ICD that most dramatically affect its
802 ability to interact with another ICD are the same regions that are most important for binding to
803 WRC and binding/capping F-actin. This again support the idea that dimerization (or
804 oligomerization) is key to ICD function.

805 Our study indicates that the HPO-30 ICD has two functions upon binding to the WRC: 1)
806 recruiting the WRC to dendrite branching site membranes and 2) enhancing WRC activation by
807 Rac1. This dual action of binding and sensitizing the WRC has been observed in several WIRS-
808 containing receptors, such as PCDH10 and PCDH19, where WIRS peptide binding recruits the
809 receptor to the membrane while weak interactions from the flanking ICD sequences promote
810 WRC activation by Rac1 (Chen et al., 2014a). Since the HPO-30 ICD strongly inhibits actin
811 polymerization, it will be important to develop new assays to directly measure WRC activation,
812 such as tracking WCA release, to understand how HPO-30 ICD binding enhances WRC
813 activation by Rac1. As Rac1 activates the WRC by binding to two distinct sites located on the
814 Sra1 subunit (Chen et al., 2017; Ding et al., 2022a), it is possible that HPO-30 ICD promotes
815 Rac1-WRC activation by directly stabilizing Rac1 binding to either site or by destabilizing WCA
816 sequestration.

817 To our knowledge, HPO-30 represents the first transmembrane protein that possesses
818 actin capping (or capping-like) activity. The precise structural mechanism of how the dimeric
819 HPO-30 ICD binds to the barbed end of actin filaments remains to be determined. It is possible
820 that it binds to the same surface as CapZ. Alternatively, it might bind to a nearby surface that
821 could either sterically clash with or allosterically destabilize CapZ binding. Regardless, the dual
822 abilities of HPO-30 to promote WRC membrane recruitment and activation while also capping
823 actin filaments and inhibiting actin polymerization may seem contradictory at first glance.
824 However, capping activity, which is usually provided by cytosolic capping proteins like CapZ, is
825 known to be critical for Arp2/3-based actin dynamics in both bead motility assays *in vitro* and
826 many processes *in vivo* (Akin and Mullins, 2008; Miyoshi et al., 2006). Capping proteins can
827 stop long actin filament growth and simultaneously reserve G-actin by blocking its access to
828 barbed ends (Carlier and Pantaloni, 1997). In parallel, capping protein can also prevent the
829 barbed end from sequestering the WH2 sequence of WCA, which would otherwise deplete the

830 activity of WASP-family proteins (Co et al., 2007; Higgs et al., 1999). Together, by blocking the
831 barbed end, the capping activity stimulates the formation of new branches through Arp2/3 and
832 thus plays a crucial role in dynamically modulating the actin architecture to generate force
833 against the surface where actin is localized (Akin and Mullins, 2008; Funk et al., 2021) (**Figure**
834 **8**, step 2). In principle, the capping activity of the HPO-30 ICD should act similarly to stimulate
835 the formation of a highly branched actin network. Although the isolated ICD has apparently
836 lower capping activity compared to the canonical capping protein CapZ, it has the advantage of
837 concentrating the capping activity in the area immediately next to membranes, which can provide
838 a more focused control of actin dynamics.
839 In summary, our study establishes HPO-30 as a novel membrane receptor that, upon
840 dimerization, can directly integrate the activities of WRC-Arp2/3-mediated actin polymerization
841 and actin filament capping, distinguishing it from other WIRS-containing receptors and
842 canonical barbed end cappers like CapZ. These two distinct functions of HPO-30 provide an
843 intriguing model to explain how it regulates local actin dynamics to facilitate dendrite branching
844 in PVD neurons (**Figure 8**). The synergistic action of both functions would promote the
845 formation of highly branched actin networks, which help generate dendritic "swellings" observed
846 in PVD neurons immediately before dendrite branch outgrowth (**Figure 8**, step 3) (Shi et al.,
847 2021). This mechanism likely works in conjunction with other actin machinery in the cell to
848 achieve highly spatiotemporally controlled actin dynamics and neuronal cell branching.
849

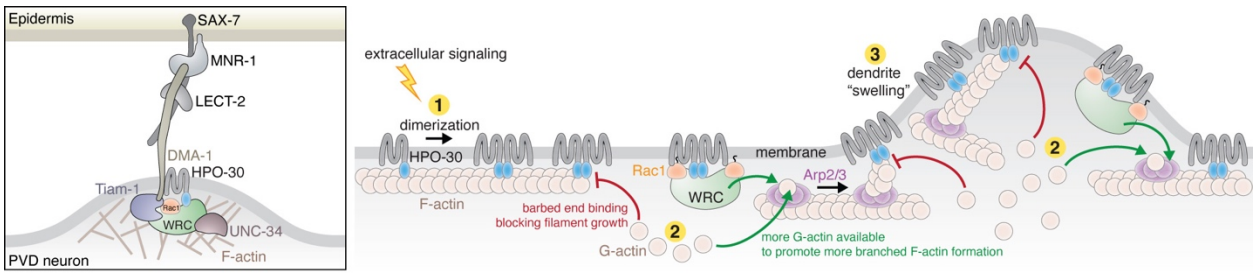

Figure 8. HPO-30 ICD integrates two distinct mechanisms to regulate actin dynamics during dendrite branching. Left, in *C. elegans* PVD neurons, a variety of molecules work together with the HPO-30/DMA-1 co-receptor to link extracellular signals to the intracellular actin network critical for driving dendrite branching. Right, model of how HPO-30 ICD modulates actin dynamics. In (1), HPO-30 on the dendrite membrane undergoes dimerization (or oligomerization). Both monomeric and dimeric forms of HPO-30 ICD can bind to the side of actin filaments, but only the dimeric ICD can bind to the fast-growing barbed end. In (2), dimeric ICD binding to the barbed end acts as a capping protein, which stops long filament growth and helps reserve G-actin for the Arp2/3 complex to produce short, branched actin filaments. In (2), dimeric ICD can also interact with the WRC. This recruits the WRC to the membrane and simultaneously promotes WRC activation by Rac1, which in turn stimulates Arp2/3 to produce branched actin filaments. In (3), the dual actions of HPO-30 ICD facilitate the formation of branched actin networks, which can help generate the "swelling" of dendrite observed in previous studies (Shi et al., 2021), an important indicator of the outgrowth of a new dendrite branch.

863 **Materials and Methods**

864 ***Protein expression and purification***

865 See Supplementary File 1 for amino acid sequences of recombinant proteins used in this
866 study. HPO-30 ICD proteins (and their associated alanine-scan mutants), including GST-ICD,
867 ICD-GST, DLC8-ICD-His6, GB1-ICD-His6, His9-sumo-ICD, MBP-ICD, GST-ICD-mEGFP,
868 GB1-FKBP-ICD-His6, GB1-FRB-ICD-His6, GB1-FKBP-His6, GB1-FRB-His6, SNAP-FKBP-
869 ICD-His6, SNAP-FRB-ICD-His6, SNAP-FKBP-His6, and SNAP-FRB-His6, as well as other
870 related proteins, including MBP-WAVE1 (1-230), MBP-WAVE1 (1-230)-WCA, MBP-WAVE1
871 (1-178), MBP-Abi2 (1-158), MBP-HSPC300, $(MBP)_2$-Abi2 (1-158), $(MBP)_2$-HSPC300, and
872 $Rac1^{Q61L/P29S}$ Δ4 (herein referred to as $Rac1^{QP}$), were individually expressed in Arctic Express
873 (DE3) RIL (Agilent) or BL21 (DE3) $T1^R$ (Sigma) cells after induction with 0.5-1 mM IPTG at
874 10 °C or 18 °C for 16 hours. His10-SNAP-CapZ β and CapZ α were expressed together from the
875 pCDFDuet vector (Novagen) in Arctic Express (DE3) RIL (Agilent) cells after induction with
876 0.75 mM IPTG at 10 °C for 16 hours. GST-ICD or ICD-GST (and alanine-scan mutants) and
877 GST-mEGFP were purified through Glutathione Sepharose beads (GE Healthcare), followed by
878 cation exchange chromatography using a Source 15S column (GE Healthcare) at pH 7.0. The
879 GST-ICD tryptophan mutations ("black" W22X) were purified through Glutathione Sepharose
880 beads (GE Healthcare), followed by dialysis into pull-down buffer containing 100 mM NaCl.
881 MBP-ICD (and associated W22R "black" mutant) was purified through amylose resin (New
882 England Biolabs), followed by cation exchange chromatography using a Source 15S column (GE
883 Healthcare) at pH 7.0. The GST tag from GST-ICD-mEGFP and the MBP tag from MBP-ICD
884 were removed using TEV cleavage at 4 °C overnight, followed by cation exchange
885 chromatography using a Source 15S column (GE Healthcare) at pH 7.0. DLC8-ICD-His6, GB1-
886 ICD-His6, His9-sumo-ICD, GB1-FKBP-ICD-His6 (and associated alanine mutants), GB1-FRB-
887 ICD-His6 (and associated alanine mutants), GB1-FKBP-His6, GB1-FRB-His6, GB1-His6, GB1-
888 homoCC-ICD-His6, SNAP-FKBP-ICD-His6, SNAP-FRB-ICD-His6, SNAP-FKBP-His6, and
889 SNAP-FRB-His6 were purified through Ni-NTA Agarose resin (Qiagen), followed by cation
890 exchange chromatography using a Source 15S column (GE Healthcare) at pH 7.0. The SNAP-
891 FKBP-ICD-His6 and SNAP-FRB-ICD-His6 alanine mutants were purified through Ni-NTA
892 Agarose resin (Qiagen), followed by dialysis into 50KMEH5Gd. GST-ICD, ICD-GST, DLC8-
893 ICD-His6, GB1-ICD-His6, His6-sumo-ICD, ICD-mEGFP, untagged ICD, untagged ICD W22R,

894 GB1-FKBP-ICD-His6 (and associated alanine mutants), GB1-FRB-ICD-His6 (and associated
895 alanine mutants), GB1-FKBP-His6, GB1-FRB-His6, GB1-His6, GB1-homoCC-ICD-His6,
896 SNAP-FKBP-ICD-His6, SNAP-FRB-ICD-His6, SNAP-FKBP-His6, SNAP-FRB-His6 were
897 further purified through a Superdex 75 column (GE Healthcare). His10-SNAP-CapZ β and CapZ
898 α were purified through Ni-NTA Agarose resin (Qiagen), followed by anion exchange
899 chromatography using a Source 15Q column (GE Healthcare) at pH 8.0 and size exclusion
900 chromatography on a Superdex 200 column (GE Healthcare). $Rac1^{QP}\Delta4$ was purified by an SP-
901 Sepharose Fast Flow column (GE Healthcare) at pH 7.0 followed by size exclusion
902 chromatography through a Superdex 75 column.
903 MBP-WAVE1, MBP-Abi2, MBP-HSPC300, $(MBP)_2$-Abi2, and $(MBP)_2$-HSPC300
904 proteins were purified through amylose beads (New England Biolabs). The Sra1/Nap1 dimer was
905 obtained by co-expressing His6-Sra1 and untagged Nap1 in Tni insect cells (Expression
906 Systems), followed by purification through Ni-NTA agarose resin (Qiagen) and anion exchange
907 chromatography using a Source 15Q column at pH 8.0. Pentameric WRC was assembled and
908 purified following previously described protocols (Chen et al., 2014b, 2010). Briefly,
909 individually purified WAVE1, Abi2, and HSPC300 subunits were mixed at equimolar ratio in
910 the presence of 1% (w/v) NP40 and incubated on ice for 48 hours. The assembled trimer was
911 then purified by anion exchange chromatography through a Source 15Q column at pH 8.0 and
912 cation exchange chromatography by a Source 15S column at pH 6.0. Dimer and trimer were
913 mixed at equimolar ratio and incubated on ice for 30 min. The assembled pentamer was purified
914 on amylose beads (NEB), after which the MBP and His6 tags were cleaved using TEV protease
915 incubation overnight. The pentamer was further purified using anion exchange chromatography
916 through a Source 15Q column at pH 8.0 and size exclusion chromatography using a Superdex
917 200 column.
918 Actin was purified as previously described from rabbit muscle acetone powder from Pel-
919 Freeze (Spudich and Watt, 1971). Actin was labeled by pyrene or Alexa Fluor® 647 after
920 polymerization at 4 °C, using a 10-fold or 2-fold excess dye, respectively. Actin and pyrene-
921 labeled actin used in actin polymerization and depolymerization assays were kept in continuous
922 dialysis at 4 °C, with buffer changes twice a week. Actin and Alexa Fluor® 647-labeled actin
923 used in smTIRF experiments were kept at 4 °C away from light for up to two weeks.
924

925 ***Generation of WRC-(MBP)$_2$***

926 To create WRC:Abi2-(MBP)$_2$, the sortase ligation sequence, LPGTG, was genetically
927 fused to the C-terminus of MBP-Abi2 (1-158). Meanwhile, a TEV site was added to the N-
928 terminus of an (MBP)$_2$ tag, which after Tev cleavage would expose a Gly required for sortase
929 ligation. MBP-Abi2 (1-158)-LPGTG was expressed, purified, and incorporated into the WRC as
930 described above to create WRC-LPGTG. GG-2MBP was expressed in Arctic Express (DE3) RIL
931 (Agilent) cells after induction with 0.75 mM IPTG at 10 °C for 16 hours, purified on amylose
932 resin, and subjected to TEV cleavage overnight, followed by anion exchange chromatography
933 using a Source 15Q column (GE Healthcare). Sortase5M (sortase A pentamutant) was a gift from
934 David Liu (Addgene plasmid # 75144), expressed in Arctic Express (DE3) RIL (Agilent) cells,
935 purified over Ni-NTA agarose resin, followed by cation exchange using a Source 15S column
936 (GE Healthcare) and size exclusion chromatography using a Superdex 75 column (GE
937 Healthcare) (Chen et al., 2011). WRC-LPGTG (1 μM) was mixed with GG-MBP (25 μM) and
938 sortase (10 μM) in 50 mM Tris pH 7.5, 150 mM NaCl, and 10 mM $CaCl_2$ and left at room
939 temperature for two hours. The reaction was quenched by adding 25 mM EGTA, and the WRC-
940 (MBP)$_2$ was purified over a Superdex 200 column to separate the WRC-(MBP)$_2$ from unligated
941 molecules and sortase.
942

943 ***Regular pull-down assay***

944 GST pull-down assays were performed as previously described (Shi et al., 2021). Briefly,
945 20 μL of GSH-Sepharose beads were mixed with bait protein and prey protein in 1 mL of pull-
946 down buffer (50 mM NaCl, 10 mM HEPES pH 7.0, 5% (w/v) glycerol, 5 mM 2-
947 mercaptoethanol, and 0.05% Triton X-100). For reactions at alternative pH values, either 10 mM
948 MES pH 6.0 or 20 mM Tris pH 8.0 was used in place of HEPES. The samples were mixed at 4
949 °C for 30 minutes, washed three times with 1 mL of pull-down buffer, and eluted with 40 μL of
950 elution buffer containing 30 mM reduced glutathione and 100 mM Tris pH 8.5. MBP pull-down
951 assays were performed like GST pull-down assays, except that 20 μL of amylose resin was used,
952 and elution buffer included 2% (w/v) maltose. His-tagged pull-down assays were performed as
953 above, used 20 μL of Ni-NTA agarose resin, G-Buffer (2 mM Tris HCl pH 8.0, 200 μM ATP,
954 0.5 mM DTT, 0.1 mM $CalCl_2$, and 1mM NaN_3) as the wash buffer. The elution buffer contained
955 500 mM imidazole pH 7.0. In all pull-down assays, the eluate was examined by SDS-PAGE and

956 Coomassie blue staining. In all pull-down assays using FKBP and FRB, rapamycin was added to
957 5 μM final concentration in all buffers. In control reactions, the same volume of DMSO was
958 added in place of rapamycin.
959 For the WRC alanine scan pull-down quantification (**Figure 1B**), the intensity of the Sra1
960 and Nap1 bands were quantified using ImageJ. The intensity from the GST control lane was
961 subtracted from the alanine protein lane, and the corrected intensity was divided by the intensity
962 of the GST-ICD band. This ratio was then divided by the ratio of the wild type HPO-30 lane. For
963 the MBP-ICD alanine scan pull-down quantification (**Figure 4A**), the intensity of the MBP-ICD
964 band was quantified using ImageJ and divided by the intensity of the GST-ICD band. The ratio
965 of the GST control was then subtracted from the ICD ratio. The corrected ratio was then set
966 relative to the WT ICD lane. For both the WRC and MBP-ICD alanine scan pulldowns, ANOVA
967 on Ranks and Dunn-Tukey tests were performed to determine significance.
968
969 ***Equilibrium pull-down (EPD) assay***
970 Equilibrium pull-down assays were performed as previously described (Chen et al.,
971 2017). Briefly, 60 μL of GSH-Sepharose beads (50% slurry equilibrated in pull-down buffer)
972 were mixed with 0.1 μM WRC and various amounts of GST-tagged protein (from 0.01 μM to 30
973 μM) and brought to 100 μL final reaction volume using pull-down buffer (composition the same
974 as in GST pull-down assays, above). The reactions were allowed to mix for 30 min at 4 °C, and
975 four reactions at a time were spun at 15 krpm for 15 seconds. The supernatant was removed and
976 examined by SDS-PAGE and Coomassie blue staining. Each assay was repeated 3 times. The
977 Sra1/Nap1 intensity was quantified using ImageJ to calculate the fractional occupancy. The data
978 from all repeats were pooled and globally fitted in DynaFit using a single binding site model
979 (Kuzmic, 1996).
980
981 ***Size exclusion chromatography analysis***
982 GB1-FKBP-ICD and GB1-FRB-ICD were mixed at equimolar ratio and loaded onto a
983 24-mL Superdex 200 column (GE healthcare) equilibrated in 100 mM NaCl, 10 mM HEPES pH
984 7.0, 5% (w/v) glycerol, and 1 mM DTT, with or without 5 μM rapamycin. Molecular weight was
985 determined by running molecular weight standards (Sigma Cat # MWGF200-1KT) in identical
986 buffer as the ICD proteins and generating a standard curve from the elution volumes.

987

988 ***Pyrene-actin polymerization assay***

989 Pyrene-actin polymerization assays were performed as previously described (Doolittle et
990 al., 2013a). Actin was purified and pyrene-labeled as described above and kept in continuous
991 dialysis in G-Buffer (2 mM Tris-HCl pH 8, 0.5 mM DTT, 0.2 mM ATP, 0.1 mM $CaCl_2$, 1 mM
992 NaN_3) that was changed twice a week. Arp2/3 was purified following existing protocols and kept
993 aliquoted at -80°C (Doolittle et al., 2013b). All proteins except for the WRC and Arp2/3 were
994 purified into 50KMEH5Gd (50 mM KCl, 1 mM $MgCl_2$, 1 mM EGTA, 10 mM HEPES pH 7.0,
995 5% [w/v] glycerol, 1 mM DTT) and stored at -80°C. WRC230VCA was purified into
996 100KMEI20Gd (100 mM KCl, 10 mM Imidazole pH 7.0, 20% [w/v] glycerol) and kept at -80°C.
997 Unless otherwise noted, a typical reaction contained 2 µM actin with 10% pyrene labeled, 10 nM
998 Arp2/3, 100 nM WRC^{230WCA} or free WCA, and /or 0.4 µM $Rac1^{QP}\Delta4$, and/or additional ICD
999 ligands to be analyzed, with or without 5 µM rapamycin or an equivalent volume of DMSO. For
1000 reactions in Figure 5C, reactions contained 4 µM actin with 5% pyrene labeling, with 5 µM
1001 rapamycin. The excitation and emission wavelengths were set to 365 nm and 407 nm,
1002 respectively, and data was collected every 2 seconds for 30 minutes. Pyrene quenching assays
1003 (Figure 5 – figure supplement 1C) were performed by mixing 4 µM actin with 5% pyrene
1004 labeling, either in the monomeric state or pre-polymerized by the addition of 50KMEH5Gd, with
1005 ICD and monitoring fluorescence over time. The long-term actin assays (Figure 5 – figure
1006 supplement 1 E) were assembled the same as for Figure 5C, but data was collected every two
1007 minutes over the course of 16 hours. The polymerization rate at $t_{1/2}$ was obtained by programs at
1008 https://biochempy.bb.iastate.edu/, which uses the same algorithm as described in (Padrick et al.,
1009 2008). Data were collected on a TECAN SPARK plate reader.

1010

1011 ***Actin depolymerization assay***

1012 Actin depolymerization assays were performed as previously described, with some
1013 modifications (Heiss and Cooper, 1991). Actin at ~20 µM and 70% pyrene-labeling was pre-
1014 polymerized at room temperature overnight by addition of 1 mM $MgCl_2$ and 50 mM KCl. For
1015 each depolymerization reaction, actin was diluted to 5 µM in one pooled mixture, either alone or
1016 with proteins to be tested, and left for 3 minutes at room temperature to allow for protein
1017 binding. Protein at the same concentration was prepared in a second, separate mixture. After 3

1018 minutes, the actin was further diluted 20-fold by the addition of the second mixture. All proteins
1019 were diluted into depolymerization buffer, which is 3 parts G-Buffer and 1 part 50KMEH5Gd
1020 (see above for buffer composition). The excitation and emission wavelengths were set to 365 nm
1021 and 407 nm, respectively. Data were collected on a TECAN SPARK plate reader. To calculate
1022 the relative initial velocity, the slope for the first 30 seconds of the reaction was calculated and
1023 divided by the slope of the actin control. ANOVA on Ranks and Dunn-Tukey tests were
1024 performed to determine significance.
1025
1026 ***Circular dichroism (CD) measurement***
1027 Untagged HPO-30 ICD was purified into 100 mM NaCl, 10 mM HEPES pH 7.0, 5%
1028 (w/v) glycerol, and 1 mM DTT. The same buffer was used to dissolve BSA powder (Fisher Cat #
1029 BP1600-100) and to blank the CD spectrometer. The blank buffer was degassed by sonication
1030 for 3 minutes at 30% power. Data were collected on a MOS-500 circular dichroism spectrometer
1031 using an ALX250 lamp. Data were collected for wavelengths between 190 nm and 260 nm, with
1032 a 1 nm step, 0.5 s acquisition period, and averaged over three repeats. Mean residue ellipticity
1033 was calculated as described previously (Greenfield, 2006). Data for BSA and HPO-30 were
1034 collected at the same concentration of protein. TMAO was dissolved to 3 M in the same buffer as
1035 HPO-30 and was added to the appropriate concentration before measurement. Separate buffer
1036 blanks containing the same concentration of TMAO were measured to ensure TMAO alone did
1037 not contribute to the spectrum.
1038
1039 ***Nuclear magnetic resonance (NMR) spectroscopy***
1040 Isotopically labeled proteins were expressed and purified as described for non-labeled
1041 proteins, using minimal media containing either N^{15} NH_4Cl or N^{15} NH_4Cl and C^{13} glucose
1042 instead of traditional media. Proteins were purified into 100 mM NaCl, 10 mM HEPES pH 7.0,
1043 5% (w/v) glycerol, 1 mM DTT and were supplemented with 10% D_2O. Protein concentration
1044 ranged from 70 µM (GB1 tag) to 850 µM (GB1-ICD). GB1 tag was produced by thrombin
1045 cleavage of GB1-ICD and removal of ICD using nickel-NTA resin (Qiagen). NMR spectra were
1046 collected on a Bruker 700 MHz spectrometer at Iowa State University equipped with z-shielded
1047 gradient triple resonance 5 mm TCI cryoprobe. 2D ^1H-^{15}N TROSY-HSQC and ^1H-^{15}N HSQC
1048 experiments were recorded with a time domain matrix consisting of 100* (t_1, ^{15}N) × 1024* (t_2,

1049 ^{1}H) complex points with acquisition time of 50 ms (t_1) and 91.8 ms (t_2) using 16 scans per FID
1050 and 1.5 s interscan delay. Spectral widths for ^{1}H and ^{15}N dimensions were set to 15.9 and 28.2
1051 ppm, respectively, with carriers set at 4.821 ppm (^{1}H) and 119.138 ppm (^{15}N). Sequential
1052 ^{1}H/^{15}N/^{13}C backbone assignments of the ICD were achieved using conventional 3D triple
1053 resonance correlation experiments [HNCO, HNCA, and HN(CO)CA] at 700 MHz. Secondary
1054 ^{13}Cα chemical shifts were calculated using Poulsen's random coil database with corrections for
1055 pH, temperature, and neighbor amino acid correction (Kjaergaard et al., 2011; Kjaergaard and
1056 Poulsen, 2011). All spectra were processed using NMRPipe (Delaglio et al., 1995) and displayed
1057 with SPARKY (Lee et al., 2015).
1058
1059 ***Fluorophore labeling of proteins***
1060 SNAP-tagged proteins were labeled with SNAP-Surface® Alexa Fluor® 488, SNAP-
1061 Surface® Alexa Fluor® 546, and SNAP-Surface® Alexa Fluor® 647 (New England Biolabs).
1062 Protein (5 μM) and dye (10 μM) were mixed and allowed to react in 50KMEH5Gd at room
1063 temperature for 2 hours. Labeled proteins were desalted into 50KMEH5Gd buffer and
1064 concentrated. Extinction coefficients of fluorophores were calculated from a standard curve and
1065 are as follows: Alexa 488 at 495 nm, 95000 $M^{-1}*cm^{-1}$; Alexa 546 at 556 nm, 120000 $M^{-1}*cm^{-1}$;
1066 Alexa 647 at 650 nm, 255000 $M^{-1}*cm^{-1}$. Protein labeling efficiency was calculated by dividing
1067 protein concentration by dye concentration—for Alexa Fluor® 488 the labeling efficiency was
1068 estimated at ~100%, for Alexa Fluor® 546 the labeling efficiency was estimated at ~60%.
1069
1070 ***smTIRF data collection***
1071 All time lapses were collected on a Nikon TE2000-E inverted microscope equipped with
1072 a 100x 1.49 NA TIRF objective and a TIRF Quad filter cube (Chroma C141789), using an Andor
1073 iXon3 EM-CCD (DU-897-CS0) camera, with a GATACA iLas system to prevent uneven
1074 illumination. Coverslips were prepared as described previously with slight modifications
1075 (Narvaez-Ortiz and Nolen, 2022). Briefly, glass coverslips (VWR Cat # 48393-241) were
1076 cleaned with 2% (w/v) Hellmanex, acetone, and 1 M KOH solutions with sonication, and rinsed
1077 extensively with DI water before each step and after the KOH treatment. Coverslips were rinsed
1078 with methanol and dried using a N_2 gas stream. GOPTES (Fisher Cat # G0210100G) was added
1079 to the coverslips, which were then baked at 75°C for 30 minutes. Coverslips were rinsed with

1080 microscope-grade acetone and dried with N_2 gas stream. A 2% (w/w) Biotin-PEG3000/NH2-
1081 PEG3000 mixture of powder (Rapp Polymere GmbH) was prepared, placed on top of the
1082 coverslips, and the coverslips baked overnight at 75°C. After overnight baking, the coverslips
1083 were washed with water and dried with N_2 gas. Individual wells were made by placing
1084 functionalized coverslips on Ibidi® sticky-Slide IV 0.4 slides (Ibidi Cat # 80608). Individual
1085 lanes were prepared for microscopy by incubating with 5% (w/v) Pluronic F-127 for 10 min at
1086 RT, followed by either 100 nM (for elongation rate analysis) or 35 nM (for side binding analysis)
1087 neutravidin incubation (in 50 mM Tris pH 7.5, 200 mM NaCl, referred to as LS TBS for short)
1088 for 10 min at RT, and either 10 nM (for elongation rate analysis) or 3.5 nM (for side binding
1089 analysis) biotinylated myosin (in LS TBS) incubation for 10 min at RT. The chambers were
1090 washed with 20 mg/mL BSA in 50 mM Tris pH 7.5, 600 mM NaCl, and incubated with 20
1091 mg/mL BSA in LS TBS for 10 min at RT. Actin was diluted to a final concentration of 2.1 μM
1092 with 20% Alexa-647 labeling in 1X TIRF buffer (final concentrations: 50 mM KCl, 2 mM
1093 $MgCl_2$, 2 mM EGTA pH 8.0, 10 mM Imidazole pH 7.0, 25 mM glucose, 1 mM Trolox, 0.5%
1094 methylcellulose (400 cP), 20 mM 2-mercaptoethanol, 0.4 mM ATP, 20 mg/mL BSA, 0.02
1095 mg/mL catalase, 0.1 mg/mL glucose oxidase, 1 mM 4-nitrobenzyl alcohol, and 0.5 mM propyl
1096 gallate) and allowed to polymerize on the slide for 5 minutes at room temperature. Excess actin
1097 was removed by two washes, each time using 40 μL of 1X TIRF buffer. A separate mixture of 1
1098 μM actin with 20% Alexa-647 labeling containing desired proteins in 1X TIRF buffer was then
1099 added to the wells to start data acquisition. Time lapse images were acquired using the following
1100 setups. Experiments involving unlabeled HPO-30 ICD and CapZ for elongation rate analysis of
1101 $actin^{AF647}$: 640-nm laser, 5% power, 50 ms exposure time, and a 5-s interval between exposures;
1102 experiments involving $CapZ^{AF488}$: 488-nm laser (15% power, 50 ms exposure time) and 640-nm
1103 laser (5% power, 50 ms exposure time), alternating between 20 consecutive exposures in the
1104 488-nm channel for $CapZ^{AF488}$ and one exposure in the 640-nm channel for $actin^{AF647}$, with a
1105 500-ms interval between exposures; experiments involving HPO-30 ICD^{AF546}: 561-nm laser
1106 (10% power, 50 or 100 ms exposure time) and 640-nm laser (5% power, 50 ms exposure time),
1107 alternating between 20 consecutive exposures in the 561-nm channel for ICD^{AF546} and one
1108 exposure in the 640-nm channel for $actin^{AF647}$, with a 500-ms interval between exposures.
1109

1110 ***smTIRF data processing - actin elongation rate measurement***

1111 Time lapses were opened in ImageJ and the background removed using a rolling ball radius of 10
1112 pixels. The length of actin filaments was calculated using the Filament Length ImageJ plugin,
1113 kindly provided by Jeff Kuhn, using a Gaussian-Radius of 1.5-2, determined for each individual
1114 movie (Kuhn and Pollard, 2005). The length (in microns) was converted to subunits using the
1115 established value of 370 actin subunits / µm (Huxley and Brown, 1967). Time points were taken
1116 from the NIS Elements software. Filaments were only selected if they were present within the
1117 first 10 frames of the movie and did not leave the frame during the course of the video. 10 time
1118 points were selected and the length at each point was calculated, and the average slope was used
1119 for the actin elongation rate. ANOVA with Dunn-Tukey tests were used to determine
1120 significance.
1121
1122 ***smTIRF data processing - side-binding/capping analysis***
1123 Time lapses were opened in ImageJ and the background removed using a rolling ball radius
1124 of 10 pixels. Only filaments present at the beginning of the videos and those that did not leave
1125 the frame during the duration of the video were selected. Analysis was performed in a single-
1126 blinded manner. Side binding events were determined if they met the following criteria: 1) the
1127 ICD/empty tag puncta must be present for more than one frame; 2) the ICD/empty tag puncta
1128 must move with the filament at least once; 3) the filament must not move away from the
1129 ICD/empty tag puncta; 4) the HPO-30/vector puncta must be smaller than a circle with a radius
1130 of 4 pixels. Capping events were confirmed by the absence of growth with puncta present and, if
1131 available, growth from the end capped after the puncta leaves the filament. A Student's t-test was
1132 used to determine significance between ICD and tag reactions.
1133
1134 ***Actin pelleting assay***
1135 Actin pelleting assays were performed based on previous protocols (Heier et al., 2017)
1136 with slight modifications. Actin was pre-polymerized at room temperature overnight by addition
1137 of 1X 50KMEH5Gd. Reactions (60 µL) were assembled by mixing 2 µM actin and 1 µM protein
1138 (in the same 50KMEH5Gd buffer), which were then allowed to bind at room temperature for 30
1139 minutes. Reactions were centrifuged at 100,000 g at 4 °C for 30 min in a Type 42.2 Ti rotor in a
1140 Beckman ultracentrifuge. 40 µL of the supernatant was removed and mixed with SDS PAGE
1141 loading buffer, and the remaining ~15 µL was removed and discarded. The pellet was dissolved

1142 by the addition of 40 µL of G-buffer, followed by brief pipetting and vortexing, and allowed to
1143 sit at room temperature for 5 min before the liquid was removed and mixed with SDS PAGE
1144 loading buffer. The intensity of the supernatant and pellet bands on SDS PAGE gels were
1145 measured using ImageJ. The total intensity of the supernatant and pellet bands, and the
1146 percentage of intensity from the pellet and the supernatant were calculated. The percentage of
1147 pelleted protein was calculated by subtracting the percentage of intensity from the pelleted
1148 protein in the absence of actin from the percentage of intensity from the pelleted protein in the
1149 presence of actin. For example, in Figure 6A, the intensity of BSA from lanes 1 and 2 was
1150 summed and the percentage of intensity from 1 and from 2 were calculated. This was repeated
1151 for lanes 3 and 4, then the percentage intensity of lane 2 was subtracted from lane 4. ANOVA
1152 with Dunn-Tukey tests were used to determine significance.
1153 To quantify the dissociation constant of F-actin binding, 0.2 µM F/F-ICD was mixed with
1154 increasing concentrations of polymerized actin and pelleted as described above. The
1155 concentration of F-actin was estimated to be the same as the concentration of G-actin. 40 µL of
1156 the supernatant was removed and mixed with SDS for visualization on a gel. The intensity of
1157 both F/F-ICD bands was quantified using ImageJ to calculate the fractional occupancy. The data
1158 was fitted in DynaFit using a single binding site model (Kuzmic, 1996).
1159
1160 ***Actin pelleting competition assays***
1161 Actin pelleting competition assays were performed nearly identically to the actin
1162 pelleting assay described above, except that after 30 minutes of incubation of 5 µM HPO-30 ICD
1163 proteins with 2 µM actin, 600 nM CapZ was added and incubated for 5 minutes before
1164 ultracentrifugation. The intensity of the top bands for CapZ in the pellet were calculated for all
1165 reactions and corrected for the intensity of CapZ pelleted without actin. The relative intensity
1166 was calculated by dividing the intensity of the lane by the intensity of the lane containing CapZ
1167 with actin alone. For example, in Figure 7D, the intensity of lane 2 was subtracted from lanes 4,
1168 6, 8, and 10. Then, the corrected intensity of lane 6, 8, and 10 was divided by the corrected
1169 intensity of lane 4. ANOVA with Dunn-Tukey tests were used to determine significance.
1170
1171 ***Tryptophan fluorescence assays***

1172 Untagged ICD and GB1 tag were purified into 50 mM NaCl, 10 mM HEPES pH 7.0, 5%
1173 (w/v) glycerol, 5 mM 2-mercaptoethanol (called 50 PDB, for pull-down buffer). Tryptophan
1174 powder (Sigma Cat # 73-22-3) and BSA (Fisher Cat # BP1600-100) were dissolved in the same
1175 buffer. Solutions were made at the correct concentrations (ranging from 0 to 50 μM) and an
1176 emission scan was measured from 320nm to 400nm. The absorption wavelength was set to
1177 243nm to minimize the fluorescence value and prevent the inner-filter effect from non-
1178 specifically reducing the emission values (Weitner et al., 2022). The excitation and emission slit
1179 widths were set to 3 nm. All measurements were performed on a Horiba Scientific FluoroMax
1180 spectrofluorometer in 3 mm quartz cuvettes (Starna Cells, Inc. Cat # 3-3.45-Q-3). Normalized
1181 peak fluorescent values were calculated by dividing the fluorescence value of the peak by the
1182 concentration of that sample.
1183 Untagged ICD "black" W22R was purified into 50 PDB. To measure the concentration,
1184 samples of a known concentration of WT ICD were run on a gel and used to make a standard
1185 curve. Experiments were performed as described above for ICD WT. To calculate the
1186 fluorescence of ICD WT + ICD "black" W22R, the fluorescence of ICD "black" W22R alone
1187 was subtracted from the fluorescence of ICD "black" W22R + ICD WT. Extra NaCl was added
1188 to the 200PDB samples to bring the final salt concentration to 200 mM NaCl.
1189
1190 ***Molecular dynamics simulations***
1191 All-atom MD simulations were performed for each structural model using the Condo
1192 cluster at the High-Performance Computing facility at Iowa State University. These simulations
1193 were conducted with GROMACS (Abraham et al., 2015) using the AMBER99SP-disp forcefield
1194 (Robustelli et al., 2018). The system was solvated in a triclinic simulation box with TIP4P water
1195 molecules. Bonds to hydrogen were constrained via the LINCS algorithm (Hess et al., 1997).
1196 Short-range electrostatic and Lennard-Jones interactions were calculated with a plain coulomb
1197 cutoff of 1.0 nm. The Particle Mesh Ewald (PME) scheme with grid spacing of 0.16 nm was
1198 utilized for long range electrostatic interactions (Essmann et al., 1995). Solvent and solute were
1199 separately coupled to a modified Berendsen thermostat (Velocity Rescale) with a reference
1200 temperature of 300 K and Parinello-Rahman barostat with a reference pressure of 1 bar.
1201 Minimization and equilibration were performed for 1 ns coupled to a Berendsen thermostat
1202 (Velocity-rescale) with a reference temperature of 300K and a reference pressure of 1 bar

1203 coupled to. After energy minimization and a 1 ns equilibration, the molecular dynamics
1204 simulations were carried out over 200 ns with 2 femtoseconds timesteps and leap-frog integrator.
1205

1206 ***S2 cell culture and transfection***

1207 Drosophila S2 cells were grown in Schneider's media (Thermo Fisher) supplemented with 10%
1208 heat-inactivated FBS (Life Technologies) and 50 U/mL penicillin-streptomycin (Thermo Fisher).
1209 Cells were transfected with Effectene (Qiagen) and 1ug of total plasmid (either Pactin>HPO-
1210 30:6xMyc (pXD384) or both Pactin>HPO-30:6xMyc (pXD384) and Pactin>HPO-30:HA
1211 (pXD226)).
1212

1213 ***Co-immunoprecipitation***

1214 S2 cells were harvested 72 hours after transfection. Cells were lysed in RIPA buffer (Thermo
1215 Fisher) with 1x Halt Protease Inhibitor Cocktail (Thermofisher) for 30 minutes on ice. Cell
1216 lysates were incubated with anti-HA affinity gel beads (Sigma E6779-1ML) for 1 hour at 4°C
1217 with rotation. Proteins were eluted at 80°C in NuPAGE LDS Sample Buffer (Life Technologies)
1218 supplemented with DTT (GoldBio) and detected using Western blot with mouse antibody to HA
1219 (1:1000, Sigma H3663), rabbit antibody to Myc (1:1000, Santa Cruz Biotechnology sc-789), and
1220 HRP-conjugated goat antibodies to mouse (1:20,000, Jackson Immuno Research).
1221

1222 **Acknowledgements**

1223 We thank ResearchIT at Iowa State University for installing AlphaFold 2 and AlphaFold
1224 Multimer; Daniel Boesch for help with submitting AlphaFold prediction tasks; Scott Nelson at
1225 Iowa State for guidance with CD spectroscopy; Xuefeng Wang at Iowa State for the initial setup
1226 of smTIRF experiments; Aubrey Sijo-Gonzales, Finlan Rhodes, Leyuan Loh, Ganesh Prasad,
1227 Simanta Mitra, and ResearchIT at Iowa State University for establishing a web-based application
1228 (*https://biochempy.bb.iastate.edu*) for data visualization; and Michael Rosen at UT Southwestern
1229 for sharing FKBP/FRB constructs. This work was supported by funding from the National
1230 Institutes of Health (R35 GM128786) and start-up funds from the Iowa State University and the
1231 Roy J. Carver Charitable Trust to B.C., National Institutes of Health (R35 GM136319) to B.J.N.,
1232 National Institutes of Health (R01 GM132561) to J.R., Howard Hughes Medical Institute and the
1233 National Institute of Neurological Disorders and Stroke (R01 NS082208) to K.S., and the National

Science Foundation Graduate Research Fellowship and a training grant from the National Institutes of Health to R.S.

Author contributions

B.C. conceived and oversaw the project. J.R. oversaw NMR experiments and MD simulations. B.N. oversaw single molecule experiments. D.A.K. purified proteins and performed biochemical experiments. D.A.K. performed AlphaFold predictions. D.A.K. and J.R. performed NMR measurements. D.A.K. and H.Y.N-O. performed single molecule TIRF experiments. R.S. performed co-immunoprecipitation experiments under the supervision of K.S. U.P. performed MD simulations under the guidance of J.R. D.A.K. and B.C. drafted the manuscript with assistance from all the authors.

Competing interests

The authors declare no competing interests.

Additional Information

All data generated in this study are available to the public. Additional correspondence and request for materials should be addressed to stone@iastate.edu.

Supplementary materials

Figure 1—figure supplement 1. Equilibrium pull-down assay of ICD-GST and WRC.

Figure 1—figure supplement 2. *Ab initio* structure prediction of HPO-30 ICD.

Figure 1—figure supplement 3. MD simulations of predicted ICD structures.

Figure 1—source data 1. The file contains the following folders:

1) unedited Figure 1 and raw gel images used in Figure 1.

2) raw data and statistical analysis shown in Figure 1B,D.

3) unedited Figure 1—figure supplement 1 and raw gel images used in Figure 1—figure supplement 1.

4) Pymol scene file containing all predicted structural models shown in Figure 1 and Figure 1—figure supplement 1.

1264 5) Pymol scenes of the individual starting and final conformations for all models used in MD
1265 simulations and RMSD values for each simulation.
1266
1267 **Figure 2—figure supplement 1.** HPO-30 ICD is largely disordered.
1268 **Figure 2—source data 1.** The file contains the following folders:
1269 1) raw 2D NMR spectra data shown in Figure 2B/C, which can be opened by commonly used
1270 NMR software, including NMRpipe (for processing) and Sparky (for visualization).
1271 2) raw CD spectra data shown in Figure 2E and Figure 2—supplement 1A.
1272 3) raw 3D NMR spectra data, including HNCO, HNCA, and HNCOCA experiments, used to
1273 generate the deviation plots in Figure 2D and Figure 2 – figure supplement 1F/G. These files can
1274 be opened using common NMR software, including NMRpipe (for processing) and Sparky (for
1275 visualization); an Excel sheet containing picked peak values and the assignments.
1276 4) unedited Figure 2—figure supplement 1 and raw gel images used in Figure 2—figure
1277 supplement 1.
1278 5) raw 2D NMR spectra data shown in Figure 2 – figure supplement 1D/E, which can be opened
1279 by commonly used NMR software, including NMRpipe (for processing) and Sparky (for
1280 visualization).
1281
1282 **Figure 3—figure supplement 1.** Protein quality control for dimerization experiments.
1283 **Figure 3—figure supplement 2.** HPO-30 ICD binding to WRC requires dimerization tags.
1284 **Figure 3—source data 1.** The file contains the following folders:
1285 1) unedited Figure 3 and raw gel images used in Figure 3.
1286 2) unedited Figure 3—figure supplement 1 and raw gel images used in Figure 3—figure
1287 supplement 1.
1288 3) raw gel filtration data shown in Figure 3—figure supplement 1C/E.
1289 4) unedited Figure 3—figure supplement 2 and raw gel images used in Figure 3—figure
1290 supplement 2.
1291
1292 **Figure 4 – figure supplement 1.** HPO-30 ICD can interact with itself.
1293 **Figure 4 – figure supplement 2.** Tryptophan fluorescence cannot be used to monitor the self-
1294 association of HPO-30 ICD.

1295 **Figure 4—figure supplement 3.** Structural predictions of HPO-30 ICD self-association.
1296 **Figure 4 – source data 1.** The file contains the following folders:
1297 1) unedited Figure 4 and raw gel images used in Figure 4.
1298 2) raw data and statistical analysis shown in Figure 4C.
1299 3) unedited Figure 4 – figure supplement 1 and raw gel images used in Figure 4 – figure
1300 supplement 1.
1301 4) unedited Figure 4 – figure supplement 2 and raw gel images used in Figure 4 – figure
1302 supplement 2.
1303 5) raw data used in Figure 4 – figure supplement 2A,B,D,E.
1304 6) Pymol scene file containing all predicted structural models shown in Figure 4—figure
1305 supplement 2.
1306 7) Pymol scenes of the individual starting and final conformations for all models used in MD
1307 simulations and RMSD values for each simulation.
1308
1309 **Figure 5—figure supplement 1.** HPO-30 ICD inhibits actin polymerization.
1310 **Figure 5—source data 1.** The file contains the following folders:
1311 1) raw pyrene-actin polymerization data shown in Figure 5A-F.
1312 2) unedited Figure 5—figure supplement 1 and raw gel images used in Figure 5—figure
1313 supplement 1.
1314 3) raw pyrene-actin polymerization data shown in Figure 5 – figure supplement 1 B-F
1315 4) gel quantification data shown in Figure 5G.
1316
1317 **Figure 6—figure supplement 1.** HPO-30 ICD binds to F-actin, but not G-actin, and inhibits F-
1318 actin depolymerization.
1319 **Figure 6—source data 1.** The file contains the following folders:
1320 1) unedited Figure 6 and raw gel images used in Figure 6.
1321 2) raw data and statistical analysis shown in Figure 6B-D.
1322 3) unedited Figure 6—figure supplement 1 and raw gel images used in Figure 6—figure
1323 supplement 1.
1324 4) raw data and statistical analysis shown in Figure 6B-D.
1325

1326 **Figure 7—figure supplement 1.** SNAP tag and fluorophore-labeling did not affect HPO-30 ICD
1327 function.
1328 **Figure 7 – figure supplement 2**. HPO-30 ICD affects actin polymerization rate.
1329 **Figure 7—source data 1.** The file contains the following folders:
1330 1) unedited Figure 7 and raw gel images used in Figure 7.
1331 2) raw data and statistical analysis shown in Figure 7B-D.
1332 3) raw data and kymographs for Figure7E.
1333 4) unedited Figure 7—figure supplement 1 and raw gel images used in Figure 7—figure
1334 supplement 1.
1335 5) raw data shown in Figure 7—figure supplement 1C.
1336 6) raw data and kymographs for Figure7 – figure supplement 2.
1337
1338 **Video 1. CapZ capping event example 1.** Related to Figure 6A, top. Time lapse of SNAP^{AF488}-
1339 CapZ (green) bound to the end of actin filaments (red) obtained by smTIRF microscopy. Video
1340 length of 1200 frames at 120 frames per second. The filament in the top left corner is the one
1341 showcased in Figure 6A, top.
1342
1343 **Video 2. CapZ capping event example 2.** Related to Figure 6A, top. Time lapse of SNAP^{AF488}-
1344 CapZ (green) bound to the end of an actin filament (red) obtained by smTIRF microscopy. Video
1345 length of 1800 frames at 120 frames per second.
1346
1347 **Video 3. HPO-30 ICD side binding event example 1.** Related to Figure 6A, bottom.
1348 SNAP^{AF546}-F/F-ICD (cyan) bound to the side of an actin filament (red) obtained by smTIRF
1349 microscopy. Video length of 1000 frames at 100 frames per second.
1350
1351 **Video 4. HPO-30 ICD side binding event example 2.** Related to Figure 6A, bottom.
1352 SNAP^{AF546}-F/F-ICD (cyan) bound to the side of an actin filament (red) obtained by smTIRF
1353 microscopy. Video length of 350 frames at 35 frames per second.
1354
1355 **Video 5. Actin elongation rate comparison.** Related to Figure 6C. Representative smTIRF time
1356 lapses used to quantify the elongation rate of actin filaments. Video shows a random selection of

1357 actin filaments from each condition tested. Video length of 15 minutes and 181 frames was
1358 compressed to 9 seconds.
1359
1360 **Supplementary File 1.** Amino acid sequences of recombinant proteins used in this study.
1361
1362

1363 **References**

1364 Abraham, M.J., Murtola, T., Schulz, R., Páll, S., Smith, J.C., Hess, B., Lindah, E., 2015. Gromacs: High
1365 performance molecular simulations through multi-level parallelism from laptops to supercomputers.
1366 SoftwareX 1–2, 19–25. https://doi.org/10.1016/j.softx.2015.06.001
1367 Adamczak, R., Porollo, A., Meller, J., 2004. Accurate prediction of solvent accessibility using neural
1368 networks-based regression. Proteins: Structure, Function and Genetics 56, 753–767.
1369 https://doi.org/10.1002/prot.20176
1370 Akin, O., Mullins, R.D., 2008. Capping Protein Increases the Rate of Actin-Based Motility by Promoting
1371 Filament Nucleation by the Arp2/3 Complex. Cell 133, 841–851.
1372 https://doi.org/10.1016/j.cell.2008.04.011
1373 Alekhina, O., Burstein, E., Billadeau, D.D., 2017. Cellular functions of WASP family proteins at a
1374 glance. J Cell Sci 130, 2235–2241. https://doi.org/10.1242/jcs.199570
1375 Avery, A.W., Fealey, M.E., Wang, F., Orlova, A., Thompson, A.R., Thomas, D.D., Hays, T.S., Egelman,
1376 E.H., 2017. Structural basis for high-affinity actin binding revealed by a β-III-spectrin SCA5
1377 missense mutation. Nat Commun 8. https://doi.org/10.1038/s41467-017-01367-w
1378 Banaszynski, L.A., Liu, C.W., Wandless, T.J., 2005. Characterization of the FKBP·Rapamycin·FRB
1379 Ternary Complex. J Am Chem Soc 127, 4715–4721. https://doi.org/10.1021/ja043277y
1380 Baskakov, I. V, Kumar, R., Srinivasan, G., Ji, Y., Bolen, D.W., Thompson, E.B., 1999. Trimethylamine
1381 N-Oxide-induced Cooperative Folding of an Intrinsically Unfolded Transcription-activating
1382 Fragment of Human Glucocorticoid Receptor*. Journal of Biological Chemistry 274, 10693–10696.
1383 https://doi.org/https://doi.org/10.1074/jbc.274.16.10693
1384 Begemann, A., Sticht, H., Begtrup, A., Vitobello, A., Faivre, L., Banka, S., Alhaddad, B., Asadollahi, R.,
1385 Becker, J., Bierhals, T., Brown, K.E., Bruel, A.L., Brunet, T., Carneiro, M., Cremer, K., Day, R.,
1386 Denommé-Pichon, A.S., Dyment, D.A., Engels, H., Fisher, R., Goh, E.S., Hajianpour, M.J., Haertel,
1387 L.R.M., Hauer, N., Hempel, M., Herget, T., Johannsen, J., Kraus, C., Le Guyader, G., Lesca, G.,
1388 Mau-Them, F.T., McDermott, J.H., McWalter, K., Meyer, P., Õunap, K., Popp, B., Reimand, T.,
1389 Riedhammer, K.M., Russo, M., Sadleir, L.G., Saenz, M., Schiff, M., Schuler, E., Syrbe, S., Van der
1390 Ven, A.T., Verloes, A., Willems, M., Zweier, C., Steindl, K., Zweier, M., Rauch, A., 2021. New
1391 insights into the clinical and molecular spectrum of the novel CYFIP2-related neurodevelopmental
1392 disorder and impairment of the WRC-mediated actin dynamics. Genetics in Medicine 23, 543–554.
1393 https://doi.org/10.1038/s41436-020-01011-x
1394 Bernhofer, M., Dallago, C., Karl, T., Satagopam, V., Heinzinger, M., Littmann, M., Olenyi, T., Qiu, J.,
1395 Schütze, K., Yachdav, G., Ashkenazy, H., Ben-Tal, N., Bromberg, Y., Goldberg, T., Kajan, L.,
1396 O'Donoghue, S., Sander, C., Schafferhans, A., Schlessinger, A., Vriend, G., Mirdita, M., Gawron,
1397 P., Gu, W., Jarosz, Y., Trefois, C., Steinegger, M., Schneider, R., Rost, B., 2021. PredictProtein -
1398 Predicting protein structure and function for 29 years. Nucleic Acids Res 49, W535–W540.
1399 https://doi.org/10.1093/nar/gkab354
1400 Bonneau, R., Tsai, J., Ruczinski, I., Chivian, D., Rohl, C., Strauss, C.E., Baker, D., 2001. Rosetta in
1401 CASP4: progress in ab initio protein structure prediction. Proteins Suppl 5, 119–126.
1402 https://doi.org/10.1002/prot.1170
1403 Bürgi, J., Xue, B., Uversky, V.N., van der Goot, F.G., 2016. Intrinsic Disorder in Transmembrane
1404 Proteins: Roles in Signaling and Topology Prediction. PLoS One 11, e0158594–e0158594.
1405 https://doi.org/10.1371/journal.pone.0158594
1406 Burianek, L.E., Soderling, S.H., 2013. Under lock and key: Spatiotemporal regulation of WASP family
1407 proteins coordinates separate dynamic cellular processes. Semin Cell Dev Biol 24, 258–266.
1408 https://doi.org/10.1016/j.semcdb.2012.12.005
1409 Caldwell, J.E., Heiss, S.G., Mermall, V., Cooper, J.A., 1989. Effects of CapZ, an Actin Capping Protein
1410 of Muscle, on the Polymerization of Actin. Biochemistry 28, 8506–8514.
1411 https://doi.org/10.1021/bi00447a036
1412 Carlier, M.-F., Pantaloni, D., 1997. Control of Actin Dynamics in Cell Motility. J Mol Biol 269, 459–467.

1413 Chaudhari, K., Gorla, M., Chang, C., Kania, A., Bashaw, G.J., 2021. Robo recruitment of the wave
1414 regulatory complex plays an essential and conserved role in midline repulsion. Elife 10, 1–35.
1415 https://doi.org/10.7554/ELIFE.64474
1416 Chaudhari, K., Zhang, K., Yam, P.T., Zang, Y., Kramer, D.A., Schlienger, S., Calabretta, S., Collins, M.,
1417 Srour, M., Chen, B., Charron, F., Bashaw, G.J., Carver, R.J., 2022. A human DCC variant causing
1418 mirror movement disorder reveals an essential role for the Wave regulatory complex in Netrin/DCC
1419 signaling. bioRxiv. https://doi.org/10.1101/2022.10.13.511954
1420 Chen, B., Brinkmann, K., Chen, Z., Pak, C.W., Liao, Y., Shi, S., Henry, L., Grishin, N. V., Bogdan, S.,
1421 Rosen, M.K., 2014a. The WAVE regulatory complex links diverse receptors to the actin
1422 cytoskeleton. Cell 156, 195–207. https://doi.org/10.1016/j.cell.2013.11.048
1423 Chen, B., Chou, H.-T., Brautigam, C.A., Xing, W., Yang, S., Henry, L., Doolittle, L.K., Walz, T., Rosen,
1424 M.K., 2017. Rac1 GTPase activates the WAVE regulatory complex through two distinct binding
1425 sites. Elife 6, 1–22. https://doi.org/10.7554/elife.29795
1426 Chen, B., Padrick, S.B., Henry, L., Rosen, M.K., 2014b. Biochemical reconstitution of the WAVE
1427 regulatory complex. Methods Enzymol 540, 55–72. https://doi.org/10.1016/B978-0-12-397924-
1428 7.00004-2
1429 Chen, I., Dorr, B.M., Liu, D.R., 2011. A general strategy for the evolution of bond-forming enzymes
1430 using yeast display. Proc Natl Acad Sci U S A 108, 11399–11404.
1431 https://doi.org/10.1073/pnas.1101046108
1432 Chen, Z., Borek, D., Padrick, S.B., Gomez, T.S., Metlagel, Z., Ismail, A.M., Umetani, J., Billadeau, D.D.,
1433 Otwinowski, Z., Rosen, M.K., 2010. Structure and control of the actin regulatory WAVE complex.
1434 Nature 468, 533–538. https://doi.org/10.1038/nature09623
1435 Cheng, P., Poo, M., 2012. Early events in axon/dendrite polarization. Annu Rev Neurosci 35, 181–201.
1436 https://doi.org/10.1146/annurev-neuro-061010-113618
1437 Chia, P.H., Chen, B., Li, P., Rosen, M.K., Shen, K., 2014. Local F-actin network links synapse formation
1438 and axon branching. Cell 156, 208–220. https://doi.org/10.1016/j.cell.2013.12.009
1439 Chou, F.-S., Wang, P.-S., 2016. The Arp2/3 complex is essential at multiple stages of neural
1440 development. Neurogenesis 3, e1261653. https://doi.org/10.1080/23262133.2016.1261653
1441 Conway, O.J., Carrasquillo, M.M., Wang, X., Bredenberg, J.M., Reddy, J.S., Strickland, S.L., Younkin,
1442 C.S., Burgess, J.D., Allen, M., Lincoln, S.J., Nguyen, T., Malphrus, K.G., Soto, A.I., Walton, R.L.,
1443 Boeve, B.F., Petersen, R.C., Lucas, J.A., Ferman, T.J., Cheshire, W.P., van Gerpen, J.A., Uitti, R.J.,
1444 Wszolek, Z.K., Ross, O.A., Dickson, D.W., Graff-Radford, N.R., Ertekin-Taner, N., 2018. ABI3
1445 and PLCG2 missense variants as risk factors for neurodegenerative diseases in Caucasians and
1446 African Americans. Mol Neurodegener 13, 1–12. https://doi.org/10.1186/s13024-018-0289-x
1447 Cooper, J.A., Pollard, T.D., 1985. Effects of Capping Protein on the Kinetics of Actin Polymerization.
1448 Biochemistry 793–799.
1449 Cooper, J.A., Walker, S.B., Pollard, T.D., 1983. Pyrene actin: documentation of the validity of a sensitive
1450 assay for actin polymerization. J Muscle Res Cell Motil 4, 253–262.
1451 https://doi.org/10.1007/BF00712034
1452 Dahl, J.P., Wang-Dunlop, J., Gonzales, C., Goad, M.E.P., Mark, R.J., Kwak, S.P., 2003. Characterization
1453 of the WAVE1 knock-out mouse: Implications for CNS development. Journal of Neuroscience 23,
1454 3343–3352. https://doi.org/10.1523/jneurosci.23-08-03343.2003
1455 Delaglio, F., Grzesiek, S., Vuister, G.W., Zhu, G., Pfeifer, J., Bax, A., 1995. NMRPipe: A
1456 multidimensional spectral processing system based on UNIX pipes*, Journal of Biomolecular NMR.
1457 Ding, B., Yang, S., Schaks, M., Liu, Y., Brown, A., Rottner, K., Chowdhury, S., Chen, B., 2022a.
1458 Structures reveal a key mechanism of WAVE Regulatory Complex activation by Rac1 GTPase.
1459 BioRxiv [Preprint], May 10. doi: 10.1101/2022.05.10.491380.
1460 Ding, B., Yang, S., Schaks, M., Liu, Y., Brown, A.J., Rottner, K., Chowdhury, S., Chen, B., 2022b.
1461 Structures reveal a key mechanism of WAVE regulatory complex activation by Rac1 GTPase. Nat
1462 Commun 13. https://doi.org/10.1038/s41467-022-33174-3

Dishman, A.F., Volkman, B.F., 2018. Unfolding the Mysteries of Protein Metamorphosis. ACS Chem Biol 13, 1438–1446. https://doi.org/10.1021/acschembio.8b00276

Dong, X., Liu, O.W., Howell, A.S., Shen, K., 2013. An extracellular adhesion molecule complex patterns dendritic branching and morphogenesis. Cell 155, 296. https://doi.org/10.1016/j.cell.2013.08.059

Doolittle, L.K., Rosen, M.K., Padrick, S.B., 2013a. Measurement and analysis of in vitro actin polymerization. Methods in Molecular Biology 1046, 273–293. https://doi.org/10.1007/978-1-62703-538-5_16

Doolittle, L.K., Rosen, M.K., Padrick, S.B., 2013b. Purification of native Arp2/3 complex from bovine thymus. Methods Mol Biol 1046, 231–250. https://doi.org/10.1007/978-1-62703-538-5_14

Drozdetskiy, A., Cole, C., Procter, J., Barton, G.J., 2015. JPred4: a protein secondary structure prediction server. Nucleic Acids Res 43, W389–W394. https://doi.org/10.1093/nar/gkv332

Dyson, H.J., Wright, P.E., 2002. Coupling of folding and binding for unstructured proteins. Curr Opin Struct Biol 12, 54–60. https://doi.org/10.1016/S0959-440X(02)00289-0

Eden, Sharon., Rohatgi, Rajat., Podtelejnikov, A. V., Mann, M., Kirschner, M.W., 2002. Mechanism of regulation of WAVE1-induced actin nucleation by Rac1 and Nck. Nature 418, 790–793. https://doi.org/10.1038/nature00859

Essmann, U., Perera, L., Berkowitz, M.L., Darden, T., Lee, H., Pedersen, L.G., 1995. A smooth particle mesh Ewald method. J Chem Phys 103, 8577–8593. https://doi.org/10.1063/1.470117

Evans, R., O'Neill, M., Pritzel, A., Antropova, N., Senior, A., Green, T., Žídek, A., Bates, R., Blackwell, S., Yim, J., Ronneberger, O., Bodenstein, S., Zielinski, M., Bridgland, A., Potapenko, A., Cowie, A., Tunyasuvunakool, K., Jain, R., Clancy, E., Kohli, P., Jumper, J., Hassabis, D., 2022. Protein complex prediction with AlphaFold-Multimer. bioRxiv 2021.10.04.463034. https://doi.org/10.1101/2021.10.04.463034

Fan, L., Lu, Y., Shen, X., Shao, H., Suo, L., Wu, Q., 2018. Alpha protocadherins and Pyk2 kinase regulate cortical neuron migration and cytoskeletal dynamics via rac1 GTPase and WAVE complex in mice. Elife 7, 1–26. https://doi.org/10.7554/eLife.35242

Funk, J., Merino, F., Schaks, M., Rottner, K., Raunser, S., Bieling, P., 2021. A barbed end interference mechanism reveals how capping protein promotes nucleation in branched actin networks. Nat Commun 12. https://doi.org/10.1038/s41467-021-25682-5

Gautreau, A., Ho, H. -y. H., Li, J., Steen, H., Gygi, S.P., Kirschner, M.W., 2004. Purification and architecture of the ubiquitous Wave complex. Proceedings of the National Academy of Sciences 101, 4379–4383. https://doi.org/10.1073/pnas.0400628101

Goley, E.D., Welch, M.D., 2006. The ARP2/3 complex: An actin nucleator comes of age. Nat Rev Mol Cell Biol 7, 713–726. https://doi.org/10.1038/nrm2026

Greenfield, N.J., 2006. Using circular dichroism spectra to estimate protein secondary structure. Nat Protoc 1, 2876–2890. https://doi.org/10.1038/nprot.2006.202

Hansen, S.D., Zuchero, J.B., Mullins, R.D., 2013. Cytoplasmic Actin: Purification and Single Molecule Assembly Assays BT - Adhesion Protein Protocols, in: Coutts, A.S. (Ed.), . Humana Press, Totowa, NJ, pp. 145–170. https://doi.org/10.1007/978-1-62703-538-5_9

Hasegawa, K., Matsui, T.K., Kondo, J., Kuwako, K.I., 2022. N-WASP-Arp2/3 signaling controls multiple steps of dendrite maturation in Purkinje cells in vivo. Development 149. https://doi.org/10.1242/dev.201214

Heier, J.A., Dickinson, D.J., Kwiatkowski, A. V, 2017. Measuring Protein Binding to F-actin by Co-sedimentation. J Vis Exp 55613. https://doi.org/10.3791/55613

Heiss, S.G., Cooper, J.A., 1991. Regulation of CapZ, an Actin Capping Protein of Chicken Muscle, by Anionic Phospholipids. Biochemistry 30, 8753–8758. https://doi.org/10.1021/bi00100a006

Hess, B., Bekker, H., Berendsen, H.J.C., Fraaije, J.G.E.M., 1997. LINCS: A Linear Constraint Solver for molecular simulations. J Comput Chem 18, 1463–1472. https://doi.org/10.1002/(SICI)1096-987X(199709)18:12<1463::AID-JCC4>3.0.CO;2-H

Hotulainen, P., Hoogenraad, C.C., 2010. Actin in dendritic spines: Connecting dynamics to function. Journal of Cell Biology 189, 619–629. https://doi.org/10.1083/jcb.201003008

Huang, Z., Liu, H., Nix, J., Xu, R., Knoverek, C.R., Bowman, G.R., Amarasinghe, G.K., Sibley, L.D., 2022. The intrinsically disordered protein TgIST from Toxoplasma gondii inhibits STAT1 signaling by blocking cofactor recruitment. Nat Commun 13. https://doi.org/10.1038/s41467-022-31720-7

Huber, A.H., Stewart, D.B., Laurents, D. V, Nelson, W.J., Weis, W.I., 2001. The cadherin cytoplasmic domain is unstructured in the absence of beta-catenin. A possible mechanism for regulating cadherin turnover. J Biol Chem 276, 12301–12309. https://doi.org/10.1074/jbc.M010377200

Huber, A.H., Weis, W.I., 2001. The structure of the beta-catenin/E-cadherin complex and the molecular basis of diverse ligand recognition by beta-catenin. Cell 105, 391–402. https://doi.org/10.1016/s0092-8674(01)00330-0

Huxley, H.E., Brown, W., 1967. The low-angle X-ray diagram of vertebrate striated muscle and its behaviour during contraction and rigor. J Mol Biol 30, 383–434. https://doi.org/10.1016/S0022-2836(67)80046-9

Hwang, D.S., Waite, J.H., 2012. Three intrinsically unstructured mussel adhesive proteins, mfp-1, mfp-2, and mfp-3: Analysis by circular dichroism. Protein Science 21, 1689–1695. https://doi.org/10.1002/pro.2147

Ito, Y., Carss, K.J., Duarte, S.T., Hartley, T., Keren, B., Kurian, M.A., Marey, I., Charles, P., Mendonça, C., Nava, C., Pfundt, R., Sanchis-Juan, A., van Bokhoven, H., van Essen, A., van Ravenswaaij-Arts, C., Aitman, T., Bennett, D., Caulfield, M., Chinnery, P., Gale, D., Koziell, A., Kuijpers, T.W., Laffan, M.A., Maher, E., Markus, H.S., Morrell, N.W., Ouwehand, W.H., Perry, D.J., Raymond, F.L., Roberts, I., Smith, K.G.C., Thrasher, A., Watkins, H., Williamson, C., Woods, G., Ashford, S., Bradley, J.R., Fletcher, D., Hammerton, T., James, R., Kingston, N., Penkett, C.J., Stirrups, K., Veltman, M., Young, T., Brown, M., Clements-Brod, N., Davis, J., Dewhurst, E., Dolling, H., Erwood, M., Frary, A., Linger, R., Martin, J.M., Papadia, S., Rehnstrom, K., Stark, H., Allsup, D., Austin, S., Bakchoul, T., Bariana, T.K., Bolton-Maggs, P., Chalmers, E., Collins, J., Collins, P., Erber, W.N., Everington, T., Favier, R., Freson, K., Furie, B., Gattens, M., Gebhart, J., Gomez, K., Greene, D., Greinacher, A., Gresele, P., Hart, D., Heemskerk, J.W.M., Henskens, Y., Kazmi, R., Keeling, D., Kelly, A.M., Lambert, M.P., Lentaigne, C., Liesner, R., Makris, M., Mangles, S., Mathias, M., Millar, C.M., Mumford, A., Nurden, P., Payne, J., Pasi, J., Peerlinck, K., Revel-Vilk, S., Richards, M., Rondina, M., Roughley, C., Schulman, S., Schulze, H., Scully, M., Sivapalaratnam, S., Stubbs, M., Tait, R.C., Talks, K., Thachil, J., Toh, C.H., Turro, E., Van Geet, C., De Vries, M., Warner, T.Q., Watson, H., Westbury, S., Furnell, A., Mapeta, R., Rayner-Matthews, P., Simeoni, I., Staines, S., Stephens, J., Watt, C., Whitehorn, D., Attwood, A., Daugherty, L., Deevi, S.V.V., Halmagyi, C., Hu, F., Matser, V., Meacham, S., Megy, K., Shamardina, O., Titterton, C., Tuna, S., Yu, P., von Ziegenweldt, J., Astle, W., Bleda, M., Carss, K.J., Gräf, S., Haimel, M., Lango-Allen, H., Richardson, S., Calleja, P., Rankin, S., Turek, W., Anderson, J., Bryson, C., Carmichael, J., McJannet, C., Stock, S., Allen, L., Ambegaonkar, G., Armstrong, R., Arno, G., Bitner-Glindzicz, M., Brady, A., Canham, N., Chitre, M., Clement, E., Clowes, V., Deegan, P., Deshpande, C., Doffinger, R., Firth, H., Flinter, F., French, C., Gardham, A., Ghali, N., Gissen, P., Grozeva, D., Henderson, R., Hensiek, A., Holden, S., Holder, M., Holder, S., Hurst, J., Josifova, D., Krishnakumar, D., Kurian, M.A., Lees, M., MacLaren, R., Maw, A., Mehta, S., Michaelides, M., Moore, A., Murphy, E., Park, S.M., Parker, A., Patch, C., Paterson, J., Rankin, J., Reid, E., Rosser, E., Sanchis-Juan, A., Sandford, R., Santra, S., Scott, R., Sohal, A., Stein, P., Thomas, E., Thompson, D., Tischkowitz, M., Vogt, J., Wakeling, E., Wassmer, E., Webster, A., Ali, Sonia, Ali, Souad, Boggard, H.J., Church, C., Coghlan, G., Cookson, V., Corris, P.A., Creaser-Myers, A., DaCosta, R., Dormand, N., Eyries, M., Gall, H., Ghataorhe, P.K., Ghio, S., Ghofrani, A., Gibbs, J.S.R., Girerd, B., Greenhalgh, A., Hadinnapola, C., Houweling, A.C., Humbert, M., in't Veld, A.H., Kennedy, F., Kiely, D.G., Kovacs, G., Lawrie, A., Ross, R.V.M., Machado, R., Masati, L., Meehan, S., Moledina, S., Montani, D., Othman, S., Peacock, A.J., Pepke-Zaba, J., Pollock, V., Polwarth, G., Ranganathan, L., Rhodes, C.J., Rue-Albrecht, K., Schotte, G., Shipley, D., Soubrier, F., Southgate, L., Scelsi, L., Suntharalingam, J., Tan, Y., Toshner, M., Treacy, C.M., Trembath, R., Noordegraaf, A.V., Walker, Sara, Wanjiku, I., Wharton, J., Wilkins, M., Wort, S.J., Yates, K., Alachkar, H., Antrobus, R.,

Arumugakani, G., Bacchelli, C., Baxendale, H., Bethune, C., Bibi, S., Booth, C., Browning, M., Burns, S., Chandra, A., Cooper, N., Davies, S., Devlin, L., Drewe, E., Edgar, D., Egner, W., Ghurye, R., Gilmour, K., Goddard, S., Gordins, P., Grigoriadou, S., Hackett, S., Hague, R., Harper, L., Hayman, G., Herwadkar, A., Huissoon, A., Jolles, S., Kelleher, P., Kumararatne, D., Lear, S., Longhurst, H., Lorenzo, L., Maimaris, J., Manson, A., McDermott, E., Murng, S., Nejentsev, S., Noorani, S., Oksenhendler, E., Ponsford, M., Qasim, W., Quinti, I., Richter, A., Samarghitean, C., Sargur, R., Savic, S., Seneviratne, S., Sewell, C., Staples, E., Stauss, H., Thaventhiran, J., Thomas, M., Welch, S., Willcocks, L., Yeatman, N., Yong, P., Ancliff, P., Babbs, C., Layton, M., Louka, E., McGowan, S., Mead, A., Roy, N., Chambers, J., Dixon, P., Estiu, C., Hague, B., Marschall, H.U., Simpson, M., Chong, S., Emmerson, I., Ginsberg, L., Gosal, D., Hadden, R., Horvath, R., Mahdi-Rogers, M., Manzur, A., Marshall, A., Matthews, E., McCarthy, M., Reilly, M., Renton, T., Rice, A., Themistocleous, A., Vale, T., Van Zuydam, N., Walker, Suellen, Ormondroyd, L., Hudson, G., Wei, W., Yu Wai Man, P., Whitworth, J., Afzal, M., Colby, E., Saleem, M., Alavijeh, O.S., Cook, H.T., Johnson, S., Levine, A.P., Wong, E.K.S., Tan, R., Boycott, K.M., MacKenzie, A., Majewski, J., Brudno, M., Bulman, D., Dyment, D., Boycott, K.M., Kernohan, K.D., Dyack, S., Raymond, F.L., 2018. De Novo Truncating Mutations in WASF1 Cause Intellectual Disability with Seizures. Am J Hum Genet 103, 144–153. https://doi.org/10.1016/j.ajhg.2018.06.001

Jan, Y.-N., Jan, L.Y., 2003. The Control of Dendrite Development. Neuron 40, 229–242. https://doi.org/https://doi.org/10.1016/S0896-6273(03)00631-7

Johannes, L., Pezeshkian, W., Ipsen, J.H., Shillcock, J.C., 2018. Clustering on Membranes: Fluctuations and More. Trends Cell Biol 28, 405–415. https://doi.org/10.1016/j.tcb.2018.01.009

Jumper, J., Evans, R., Pritzel, A., Green, T., Figurnov, M., Ronneberger, O., Tunyasuvunakool, K., Bates, R., Žídek, A., Potapenko, A., Bridgland, A., Meyer, C., Kohl, S.A.A., Ballard, A.J., Cowie, A., Romera-Paredes, B., Nikolov, S., Jain, R., Adler, J., Back, T., Petersen, S., Reiman, D., Clancy, E., Zielinski, M., Steinegger, M., Pacholska, M., Berghammer, T., Bodenstein, S., Silver, D., Vinyals, O., Senior, A.W., Kavukcuoglu, K., Kohli, P., Hassabis, D., 2021. Highly accurate protein structure prediction with AlphaFold. Nature 596, 583–589. https://doi.org/10.1038/s41586-021-03819-2

Källberg, M., Wang, H., Wang, S., Peng, J., Wang, Z., Lu, H., Xu, J., 2012. Template-based protein structure modeling using the RaptorX web server. Nat Protoc 7, 1511–1522. https://doi.org/10.1038/nprot.2012.085

Kirkpatrick, S.L., Goldberg, L.R., Yazdani, N., Babbs, R.K., Wu, J., Reed, E.R., Jenkins, D.F., Bolgioni, A.F., Landaverde, K.I., Luttik, K.P., Mitchell, K.S., Kumar, V., Johnson, W.E., Mulligan, M.K., Cottone, P., Bryant, C.D., 2017. Cytoplasmic FMR1-Interacting Protein 2 Is a Major Genetic Factor Underlying Binge Eating. Biol Psychiatry 81, 757–769. https://doi.org/10.1016/j.biopsych.2016.10.021

Kjaergaard, M., Brander, S., Poulsen, F.M., 2011. Random coil chemical shift for intrinsically disordered proteins: Effects of temperature and pH. J Biomol NMR 49, 139–149. https://doi.org/10.1007/s10858-011-9472-x

Kjaergaard, M., Poulsen, F.M., 2011. Sequence correction of random coil chemical shifts: Correlation between neighbor correction factors and changes in the Ramachandran distribution. J Biomol NMR 50, 157–165. https://doi.org/10.1007/s10858-011-9508-2

Kobayashi, K., Kuroda, S., Fukata, M., Nakamura, T., Nagase, T., Nomura, N., Matsuura, Y., Yoshida-Kubomura, N., Iwamatsu, A., Kaibuchi, K., 1998. p140Sra-1 (specifically Rac1-associated protein) is a novel specific target for Rac1 small GTPase. Journal of Biological Chemistry 273, 291–295. https://doi.org/10.1074/jbc.273.1.291

Koronakis, V., Hume, P.J., Humphreys, D., Liu, T., Horning, O., Jensen, O.N., McGhie, E.J., 2011. WAVE regulatory complex activation by cooperating GTPases Arf and Rac1. Proceedings of the National Academy of Sciences 108, 14449–14454. https://doi.org/10.1073/pnas.1107666108

Kouyama, T., Mihashi, K., 1981. Fluorimetry study of N-(1-pyrenyl)iodoacetamide-labelled F-actin. Local structural change of actin protomer both on polymerization and on binding of heavy meromyosin. Eur J Biochem 114, 33–38.

1616 Kramer, D.A., Piper, H.K., Chen, B., 2022. WASP family proteins : Molecular mechanisms and
1617 implications in human disease. Eur J Cell Biol 101. https://doi.org/10.1016/j.ejcb.2022.151244
1618 Kuhn, J.R., Pollard, T.D., 2005. Real-time measurements of actin filament polymerization by total
1619 internal reflection fluorescence microscopy. Biophys J 88, 1387–1402.
1620 https://doi.org/10.1529/biophysj.104.047399
1621 Kumar, V., Kim, K., Joseph, C., Kourrich, S., Yoo, S.-H., Huang, H.C., Vitaterna, M.H., de Villena, F.P.-
1622 M., Churchill, G., Bonci, A., Takahashi, J.S., 2013. C57BL/6N Mutation in Cytoplasmic FMRP
1623 interacting protein 2 Regulates Cocaine Response. Science (1979) 342, 1508–1512.
1624 Kuzmic, P., 1996. Program DYNAFIT for the analysis of enzyme kinetic data: application to
1625 HIV proteinase. Anal Biochem 237, 260–273. https://doi.org/10.1006/abio.1996.0238
1626 Lebensohn, A.M., Kirschner, M.W., 2009. Activation of the WAVE Complex by Coincident Signals
1627 Controls Actin Assembly. Mol Cell 36, 512–524. https://doi.org/10.1016/j.molcel.2009.10.024
1628 Lee, N.K., Fok, K.W., White, A., Wilson, N.H., O'Leary, C.J., Cox, H.L., Michael, M., Yap, A.S.,
1629 Cooper, H.M., 2016. Neogenin recruitment of the WAVE regulatory complex maintains adherens
1630 junction stability and tension. Nat Commun 7. https://doi.org/10.1038/ncomms11082
1631 Lee, W., Tonelli, M., Markley, J.L., 2015. NMRFAM-SPARKY: Enhanced software for biomolecular
1632 NMR spectroscopy. Bioinformatics 31, 1325–1327. https://doi.org/10.1093/bioinformatics/btu830
1633 Lefebvre, J.L., Sanes, J.R., Kay, J.N., 2015. Development of Dendritic Form and Function. Annu Rev
1634 Cell Dev Biol 31, 741–777. https://doi.org/10.1146/annurev-cellbio-100913-013020
1635 Machesky, L.M., Atkinson, S.J., Ampe, C., Vandekerckhove, J., Pollard, T.D., Vandekercldaove, J.,
1636 1994. Purification of a cortical complex containing two unconventional actins from Acanthamoeba
1637 by affinity chromatography on profilin-agarose. Journal of Cell Biology 127, 107–115.
1638 https://doi.org/10.1083/jcb.127.1.107
1639 Machesky, L.M., Insall, R.H., 1998. Scar1 and the related Wiskott-Aldrich syndrome protein, WASP,
1640 regulate the actin cytoskeleton through the Arp2/3 complex. Current Biology 8, 1347–1356.
1641 https://doi.org/10.1016/S0960-9822(98)00015-3
1642 McGuffin, L.J., Bryson, K., Jones, D.T., 2000. The PSIPRED protein structure prediction server .
1643 Bioinformatics 16, 404–405. https://doi.org/10.1093/bioinformatics/16.4.404
1644 Minkyung, B., Frank, D., Ivan, A., Justas, D., Sergey, O., Rie, L.G., Jue, W., Qian, C., N., K.L., Dustin,
1645 S.R., Claudia, M., Hahnbeom, P., Carson, A., R., G.C., Andy, D., H., P.J., V., R.A., A., van D.A.,
1646 C., E.A., J., O.D., Theo, S., Christoph, B., Tea, P.-K., K., R.M., Udit, D., K., Y.C., E., B.J.,
1647 Christopher, G.K., V., G.N., D., A.P., J., R.R., David, B., 2021. Accurate prediction of protein
1648 structures and interactions using a three-track neural network. Science (1979) 373, 871–876.
1649 https://doi.org/10.1126/science.abj8754
1650 Miyoshi, T., Tsuji, T., Higashida, C., Hertzog, M., Fujita, A., Narumiya, S., Scita, G., Watanabe, N.,
1651 2006. Actin turnover-dependent fast dissociation of capping protein in the dendritic nucleation actin
1652 network: Evidence of frequent filament severing. Journal of Cell Biology 175, 947–955.
1653 https://doi.org/10.1083/jcb.200604176
1654 Narvaez-Ortiz, H.Y., Nolen, B.J., 2022. Unconcerted conformational changes in Arp2/3 complex
1655 integrate multiple activating signals to assemble functional actin networks. Current Biology 32, 975-
1656 987.e6. https://doi.org/10.1016/j.cub.2022.01.004
1657 Okuda, M., Tsunaka, Y., Nishimura, Y., 2022. Dynamic structures of intrinsically disordered proteins
1658 related to the general transcription factor TFIIH, nucleosomes, and histone chaperones. Biophys
1659 Rev. https://doi.org/10.1007/s12551-022-01014-9
1660 Olive, C., Ibanez, L., Farias, F.H.G., Wang, F., John, P., Norton, J.B., Gentsch, J., Morris, J.C., Li, Z.,
1661 Del-aguila, J., Bergmann, K., Bradley, J., Benitez, B.A., Harari, O., Fagan, A., Ances, B., Cruchaga,
1662 C., Victoria, M., 2020. Examination of the Effect of Rare Variants in TREM2, ABI3, and PLCG2 in
1663 LOAD Through Multiple Phenotypes. Journal of Alzheimers Disease 77, 1469–1482.
1664 https://doi.org/10.3233/JAD-200019.Examination
1665 O'Shea, E.K., Klemm, J.D., Kim, P.S., Alber, T., 1999. X-ray Structure of the GCN4 Leucine Zipper, a
1666 Two-Stranded, Parallel Coiled Coil. Science (1979) 254, 539–544.

1667 Padrick, S.B., Cheng, H.C., Ismail, A.M., Panchal, S.C., Doolittle, L.K., Kim, S., Skehan, B.M., Umetani,
1668 J., Brautigam, C.A., Leong, J.M., Rosen, M.K., 2008. Hierarchical Regulation of WASP/WAVE
1669 Proteins. Mol Cell 32, 426–438. https://doi.org/10.1016/j.molcel.2008.10.012
1670 Pilpel, Y., Segal, M., 2005. Rapid WAVE dynamics in dendritic spines of cultured hippocampal neurons
1671 is mediated by actin polymerization. J Neurochem 95, 1401–1410. https://doi.org/10.1111/j.1471-
1672 4159.2005.03467.x
1673 Polesskaya, A., Boutillon, A., Yang, S., Wang, Y., Romero, S., Liu, Y., Lavielle, M., Vacher, S.,
1674 Schnitzler, A., Molinie, N., Rocques, N., Fokin, A., Guérois, R., Bièche, I., Chen, B., David, N.B.,
1675 Gautreau, A.M., 2021. CYFIP2-containing WAVE complexes inhibit cell migration by a
1676 competition mechanism. bioRxiv 2020.07.02.184655.
1677 Pollard, T.D., 2010. A Guide to Simple and Informative Binding Assays. Mol Biol Cell 21, 4061–4067.
1678 https://doi.org/10.1091/mbc.e10-08-0683
1679 Pollard, T.D., 2007. Regulation of Actin Filament Assembly by Arp2/3 Complex and Formins. Annu Rev
1680 Biophys Biomol Struct 36, 451–477. https://doi.org/10.1146/annurev.biophys.35.040405.101936
1681 Pollitt, A.Y., Insall, R.H., 2009. WASP and SCAR/WAVE proteins: the drivers of actin assembly. J Cell
1682 Sci 122, 2575–2578. https://doi.org/10.1242/jcs.023879
1683 Racz, B., Weinberg, R.J., 2008. Organization of the Arp2/3 Complex in Hippocampal Spines. Journal of
1684 Neuroscience 28, 5654–5659. https://doi.org/10.1523/jneurosci.0756-08.2008
1685 Robustelli, P., Piana, S., Shaw, D.E., 2018. Developing a molecular dynamics force field for both folded
1686 and disordered protein states. Proc Natl Acad Sci U S A 115, E4758–E4766.
1687 https://doi.org/10.1073/pnas.1800690115
1688 Rottner, K., Stradal, T.E.B., Chen, B., 2021. WAVE regulatory complex. Current Biology 31, R512–
1689 R517. https://doi.org/10.1016/j.cub.2021.01.086
1690 Scott, E.K., Luo, L., 2001. How do dendrites take their shape? Nat Neurosci 4, 359–365.
1691 https://doi.org/10.1038/86006
1692 Shi, R., Kramer, D.A., Chen, B., Shen, K., 2021. A two-step actin polymerization mechanism drives
1693 dendrite branching. Neural Dev 16, 1–16. https://doi.org/10.1186/s13064-021-00154-0
1694 Shimojima Yamamoto, K., Yanagishita, T., Yamamoto, H., Miyamoto, Y., Nagata, M., Ishihara, Y.,
1695 Miyashita, Y., Asano, Y., Sakata, Y., Yamamoto, T., 2021. Recurrent de novo pathogenic variant of
1696 WASF1 in a Japanese patient with neurodevelopmental disorder with absent language and variable
1697 seizures. Hum Genome Var 8, 7–9. https://doi.org/10.1038/s41439-021-00176-4
1698 Sims, R., Van Der Lee, S.J., Naj, A.C., Bellenguez, C., Badarinarayan, N., Jakobsdottir, J., Kunkle, B.W.,
1699 Boland, A., Raybould, R., Bis, J.C., Martin, E.R., Grenier-Boley, B., Heilmann-Heimbach, S.,
1700 Chouraki, V., Kuzma, A.B., Sleegers, K., Vronskaya, M., Ruiz, A., Graham, R.R., Olaso, R.,
1701 Hoffmann, P., Grove, M.L., Vardarajan, B.N., Hiltunen, M., Nöthen, M.M., White, C.C., Hamilton-
1702 Nelson, K.L., Epelbaum, J., Maier, W., Choi, S.H., Beecham, G.W., Dulary, C., Herms, S., Smith,
1703 A.G.A. V., Funk, C.C., Derbois, C., Forstner, A.J., Ahmad, S., Li, H., Bacq, D., Harold, D.,
1704 Satizabal, C.L., Valladares, O., Squassina, A., Thomas, R., Brody, J.A., Qu, L., Sánchez-Juan, P.,
1705 Morgan, T., Wolters, F.J., Zhao, Y., Garcia, F.S., Denning, N., Fornage, M., Malamon, J., Naranjo,
1706 M.C.D., Majounie, E., Mosley, T.H., Dombroski, B., Wallon, D., Lupton, M.K., Dupuis, J.,
1707 Whitehead, P., Fratiglioni, L., Medway, C., Jian, X., Mukherjee, S., Keller, L., Brown, K., Lin, H.,
1708 Cantwell, L.B., Panza, F., McGuinness, B., Moreno-Grau, S., Burgess, J.D., Solfrizzi, V., Proitsi, P.,
1709 Adams, H.H., Allen, M., Seripa, D., Pastor, P., Cupples, L.A., Price, N.D., Hannequin, D., Frank-
1710 García, A., Levy, D., Chakrabarty, P., Caffarra, P., Giegling, I., Beiser, A.S., Giedraitis, V., Hampel,
1711 H., Garcia, M.E., Wang, X., Lannfelt, L., Mecocci, P., Eiriksdottir, G., Crane, P.K., Pasquier, F.,
1712 Boccardi, V., Henández, I., Barber, R.C., Scherer, M., Tarraga, L., Adams, P.M., Leber, M., Chen,
1713 Y., Albert, M.S., Riedel-Heller, S., Emilsson, V., Beekly, D., Braae, A., Schmidt, R., Blacker, D.,
1714 Masullo, C., Schmidt, H., Doody, R.S., Spalletta, G., Jr, W.T.L., Fairchild, T.J., Bossù, P., Lopez,
1715 O.L., Frosch, M.P., Sacchinelli, E., Ghetti, B., Yang, Q., Huebinger, R.M., Jessen, F., Li, S.,
1716 Kamboh, M.I., Morris, J.C., Sotolongo-Grau, O., Katz, M.J., Corcoran, C., Dunstan, M., Braddel,
1717 A., Thomas, C., Meggy, A., Marshall, R., Gerrish, A., Chapman, J., Aguilar, M., Taylor, S., Hill,

M., Fairén, M.D., Hodges, A., Vellas, B., Soininen, H., Kloszewska, I., Daniilidou, M., Uphill, J., Patel, Y., Hughes, J.T., Lord, J., Turton, J., Hartmann, A.M., Cecchetti, R., Fenoglio, C., Serpente, M., Arcaro, M., Caltagirone, C., Orfei, M.D., Ciaramella, A., Pichler, S., Mayhaus, M., Gu, W., Lleó, A., Fortea, J., Blesa, R., Barber, I.S., Brookes, K., Cupidi, C., Maletta, R.G., Carrell, D., Sorbi, S., Moebus, S., Urbano, M., Pilotto, A., Kornhuber, J., Bosco, P., Todd, S., Craig, D., Johnston, J., Gill, M., Lawlor, B., Lynch, A., Fox, N.C., Hardy, J., Albin, R.L., Apostolova, L.G., Arnold, S.E., Asthana, S., Atwood, C.S., Baldwin, C.T., Barnes, L.L., Barral, S., Beach, T.G., Becker, J.T., Bigio, E.H., Bird, T.D., Boeve, B.F., Bowen, J.D., Boxer, A., Burke, J.R., Burns, J.M., Buxbaum, J.D., Cairns, N.J., Cao, C., Carlson, C.S., Carlsson, C.M., Carney, R.M., Carrasquillo, M.M., Carroll, S.L., Diaz, C.C., Chui, H.C., Clark, D.G., Cribbs, D.H., Crocco, E.A., Decarli, C., Dick, M., Duara, R., Evans, D.A., Faber, K.M., Fallon, K.B., Fardo, D.W., Farlow, M.R., Ferris, S., Foroud, T.M., Galasko, D.R., Gearing, M., Geschwind, D.H., Gilbert, J.R., Graff-Radford, N.R., Green, R.C., Growdon, J.H., Hamilton, R.L., Harrell, L.E., Honig, L.S., Huentelman, M.J., Hulette, C.M., Hyman, B.T., Jarvik, G.P., Abner, E., Jin, L.W., Jun, G., Karydas, A., Kaye, J.A., Kim, R., Kowall, N.W., Kramer, J.H., Laferla, F.M., Lah, J.J., Leverenz, J.B., Levey, A.I., Li, G., Lieberman, A.P., Lunetta, K.L., Lyketsos, C.G., Marson, D.C., Martiniuk, F., Mash, D.C., Masliah, E., McCormick, W.C., McCurry, S.M., McDavid, A.N., McKee, A.C., Mesulam, M., Miller, B.L., Miller, C.A., Miller, J.W., Murrell, J.R., Myers, A.J., O'Bryant, S., Olichney, J.M., Pankratz, V.S., Parisi, J.E., Paulson, H.L., Perry, W., Peskind, E., Pierce, A., Poon, W.W., Potter, H., Quinn, J.F., Raj, A., Raskind, M., Reisberg, B., Reitz, C., Ringman, J.M., Roberson, E.D., Rogaeva, E., Rosen, H.J., Rosenberg, R.N., Sager, M.A., Saykin, A.J., Schneider, J.A., Schneider, L.S., Seeley, W.W., Smith, A.G.A. V., Sonnen, J.A., Spina, S., Stern, R.A., Swerdlow, R.H., Tanzi, R.E., Thornton-Wells, T.A., Trojanowski, J.Q., Troncoso, J.C., Van Deerlin, V.M., Van Eldik, L.J., Vinters, H. V., Vonsattel, J.P., Weintraub, S., Welsh-Bohmer, K.A., Wilhelmsen, K.C., Williamson, J., Wingo, T.S., Woltjer, R.L., Wright, C.B., Yu, C.E., Yu, L., Garzia, F., Golamaully, F., Septier, G., Engelborghs, S., Vandenberghe, R., De Deyn, P.P., Fernadez, C.M., Benito, Y.A., Thonberg, H., Forsell, C., Lilius, L., Kinhult-Stählbom, A., Kilander, L., Brundin, R., Concari, L., Helisalmi, S., Koivisto, A.M., Haapasalo, A., Dermecourt, V., Fievet, N., Hanon, O., Dufouil, C., Brice, A., Ritchie, K., Dubois, B., Himali, J.J., Keene, C.D., Tschanz, J., Fitzpatrick, A.L., Kukull, W.A., Norton, M., Aspelund, T., Larson, E.B., Munger, R., Rotter, J.I., Lipton, R.B., Bullido, M.J., Hofman, A., Montine, T.J., Coto, E., Boerwinkle, E., Petersen, R.C., Alvarez, V., Rivadeneira, F., Reiman, E.M., Gallo, M., O'Donnell, C.J., Reisch, J.S., Bruni, A.C., Royall, D.R., Dichgans, M., Sano, M., Galimberti, D., St George-Hyslop, P., Scarpini, E., Tsuang, D.W., Mancuso, M., Bonuccelli, U., Winslow, A.R., Daniele, A., Wu, C.K., Peters, O., Nacmias, B., Riemenschneider, M., Heun, R., Brayne, C., Rubinsztein, D.C., Bras, J., Guerreiro, R., Al-Chalabi, A., Shaw, C.E., Collinge, J., Tsolaki, M., Clarimón, J., Sussams, R., Lovestone, S., O'Donovan, M.C., Owen, M.J., Behrens, T.W., Mead, S., Uitterlinden, A.G., Holmes, C., Cruchaga, C., Ingelsson, M., Bennett, D.A., Powell, J., Golde, T.E., Graff, C., De Jager, P.L., Morgan, K., Ertekin-Taner, N., Combarros, O., Psaty, B.M., Passmore, P., Younkin, S.G., Berr, C., Gudnason, V., Rujescu, D., Dickson, D.W., Dartigues, J.F., Destefano, A.L., Ortega-Cubero, S., Hakonarson, H., Campion, D., Boada, M., Kauwe, J.K., Farrer, L.A., Van Broeckhoven, C., Ikram, M.A., Jones, L., Haines, J.L., Tzourio, C., Tzourio, C., Escott-Price, V., Mayeux, R., Deleuze, J.F., Amin, N., Goate, A.M., Pericak-Vance, M.A., Amouyel, P., Van Duijn, C.M., Ramirez, A., Wang, L.S., Lambert, J.C., Seshadri, S., Williams, J., Schellenberg, G.D., 2017. Rare coding variants in PLCG2, ABI3, and TREM2 implicate microglial-mediated innate immunity in Alzheimer's disease. Nat Genet 49, 1373–1384. https://doi.org/10.1038/ng.3916

Smith, C.J., O'Brien, T., Chatzigeorgiou, M., Clay Spencer, W., Feingold-Link, E., Husson, S.J., Hori, S., Mitani, S., Gottschalk, A., Schafer, W.R., Miller, D.M., 2013. Sensory neuron fates are distinguished by a transcriptional switch that regulates dendrite branch stabilization. Neuron 79, 266–280. https://doi.org/10.1016/j.neuron.2013.05.009

Soderling, S.H., Guire, E.S., Kaech, S., White, J., Zhang, F., Schutz, K., Langeberg, L.K., Banker, G., Raber, J., Scott, J.D., 2007. A WAVE-1 and WRP Signaling Complex Regulates Spine Density,

Synaptic Plasticity, and Memory. Journal of Neuroscience 27, 355–365. https://doi.org/10.1523/jneurosci.3209-06.2006

Soderling, S.H., Langeberg, L.K., Soderling, J.A., Davee, S.M., Simerly, R., Raber, J., Scott, J.D., H., S.S., K., L.L., A., S.J., M., D.S., Richard, S., Jacob, R., D., S.J., 2003. Loss of WAVE-1 causes sensorimotor retardation and reduced learning and memory in mice. Proceedings of the National Academy of Sciences 100, 1723–1728. https://doi.org/10.1073/pnas.0438033100

Spudich, J.A., Watt, S., 1971. The Regulation of Rabbit Skeletal Muscle Contraction. Journal of Biological Chemistry 246, 4866–4871. https://doi.org/10.1016/s0021-9258(18)62016-2

Srivastava, S., Macke, E.L., Swanson, L.C., Coulter, D., Klee, E.W., Mullegama, S. V., Xie, Y., Lanpher, B.C., Bedoukian, E.C., Skraban, C.M., Villard, L., Milh, M., Leppert, M.L.O., Cohen, J.S., 2021. Expansion of the genotypic and phenotypic spectrum of wasf1-related neurodevelopmental disorder. Brain Sci 11, 1–10. https://doi.org/10.3390/brainsci11070931

Stephan, R., Gohl, C., Fleige, A., Klämbt, C., Bogdan, S., 2011. Membrane-targeted WAVE mediates photoreceptor axon targeting in the absence of the WAVE complex in Drosophila. Mol Biol Cell 22, 4079–4092. https://doi.org/10.1091/mbc.E11-02-0121

Tahirovic, S., Hellal, F., Neukirchen, D., Hindges, R., Garvalov, B.K., Flynn, K.C., Stradal, T.E., Chrostek-Grashoff, A., Brakebusch, C., Bradke, F., 2010. Rac1 regulates neuronal polarization through the WAVE complex. J Neurosci 30, 6930–6943. https://doi.org/10.1523/JNEUROSCI.5395-09.2010

Takenawa, T., Suetsugu, S., 2007. The WASP-WAVE protein network: Connecting the membrane to the cytoskeleton. Nat Rev Mol Cell Biol 8, 37–48. https://doi.org/10.1038/nrm2069

Tang, L.T., Diaz-Balzac, C.A., Rahman, M., Ramirez-Suarez, N.J., Salzberg, Y., Lázaro-Peña, M.I., Bülow, H.E., 2019. TIAM-1/GEF can shape somatosensory dendrites independently of its GEF activity by regulating F-actin localization. Elife 8, 1–27. https://doi.org/10.7554/elife.38949

Tavosanis, G., 2012. Dendritic structural plasticity. Dev Neurobiol 72, 73–86. https://doi.org/10.1002/dneu.20951

Turjanski, A.G., Gutkind, J.S., Best, R.B., Hummer, G., 2008. Binding-Induced Folding of a Natively Unstructured Transcription Factor. PLoS Comput Biol 4, e1000060.

Wang, W., Lo, K.W.-H., Kan, H.-M., Fan, J.-S., Zhang, M., 2003. Structure of the monomeric 8-kDa dynein light chain and mechanism of the domain-swapped dimer assembly. J Biol Chem 278, 41491–41499. https://doi.org/10.1074/jbc.M307118200

Wang, X., Jiang, W., Luo, S., Yang, X., Wang, C., Wang, B., Dang, Y., Shen, Y., Ma, D.K., 2021. The C. elegans homolog of human panic-disorder risk gene TMEM132D orchestrates neuronal morphogenesis through the WAVE-regulatory complex. Mol Brain 14, 54. https://doi.org/10.1186/s13041-021-00767-w

Weeds, A., Maciver, S., 1993. F-actin capping proteins. Curr Opin Cell Biol 5, 63–69. https://doi.org/10.1016/S0955-0674(05)80009-2

Weitner, T., Friganović, T., Šakić, D., 2022. Inner Filter Effect Correction for Fluorescence Measurements in Microplates Using Variable Vertical Axis Focus. Anal Chem. https://doi.org/10.1021/acs.analchem.2c01031

Wu, S., Zhang, Y., 2007. LOMETS: a local meta-threading-server for protein structure prediction. Nucleic Acids Res 35, 3375–3382. https://doi.org/10.1093/nar/gkm251

Xing, G., Li, M., Sun, Y., Rui, M., Zhuang, Y., Lv, H., Han, J., Jia, Z., Xie, W., 2018. Neurexin–neuroligin 1 regulates synaptic morphology and functions via the WAVE regulatory complex in Drosophila neuromuscular junction. Elife 7, 1–23. https://doi.org/10.7554/eLife.30457

Yamazaki, D., Fujiwara, T., Suetsugu, S., Takenawa, T., 2005. A novel function of WAVE in lamellipodia: WAVE1 is required for stabilization of lamellipodial protrusions during cell spreading. Genes Cells 10, 381–392. https://doi.org/10.1111/j.1365-2443.2005.00845.x

Yan, Z., Kim, E., Datta, D., Lewis, D.A., Soderling, S.H., 2016. Synaptic Actin Dysregulation, a Convergent Mechanism of Mental Disorders? The Journal of Neuroscience 36, 11411–11417. https://doi.org/10.1523/jneurosci.2360-16.2016

1820 Yang, S., Tang, Y., Liu, Y., Brown, A.J., Schaks, M., Ding, B., Kramer, D.A., Mietkowska, M., Ding, L.,
1821 Alekhina, O., Billadeau, D.D., Chowdhury, S., Wang, J., Rottner, K., Chen, B., 2022. Arf GTPase
1822 activates the WAVE regulatory complex through a distinct binding site. Sci Adv 8.
1823 Yokoyama, K., Tezuka, T., Kotani, M., Nakazawa, T., Hoshina, N., Shimoda, Y., Kakuta, S., Sudo, K.,
1824 Watanabe, K., Iwakura, Y., Yamamoto, T., 2011. NYAP: A phosphoprotein family that links PI3K
1825 to WAVE1 signalling in neurons. EMBO Journal 30, 4739–4754.
1826 https://doi.org/10.1038/emboj.2011.348
1827 Zhao, A., Zhou, R., Gu, Q., Liu, M., Zhang, B., Huang, J., Yang, B., Yao, R., Wang, J., Lv, H., Wang, J.,
1828 Shen, Y., Wang, H., Chen, X., 2021. Trio exome sequencing identified a novel de novo WASF1
1829 missense variant leading to recurrent site substitution in a Chinese patient with developmental delay,
1830 microcephaly, and early-onset seizures: a mutational hotspot p.Trp161 and literature review. Clinica
1831 Chimica Acta. https://doi.org/10.1016/j.cca.2021.08.030
1832 Zhao, B., Meka, D.P., Scharrenberg, R., König, T., Schwanke, B., Kobler, O., Windhorst, S., Kreutz,
1833 M.R., Mikhaylova, M., Calderon de Anda, F., 2017. Microtubules Modulate F-actin Dynamics
1834 during Neuronal Polarization. Sci Rep 7, 9583. https://doi.org/10.1038/s41598-017-09832-8
1835 Zhou, P., Wagner, G., 2010. Overcoming the solubility limit with solubility-enhancement tags: successful
1836 applications in biomolecular NMR studies. J Biomol NMR 46, 23–31.
1837 https://doi.org/10.1007/s10858-009-9371-6
1838 Zou, W., Dong, X., Broederdorf, T.R., Shen, A., Kramer, D.A., Shi, R., Liang, X., Miller, D.M., Xiang,
1839 Y.K., Yasuda, R., Chen, B., Shen, K., 2018. A Dendritic Guidance Receptor Complex Brings
1840 Together Distinct Actin Regulators to Drive Efficient F-Actin Assembly and Branching. Dev Cell
1841 45, 362-375.e3. https://doi.org/10.1016/j.devcel.2018.04.008
1842 Zou, W., Shen, A., Dong, X., Tugizova, M., Xiang, Y.K., Shen, K., 2016. A multi-protein receptor-ligand
1843 complex underlies combinatorial dendrite guidance choices in C. elegans. Elife 5, 1–25.
1844 https://doi.org/10.7554/elife.18345
1845 Zou, W., Yadav, S., DeVault, L., Nung Jan, Y., Sherwood, D.R., 2015. RAB-10-Dependent Membrane
1846 Transport Is Required for Dendrite Arborization. PLoS Genet 11.
1847 https://doi.org/10.1371/journal.pgen.1005484
1848 Zweier, M., Begemann, A., McWalter, K., Cho, M.T., Abela, L., Banka, S., Behring, B., Berger, A.,
1849 Brown, C.W., Carneiro, M., Chen, J., Cooper, G.M., Finnila, C.R., Guillen Sacoto, M.J., Henderson,
1850 A., Hüffmeier, U., Joset, P., Kerr, B., Lesca, G., Leszinski, G.S., McDermott, J.H., Meltzer, M.R.,
1851 Monaghan, K.G., Mostafavi, R., Õunap, K., Plecko, B., Powis, Z., Purcarin, G., Reimand, T.,
1852 Riedhammer, K.M., Schreiber, J.M., Sirsi, D., Wierenga, K.J., Wojcik, M.H., Papuc, S.M., Steindl,
1853 K., Sticht, H., Rauch, A., 2019. Spatially clustering de novo variants in CYFIP2, encoding the
1854 cytoplasmic FMRP interacting protein 2, cause intellectual disability and seizures. European Journal
1855 of Human Genetics 27, 747–759. https://doi.org/10.1038/s41431-018-0331-z
1856
1857

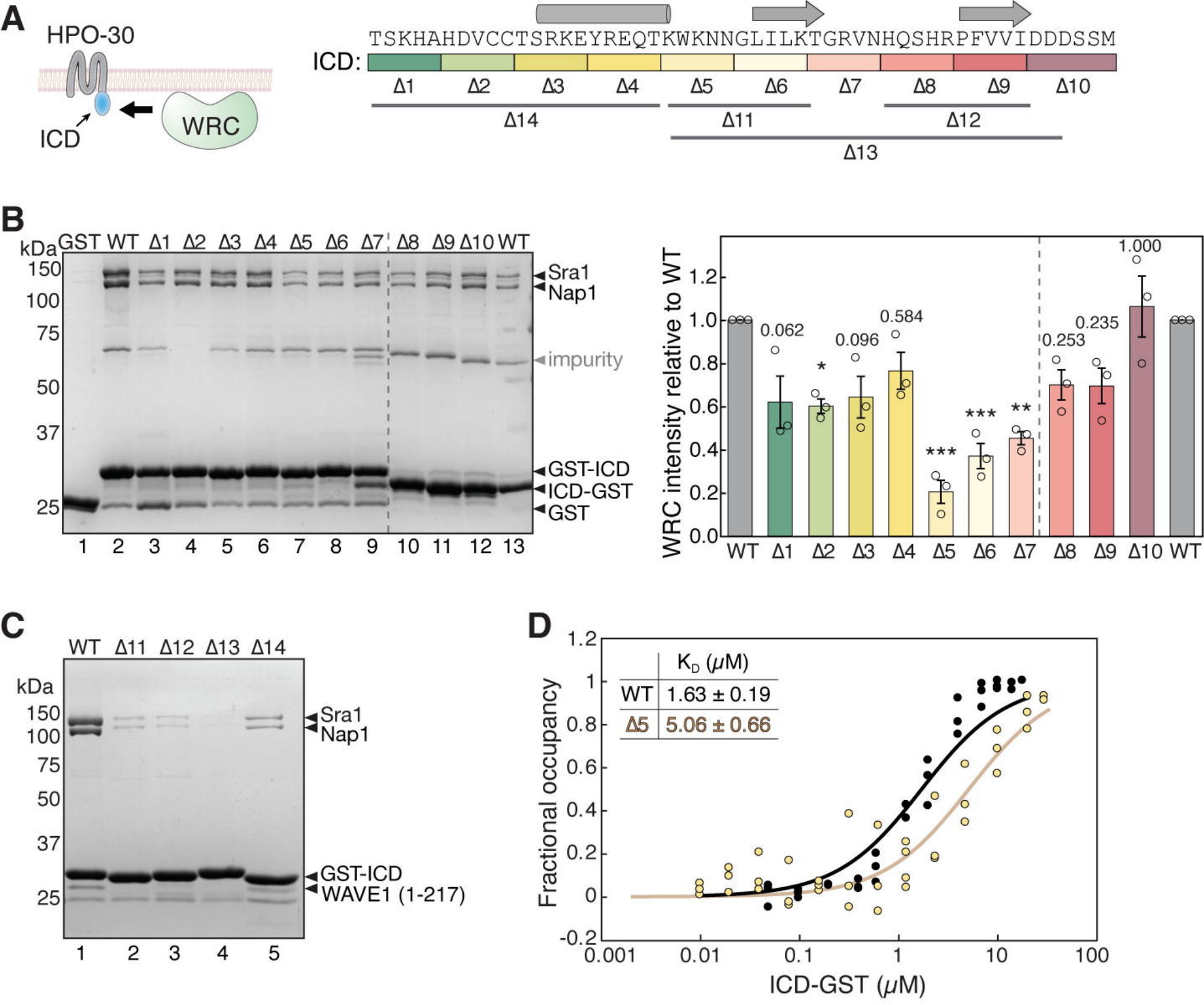
A
HPO-30
ICD
WRC
TSKHAHDVCCTSRKEYREQTKWKNNGLILKTGRVNHQSHRPFVVIDDDSSM
ICD:
Δ1 Δ2 Δ3 Δ4 Δ5 Δ6 Δ7 Δ8 Δ9 Δ10
Δ14
Δ11
Δ12
Δ13
B
kDa
GST WT Δ1 Δ2 Δ3 Δ4 Δ5 Δ6 Δ7 Δ8 Δ9 Δ10 WT
150
100
75
50
37
25
Sra1
Nap1
impurity
GST-ICD
ICD-GST
GST
1 2 3 4 5 6 7 8 9 10 11 12 13
WRC intensity relative to WT
0.062
0.096
0.584
0.253
0.235
1.000
*
***
***
**
WT Δ1 Δ2 Δ3 Δ4 Δ5 Δ6 Δ7 Δ8 Δ9 Δ10 WT
C
WT Δ11 Δ12 Δ13 Δ14
kDa
150
100
75
50
37
25
Sra1
Nap1
GST-ICD
WAVE1 (1-217)
1 2 3 4 5
D
K_D (μM)
WT 1.63 ± 0.19
Δ5 5.06 ± 0.66
Fractional occupancy
ICD-GST (μM)
0.001 0.01 0.1 1 10 100

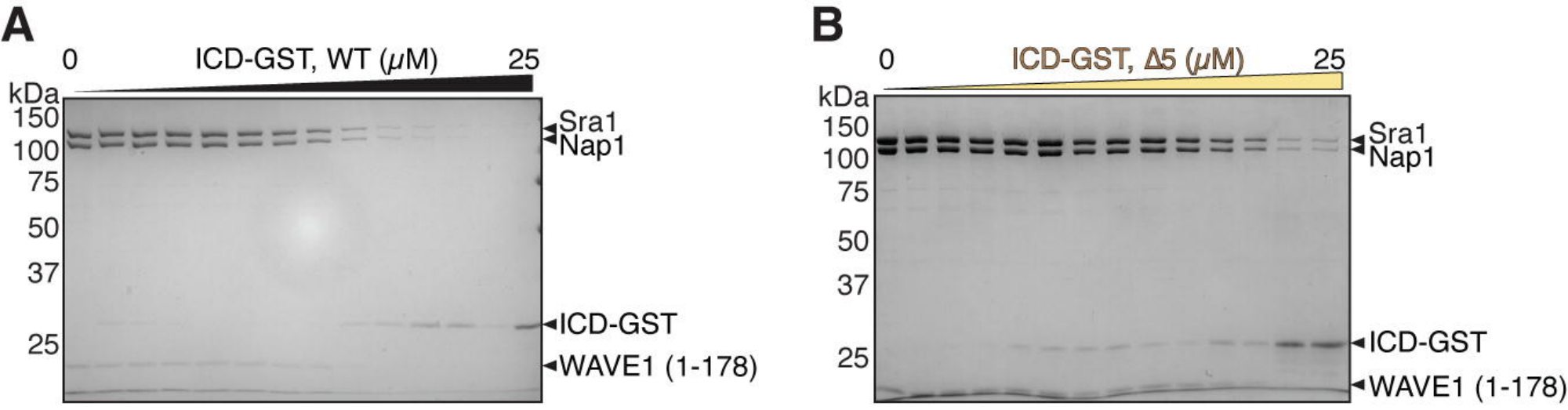
A
0
ICD-GST, WT (μM)
25
kDa
150
100
75
50
37
25
Sra1
Nap1
ICD-GST
WAVE1 (1-178)
B
0
ICD-GST, Δ5 (μM)
25
kDa
150
100
75
50
37
25
Sra1
Nap1
ICD-GST
WAVE1 (1-178)

ICD: TSKHAHDVCCTSRKEYREQTKWKNNGLILKTGRVNHQSHRPFVVIDDDSSM

Program \ Model	Overlay	1	2	3	4	5
LOMETS						
QUARK						
RaptorX						
Rosetta						
AlphaFold 2						
RoseTTAFold						
AlphaFold 2 (HPO-30 FL)						
RoseTTAFold (HPO-30 FL)						

ICD: TSKHAHDVCCTSRKEYREQTKWKNNGLILKTGRVNHQSHRPFVVIDDDSSM

Program	Initial model	Final model	RMSD through MD simulations
LOMETS	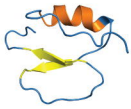	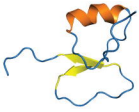	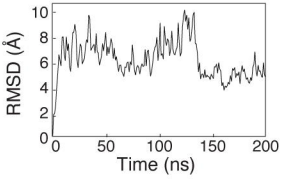
QUARK	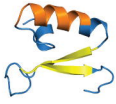	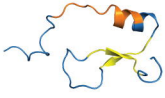	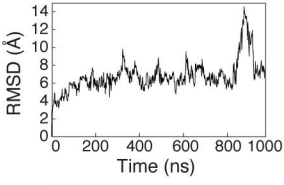
RaptorX	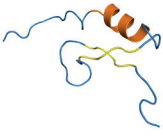	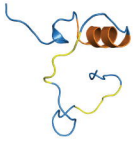	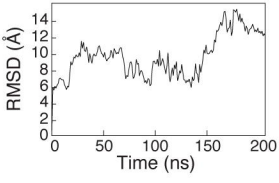
Rosetta	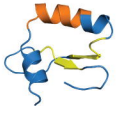	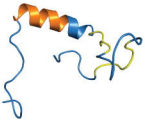	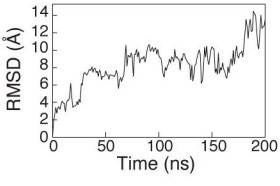
AlphaFold 2		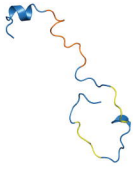	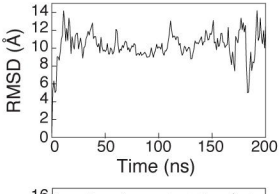
RoseTTAFold	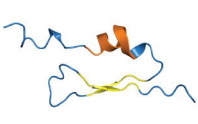		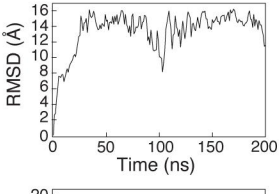
AlphaFold 2 (HPO-30 FL)	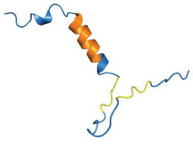	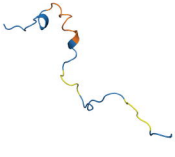	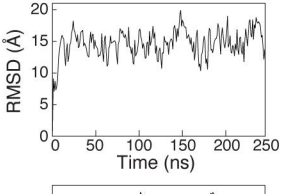
RoseTTAFold (HPO-30 FL)		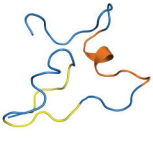	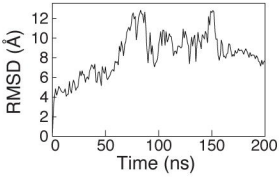

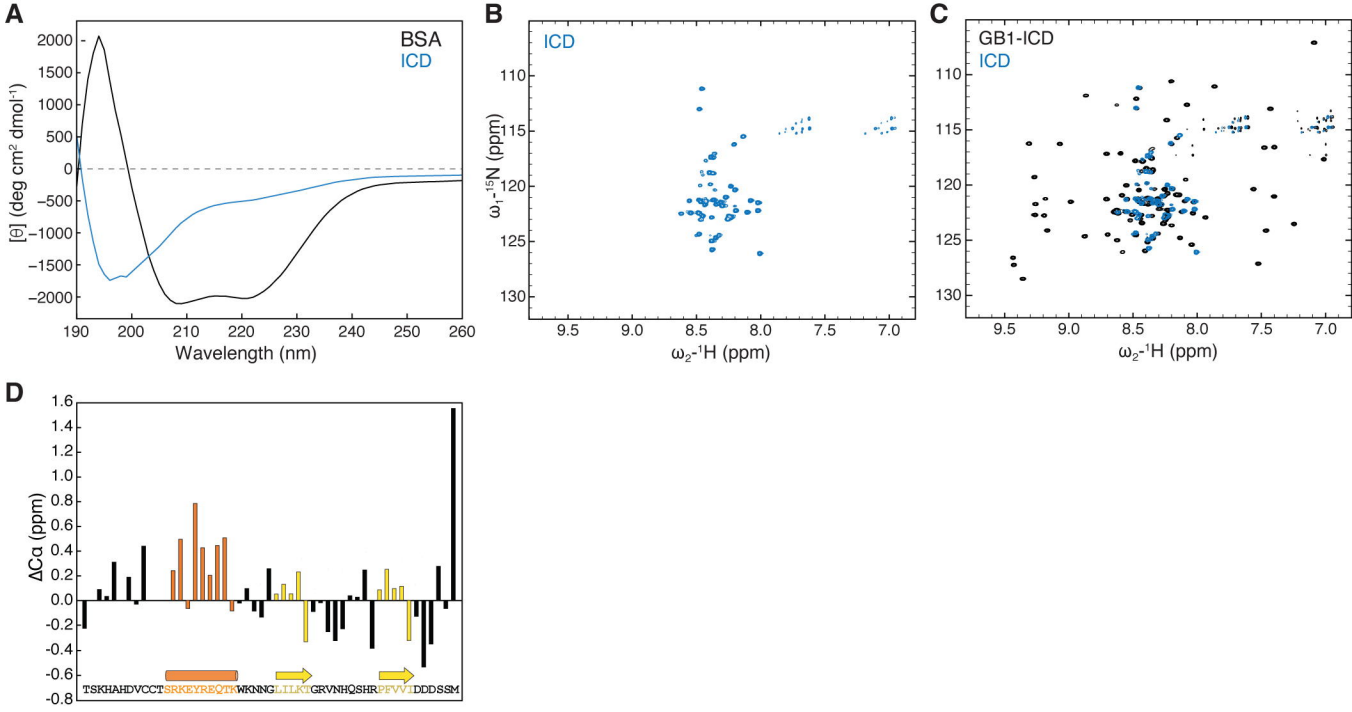
A
BSA
ICD
[θ] (deg cm² dmol⁻¹)
Wavelength (nm)
B
ICD
ω1-15N (ppm)
ω2-1H (ppm)
C
GB1-ICD
ICD
ω2-1H (ppm)
D
ΔCα (ppm)
TSKHAHDVCCTSRKEYREQTKWKNNGLILKTGRVNHQSHRPFVVIDDDSSM

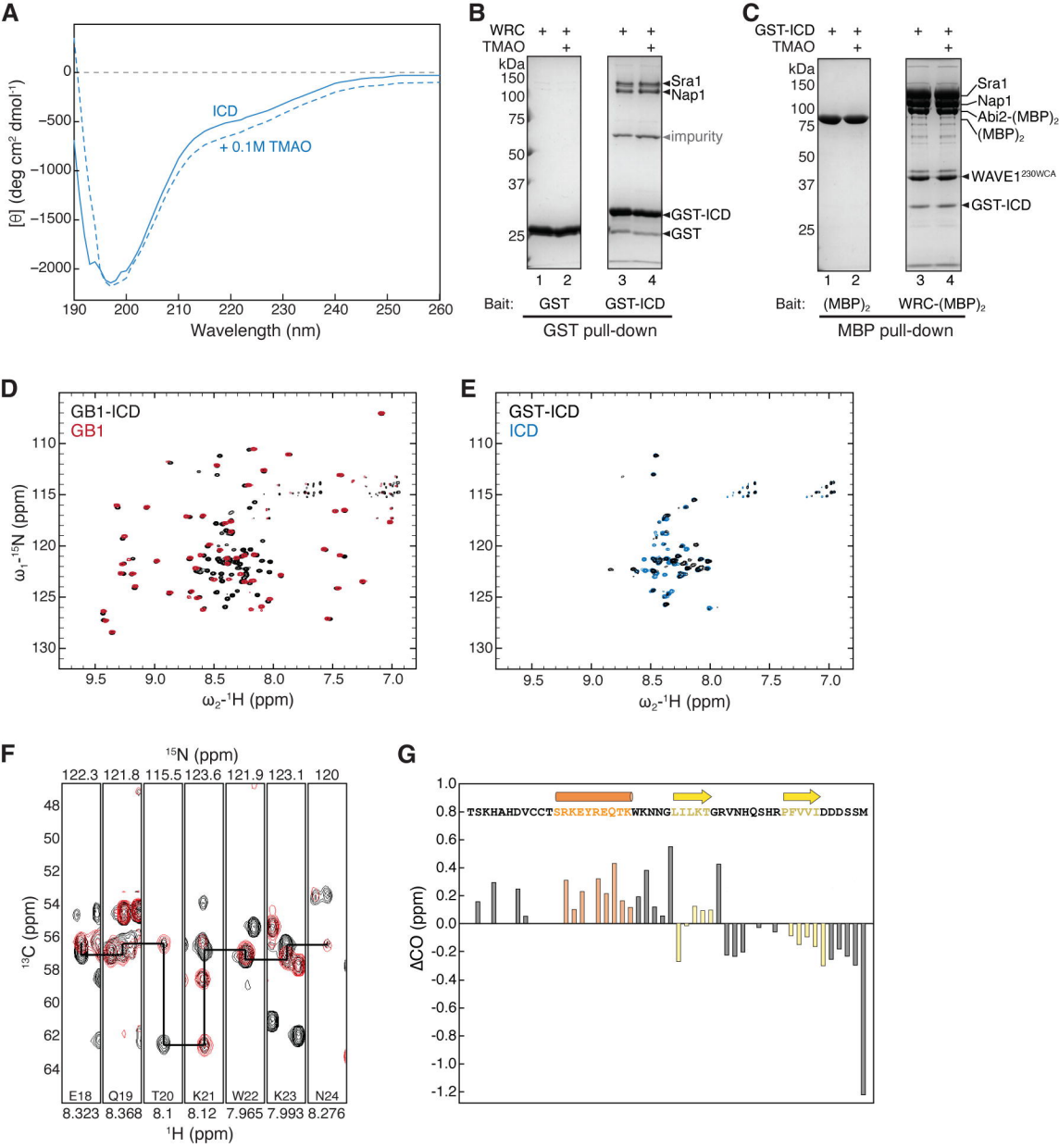
A
ICD
+ 0.1M TMAO
[θ] (deg cm² dmol⁻¹)
Wavelength (nm)
B
WRC
TMAO
kDa
Sra1
Nap1
impurity
GST-ICD
GST
Bait: GST GST-ICD
GST pull-down
C
GST-ICD
TMAO
Sra1
Nap1
Abi2-(MBP)₂
(MBP)₂
WAVE1 230WCA
GST-ICD
Bait: (MBP)₂ WRC-(MBP)₂
MBP pull-down
D
GB1-ICD
GB1
ω₁-¹⁵N (ppm)
ω₂-¹H (ppm)
E
GST-ICD
ICD
ω₂-¹H (ppm)
F
¹⁵N (ppm)
122.3 121.8 115.5 123.6 121.9 123.1 120
¹³C (ppm)
E18 Q19 T20 K21 W22 K23 N24
8.323 8.368 8.1 8.12 7.965 7.993 8.276
¹H (ppm)
G
TSKHAHDVCCTSRKEYREQTKWKNNGLILKTGRVNHQSHRPFVVIDDDSSM
ΔCO (ppm)

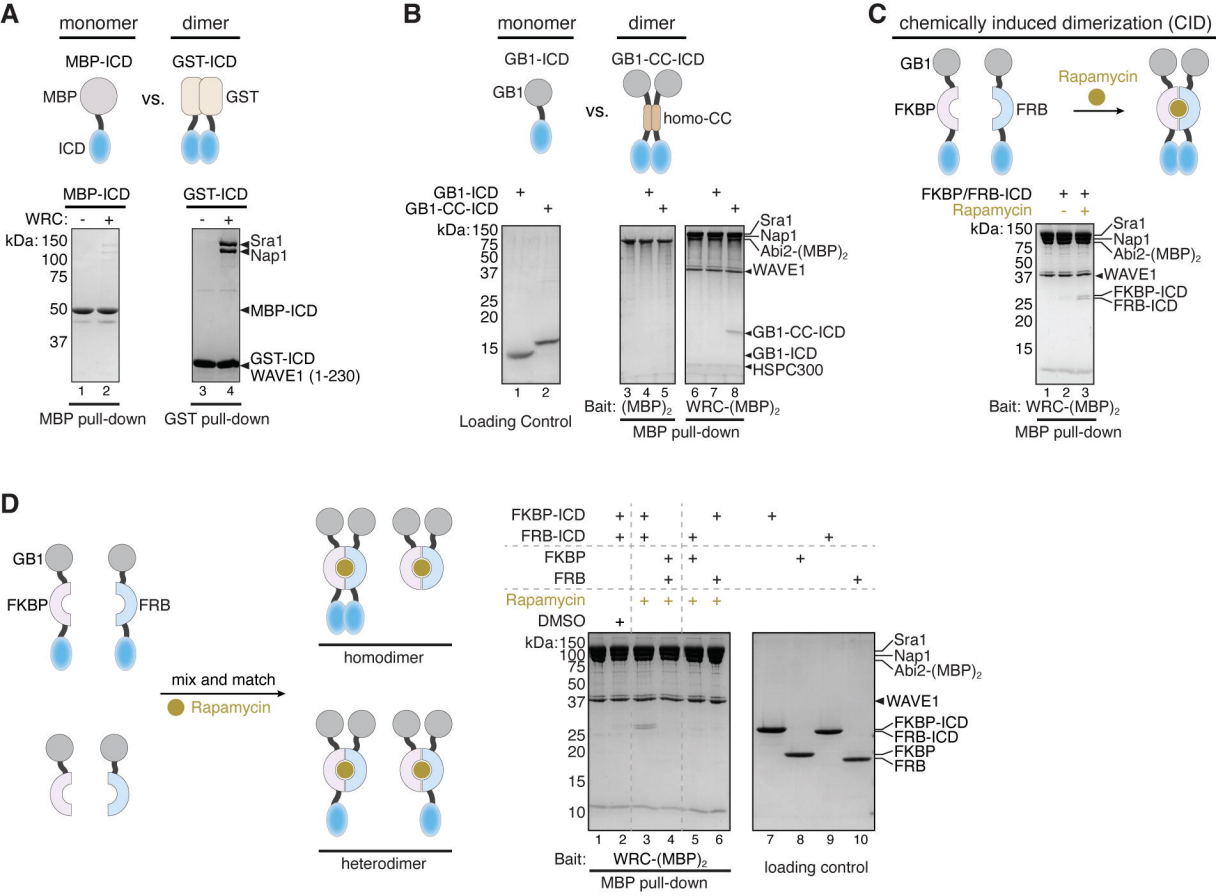
A
monomer
dimer
MBP-ICD
GST-ICD
MBP
ICD
vs.
GST
WRC:
kDa:
150
100
75
50
37
Sra1
Nap1
MBP-ICD
GST-ICD
WAVE1 (1-230)
1 2
3 4
MBP pull-down
GST pull-down
B
monomer
dimer
GB1-ICD
GB1
GB1-CC-ICD
homo-CC
GB1-ICD
GB1-CC-ICD
25
20
15
Sra1
Nap1
Abi2-(MBP)2
WAVE1
GB1-CC-ICD
GB1-ICD
HSPC300
1 2
3 4 5
6 7 8
Bait: (MBP)2
WRC-(MBP)2
Loading Control
MBP pull-down
C
chemically induced dimerization (CID)
GB1
FKBP
FRB
Rapamycin
FKBP/FRB-ICD
Rapamycin
Sra1
Nap1
Abi2-(MBP)2
WAVE1
FKBP-ICD
FRB-ICD
1 2 3
Bait: WRC-(MBP)2
MBP pull-down
D
GB1
FKBP
FRB
mix and match
Rapamycin
homodimer
heterodimer
FKBP-ICD
FRB-ICD
FKBP
FRB
Rapamycin
DMSO
10
Sra1
Nap1
Abi2-(MBP)2
WAVE1
FKBP-ICD
FRB-ICD
FKBP
FRB
1 2 3 4 5 6
7 8 9 10
Bait: WRC-(MBP)2
MBP pull-down
loading control

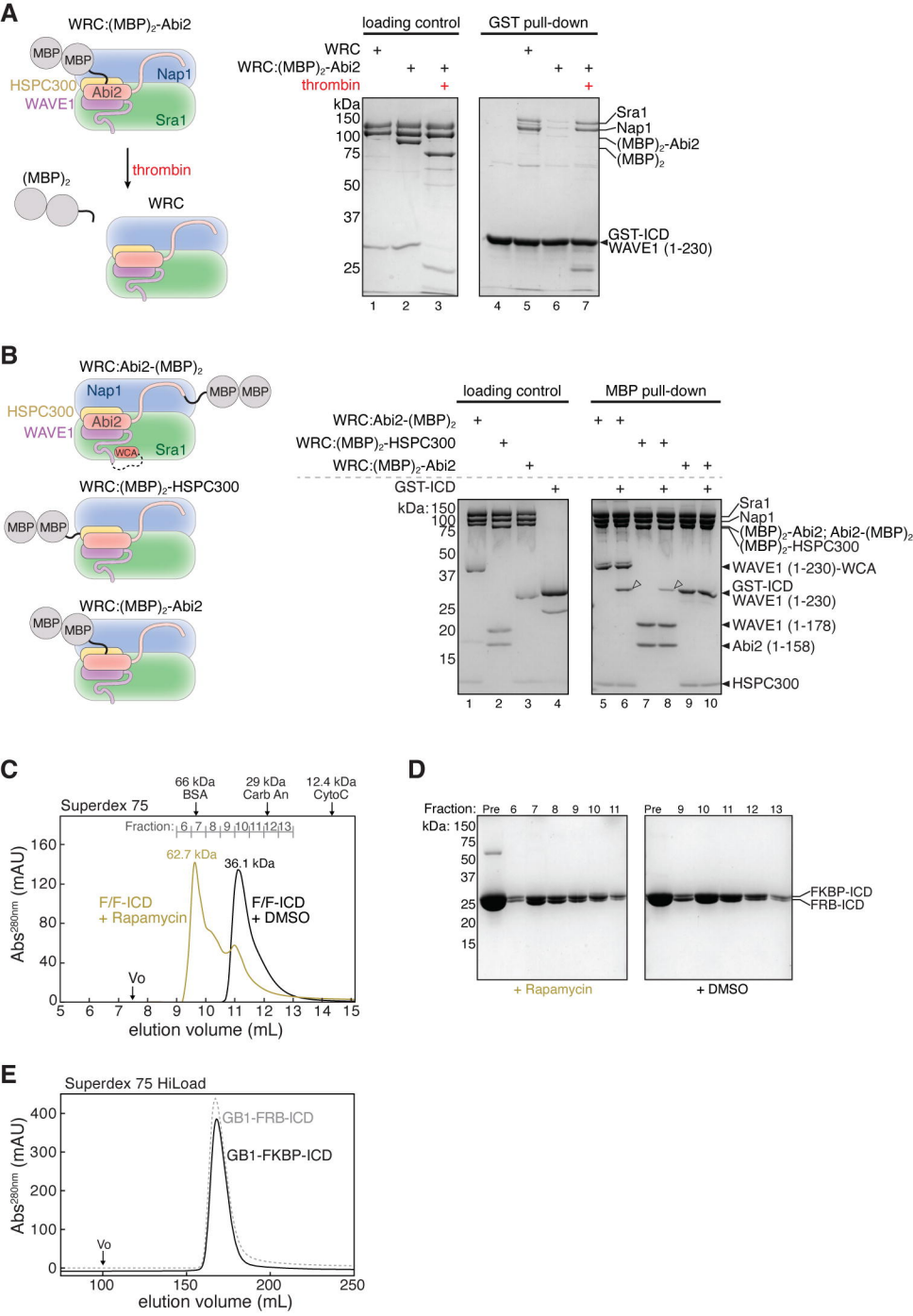
A
WRC:(MBP)2-Abi2
MBP
MBP
Nap1
HSPC300
Abi2
WAVE1
Sra1
thrombin
(MBP)2
WRC
loading control
GST pull-down
WRC
WRC:(MBP)2-Abi2
thrombin
kDa
150
100
75
50
37
25
Sra1
Nap1
(MBP)2-Abi2
(MBP)2
GST-ICD
WAVE1 (1-230)
1 2 3 4 5 6 7
B
WRC:Abi2-(MBP)2
Nap1
MBP MBP
HSPC300
Abi2
WAVE1
WCA
Sra1
WRC:(MBP)2-HSPC300
MBP MBP
WRC:(MBP)2-Abi2
MBP
MBP
loading control
MBP pull-down
WRC:Abi2-(MBP)2
WRC:(MBP)2-HSPC300
WRC:(MBP)2-Abi2
GST-ICD
kDa: 150
100
75
50
37
25
20
15
Sra1
Nap1
(MBP)2-Abi2; Abi2-(MBP)2
(MBP)2-HSPC300
WAVE1 (1-230)-WCA
GST-ICD
WAVE1 (1-230)
WAVE1 (1-178)
Abi2 (1-158)
HSPC300
1 2 3 4 5 6 7 8 9 10
C
66 kDa BSA
29 kDa Carb An
12.4 kDa CytoC
Superdex 75
Fraction: 6 7 8 9 10 11 12 13
62.7 kDa
36.1 kDa
F/F-ICD + Rapamycin
F/F-ICD + DMSO
Vo
Abs280nm (mAU)
160
120
80
40
0
5 6 7 8 9 10 11 12 13 14 15
elution volume (mL)
D
Fraction: Pre 6 7 8 9 10 11
kDa: 150
75
50
37
25
20
15
+ Rapamycin
Pre 9 10 11 12 13
+ DMSO
FKBP-ICD
FRB-ICD
E
Superdex 75 HiLoad
GB1-FRB-ICD
GB1-FKBP-ICD
Vo
Abs280nm (mAU)
400
300
200
100
0
100 150 200 250
elution volume (mL)

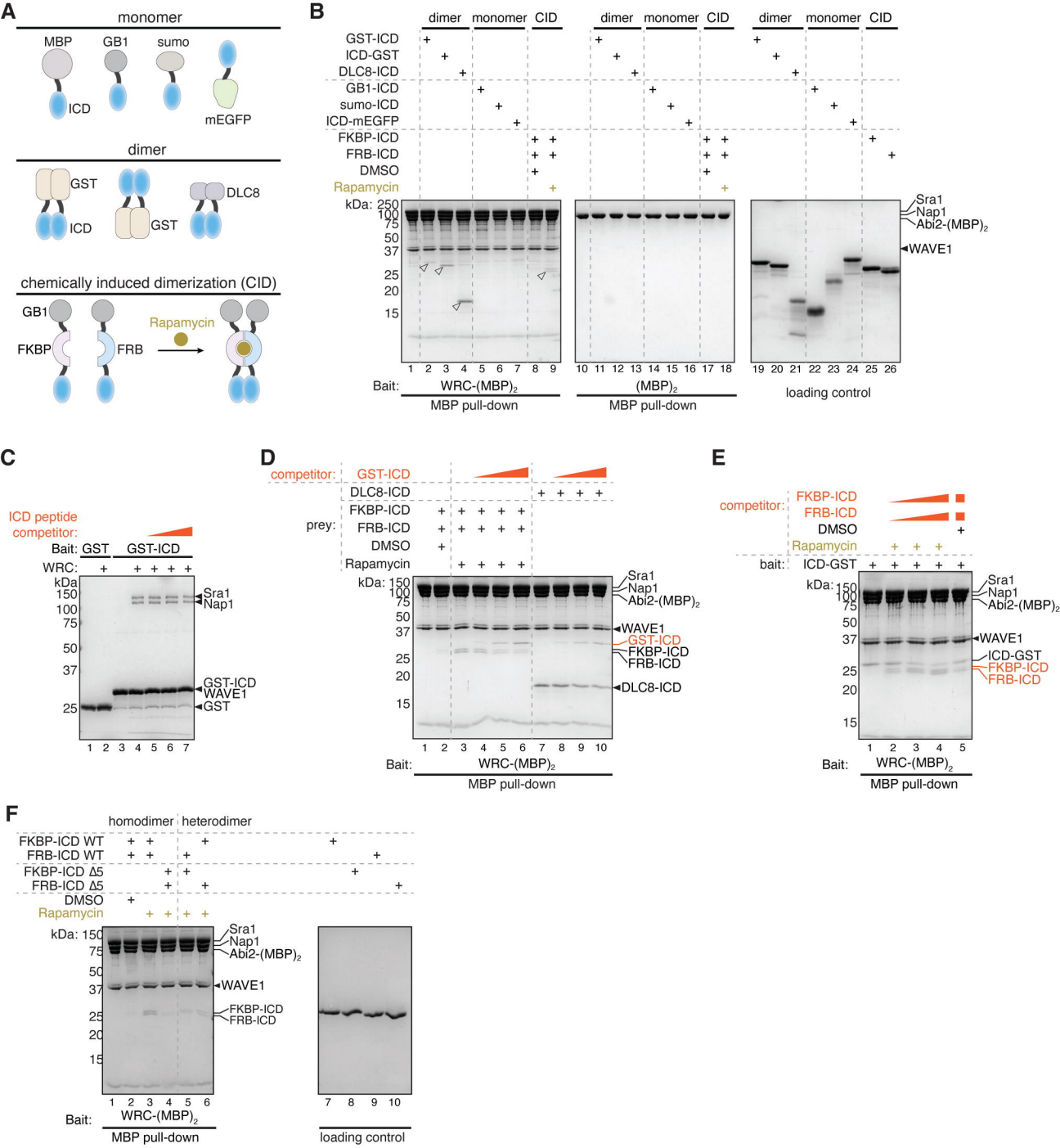
A
monomer
MBP
GB1
sumo
ICD
mEGFP
dimer
GST
ICD
GST
DLC8
chemically induced dimerization (CID)
GB1
FKBP
FRB
Rapamycin
B
dimer
monomer
CID
GST-ICD
ICD-GST
DLC8-ICD
GB1-ICD
sumo-ICD
ICD-mEGFP
FKBP-ICD
FRB-ICD
DMSO
Rapamycin
kDa: 250
100
75
50
37
25
20
15
Sra1
Nap1
Abi2-(MBP)2
WAVE1
Bait:
WRC-(MBP)2
(MBP)2
MBP pull-down
loading control
C
ICD peptide competitor:
Bait: GST
GST-ICD
WRC:
kDa
150
100
75
50
37
25
Sra1
Nap1
GST-ICD
WAVE1
GST
D
competitor:
GST-ICD
DLC8-ICD
prey:
FKBP-ICD
FRB-ICD
DMSO
Rapamycin
kDa: 150
100
75
50
37
25
20
15
Sra1
Nap1
Abi2-(MBP)2
WAVE1
GST-ICD
FKBP-ICD
FRB-ICD
DLC8-ICD
Bait:
WRC-(MBP)2
MBP pull-down
E
competitor:
FKBP-ICD
FRB-ICD
DMSO
Rapamycin
bait:
ICD-GST
kDa: 150
100
75
50
37
25
20
15
Sra1
Nap1
Abi2-(MBP)2
WAVE1
ICD-GST
FKBP-ICD
FRB-ICD
Bait:
WRC-(MBP)2
MBP pull-down
F
homodimer
heterodimer
FKBP-ICD WT
FRB-ICD WT
FKBP-ICD Δ5
FRB-ICD Δ5
DMSO
Rapamycin
kDa: 150
75
50
37
25
20
15
Sra1
Nap1
Abi2-(MBP)2
WAVE1
FKBP-ICD
FRB-ICD
Bait:
WRC-(MBP)2
MBP pull-down
loading control

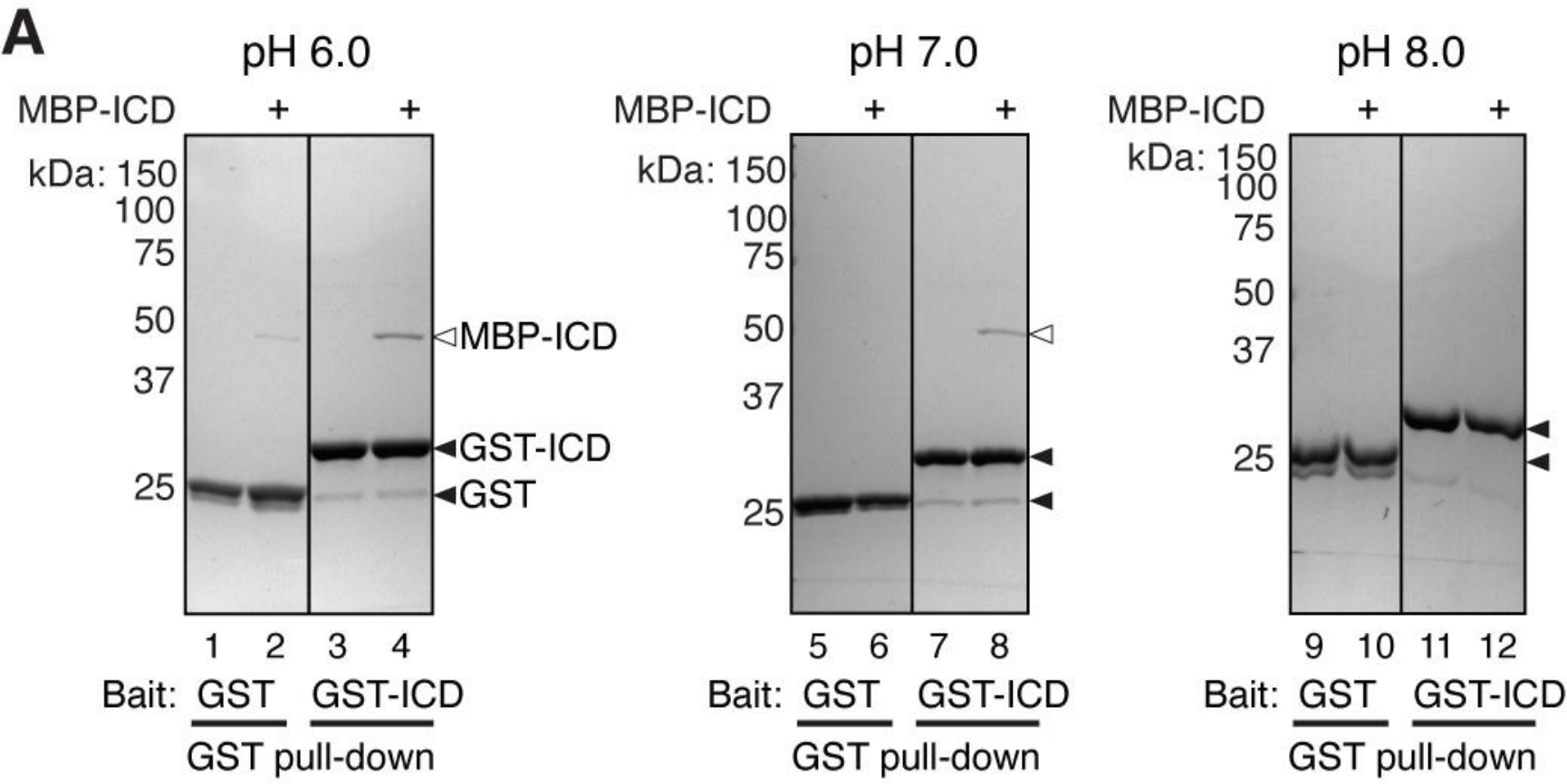
A
pH 6.0
pH 7.0
pH 8.0
MBP-ICD
kDa: 150
100
75
50
37
25
MBP-ICD
GST-ICD
GST
1 2 3 4
5 6 7 8
9 10 11 12
Bait: GST GST-ICD
GST pull-down

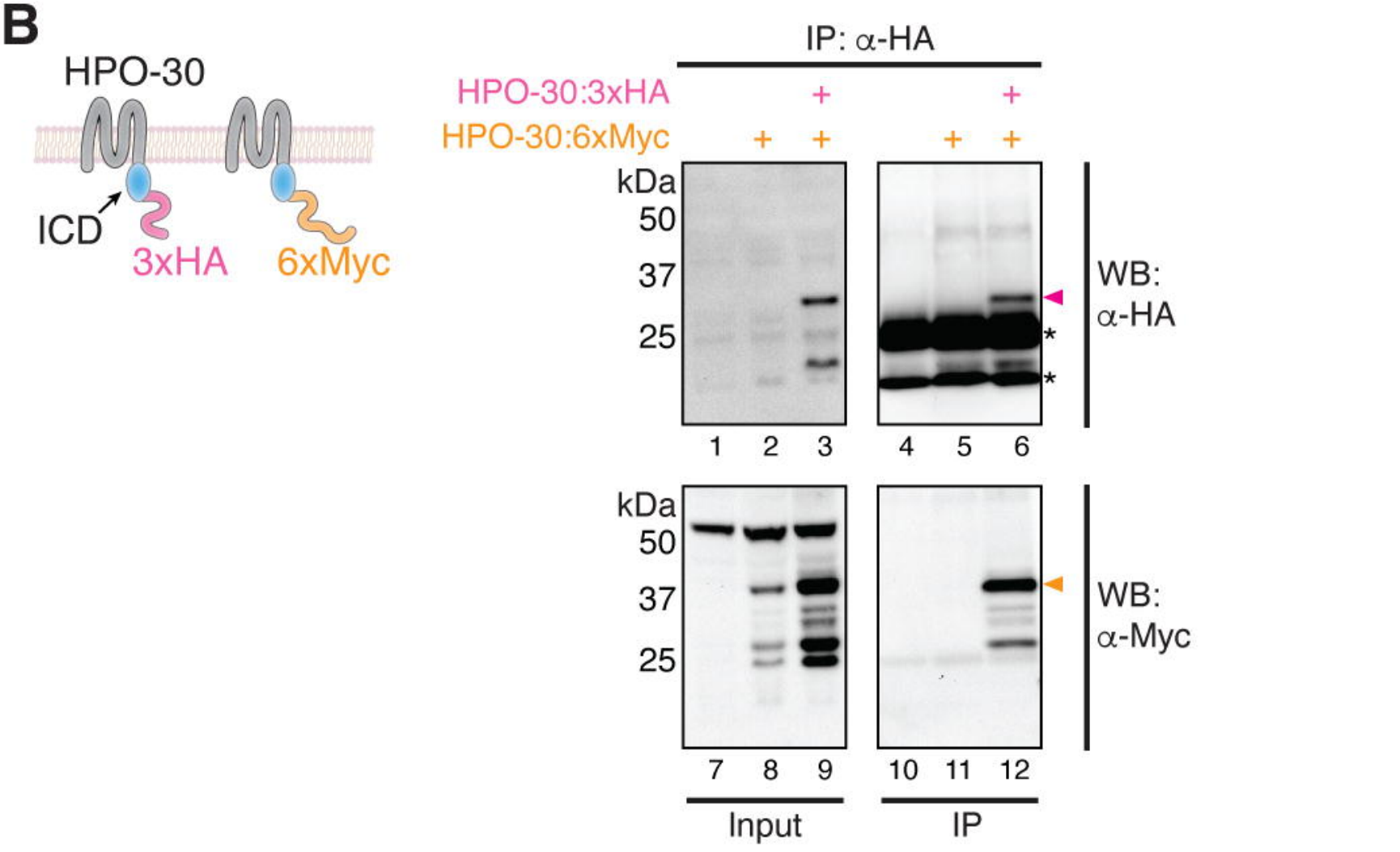
B
HPO-30
ICD
3xHA
6xMyc
IP: α-HA
HPO-30:3xHA
HPO-30:6xMyc
kDa
50
37
25
WB: α-HA
WB: α-Myc
1 2 3 4 5 6
7 8 9 10 11 12
Input
IP

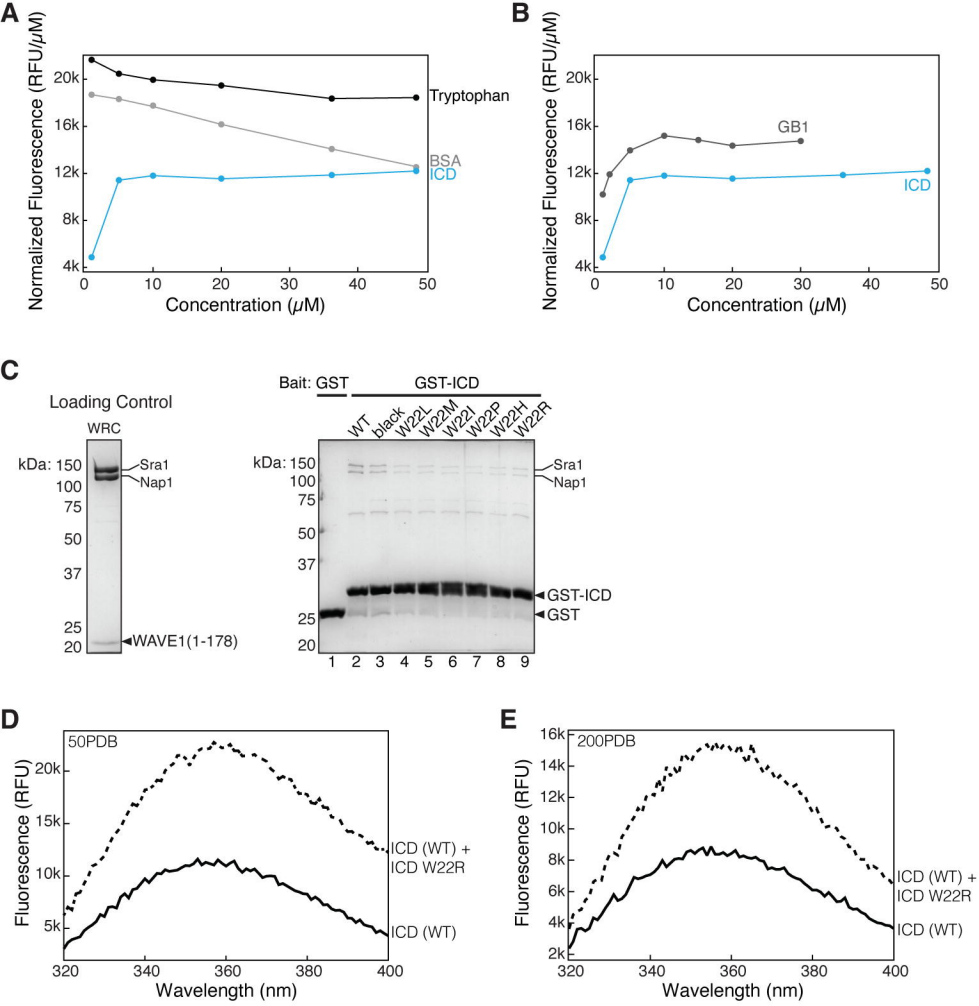
A
Normalized Fluorescence (RFU/μM)
20k
16k
12k
8k
4k
0
10
20
30
40
50
Concentration (μM)
Tryptophan
BSA
ICD
B
Normalized Fluorescence (RFU/μM)
GB1
ICD
Concentration (μM)
C
Loading Control
WRC
kDa: 150
100
75
50
37
25
20
Sra1
Nap1
WAVE1(1-178)
Bait: GST
GST-ICD
WT
black
W22L
W22M
W22I
W22P
W22H
W22R
GST-ICD
GST
1 2 3 4 5 6 7 8 9
D
50PDB
Fluorescence (RFU)
ICD (WT) +
ICD W22R
ICD (WT)
Wavelength (nm)
E
200PDB
Fluorescence (RFU)
ICD (WT) +
ICD W22R
ICD (WT)
Wavelength (nm)

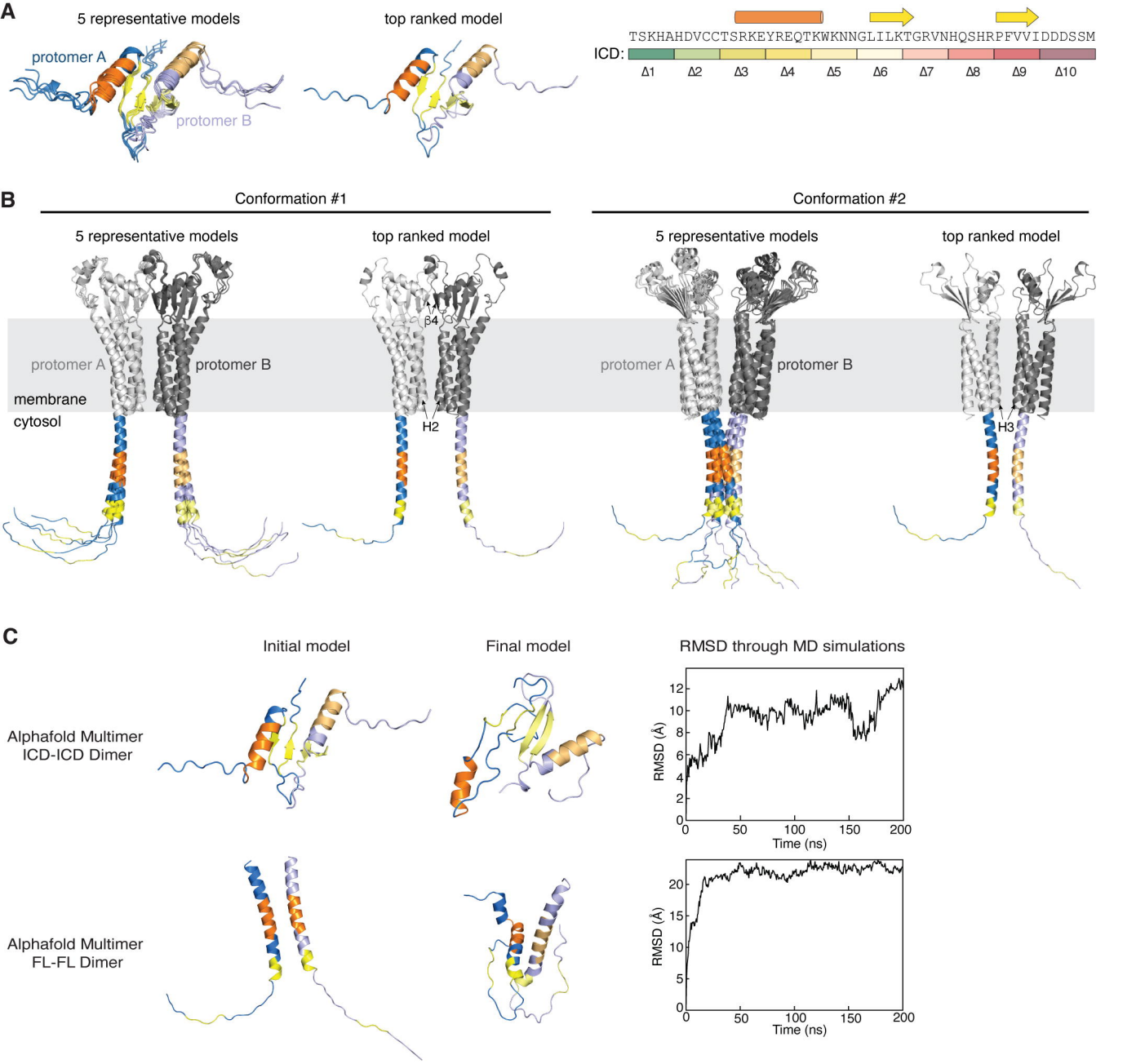
A
5 representative models
top ranked model
protomer A
protomer B
TSKHAHDVCCTSRKEYREQTKWKNNGLILKTGRVNHQSHRPFVVIDDDSSM
ICD:
Δ1
Δ2
Δ3
Δ4
Δ5
Δ6
Δ7
Δ8
Δ9
Δ10
B
Conformation #1
Conformation #2
5 representative models
top ranked model
5 representative models
top ranked model
protomer A
protomer B
membrane
cytosol
β4
H2
protomer A
protomer B
H3
C
Initial model
Final model
RMSD through MD simulations
Alphafold Multimer
ICD-ICD Dimer
RMSD (Å)
Time (ns)
Alphafold Multimer
FL-FL Dimer
RMSD (Å)
Time (ns)

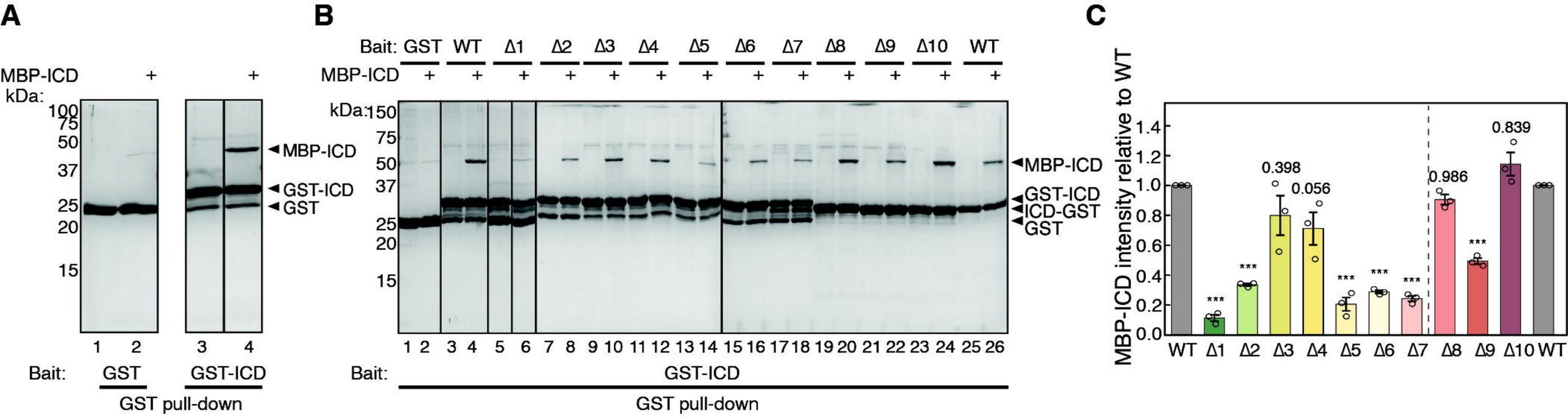
A
MBP-ICD
kDa:
100
75
50
37
25
20
15
MBP-ICD
GST-ICD
GST
1 2 3 4
Bait: GST GST-ICD
GST pull-down
B
Bait: GST WT Δ1 Δ2 Δ3 Δ4 Δ5 Δ6 Δ7 Δ8 Δ9 Δ10 WT
MBP-ICD
kDa:
150
75
50
37
25
20
15
MBP-ICD
GST-ICD
ICD-GST
GST
1 2 3 4 5 6 7 8 9 10 11 12 13 14 15 16 17 18 19 20 21 22 23 24 25 26
Bait: GST-ICD
GST pull-down
C
MBP-ICD intensity relative to WT
1.4
1.2
1.0
0.8
0.6
0.4
0.2
0.0
0.398
0.056
0.986
0.839
***
WT Δ1 Δ2 Δ3 Δ4 Δ5 Δ6 Δ7 Δ8 Δ9 Δ10 WT

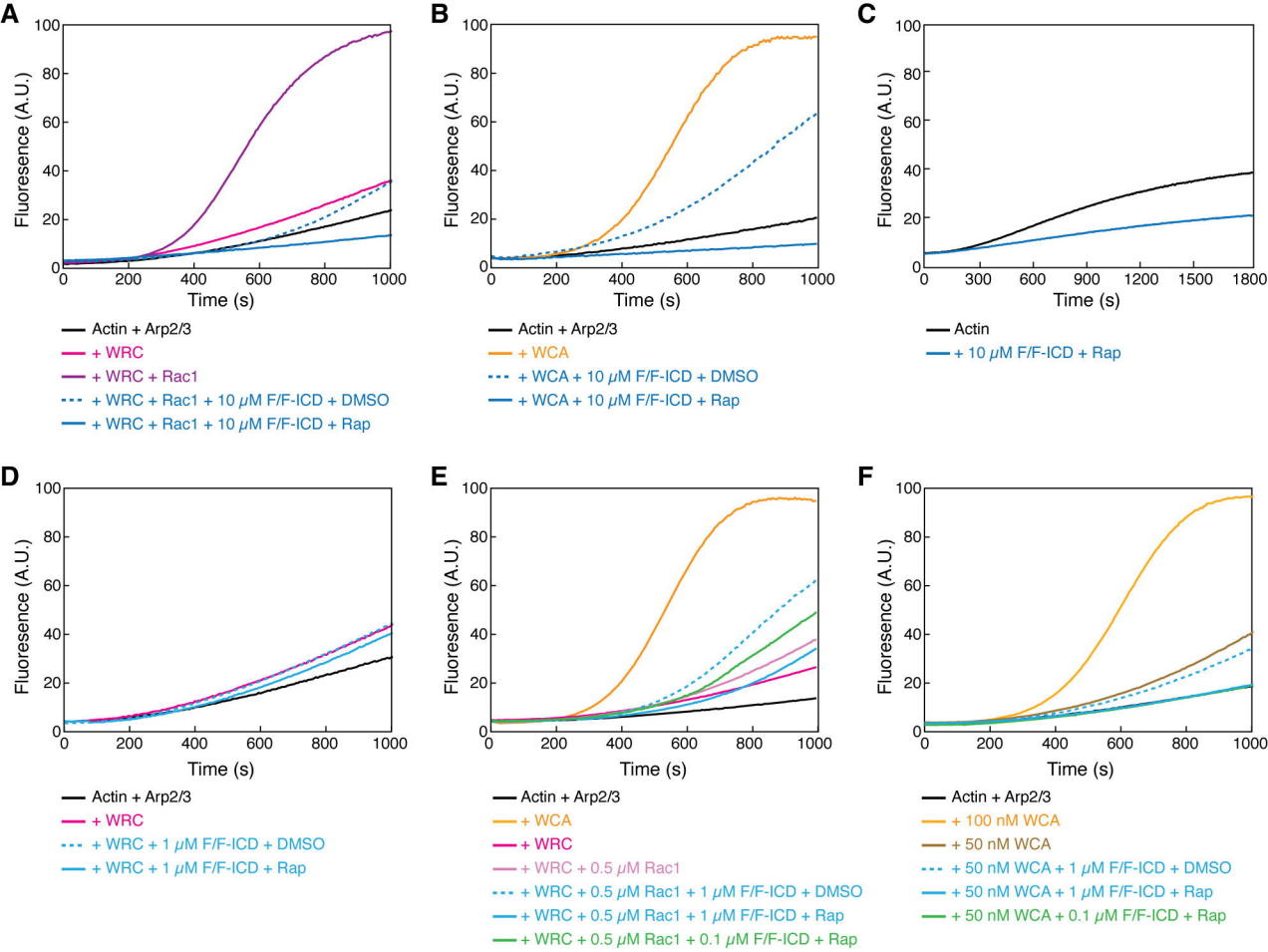
A
Fluoresence (A.U.)
Time (s)
Actin + Arp2/3
+ WRC
+ WRC + Rac1
+ WRC + Rac1 + 10 μM F/F-ICD + DMSO
+ WRC + Rac1 + 10 μM F/F-ICD + Rap
B
Fluoresence (A.U.)
Time (s)
Actin + Arp2/3
+ WCA
+ WCA + 10 μM F/F-ICD + DMSO
+ WCA + 10 μM F/F-ICD + Rap
C
Fluoresence (A.U.)
Time (s)
Actin
+ 10 μM F/F-ICD + Rap
D
Fluoresence (A.U.)
Time (s)
Actin + Arp2/3
+ WRC
+ WRC + 1 μM F/F-ICD + DMSO
+ WRC + 1 μM F/F-ICD + Rap
E
Fluoresence (A.U.)
Time (s)
Actin + Arp2/3
+ WCA
+ WRC
+ WRC + 0.5 μM Rac1
+ WRC + 0.5 μM Rac1 + 1 μM F/F-ICD + DMSO
+ WRC + 0.5 μM Rac1 + 1 μM F/F-ICD + Rap
+ WRC + 0.5 μM Rac1 + 0.1 μM F/F-ICD + Rap
F
Fluoresence (A.U.)
Time (s)
Actin + Arp2/3
+ 100 nM WCA
+ 50 nM WCA
+ 50 nM WCA + 1 μM F/F-ICD + DMSO
+ 50 nM WCA + 1 μM F/F-ICD + Rap
+ 50 nM WCA + 0.1 μM F/F-ICD + Rap

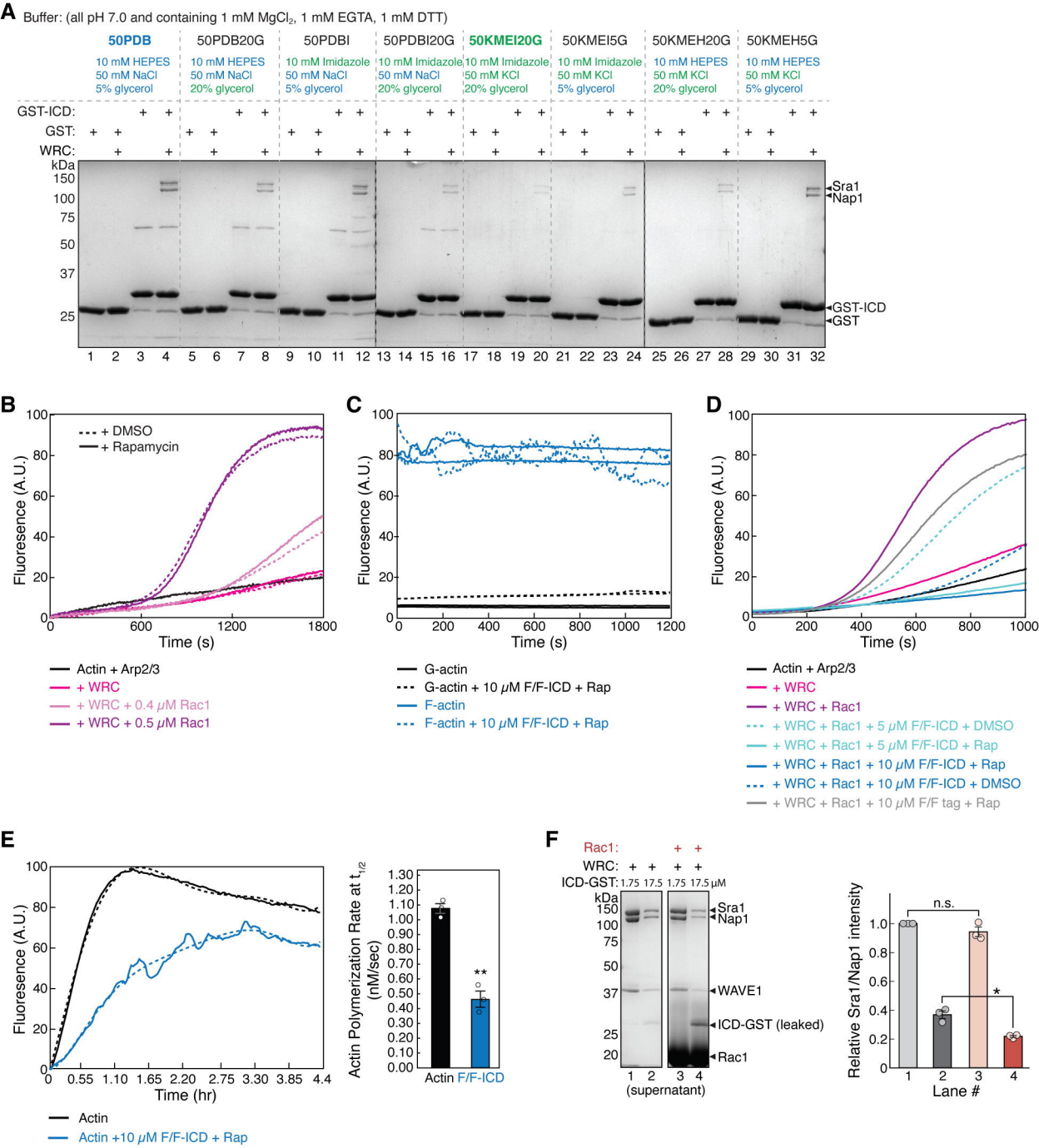
A
Buffer: (all pH 7.0 and containing 1 mM MgCl2, 1 mM EGTA, 1 mM DTT)
50PDB
10 mM HEPES
50 mM NaCl
5% glycerol
50PDB20G
10 mM HEPES
50 mM NaCl
20% glycerol
50PDBI
10 mM Imidazole
50 mM NaCl
5% glycerol
50PDBI20G
10 mM Imidazole
50 mM NaCl
20% glycerol
50KMEI20G
10 mM Imidazole
50 mM KCl
20% glycerol
50KMEI5G
10 mM Imidazole
50 mM KCl
5% glycerol
50KMEH20G
10 mM HEPES
50 mM KCl
20% glycerol
50KMEH5G
10 mM HEPES
50 mM KCl
5% glycerol
GST-ICD:
GST:
WRC:
kDa
150
100
75
50
37
25
Sra1
Nap1
GST-ICD
GST
1 2 3 4 5 6 7 8 9 10 11 12 13 14 15 16 17 18 19 20 21 22 23 24 25 26 27 28 29 30 31 32
B
Fluoresence (A.U.)
Time (s)
+ DMSO
+ Rapamycin
Actin + Arp2/3
+ WRC
+ WRC + 0.4 μM Rac1
+ WRC + 0.5 μM Rac1
C
Fluoresence (A.U.)
Time (s)
G-actin
G-actin + 10 μM F/F-ICD + Rap
F-actin
F-actin + 10 μM F/F-ICD + Rap
D
Fluoresence (A.U.)
Time (s)
Actin + Arp2/3
+ WRC
+ WRC + Rac1
+ WRC + Rac1 + 5 μM F/F-ICD + DMSO
+ WRC + Rac1 + 5 μM F/F-ICD + Rap
+ WRC + Rac1 + 10 μM F/F-ICD + Rap
+ WRC + Rac1 + 10 μM F/F-ICD + DMSO
+ WRC + Rac1 + 10 μM F/F tag + Rap
E
Fluoresence (A.U.)
Time (hr)
Actin
Actin +10 μM F/F-ICD + Rap
Actin Polymerization Rate at t1/2 (nM/sec)
**
Actin
F/F-ICD
F
Rac1:
WRC:
ICD-GST: 1.75 17.5 1.75 17.5 μM
kDa
Sra1
Nap1
WAVE1
ICD-GST (leaked)
Rac1
1 2 3 4
(supernatant)
Relative Sra1/Nap1 intensity
n.s.
*
Lane #

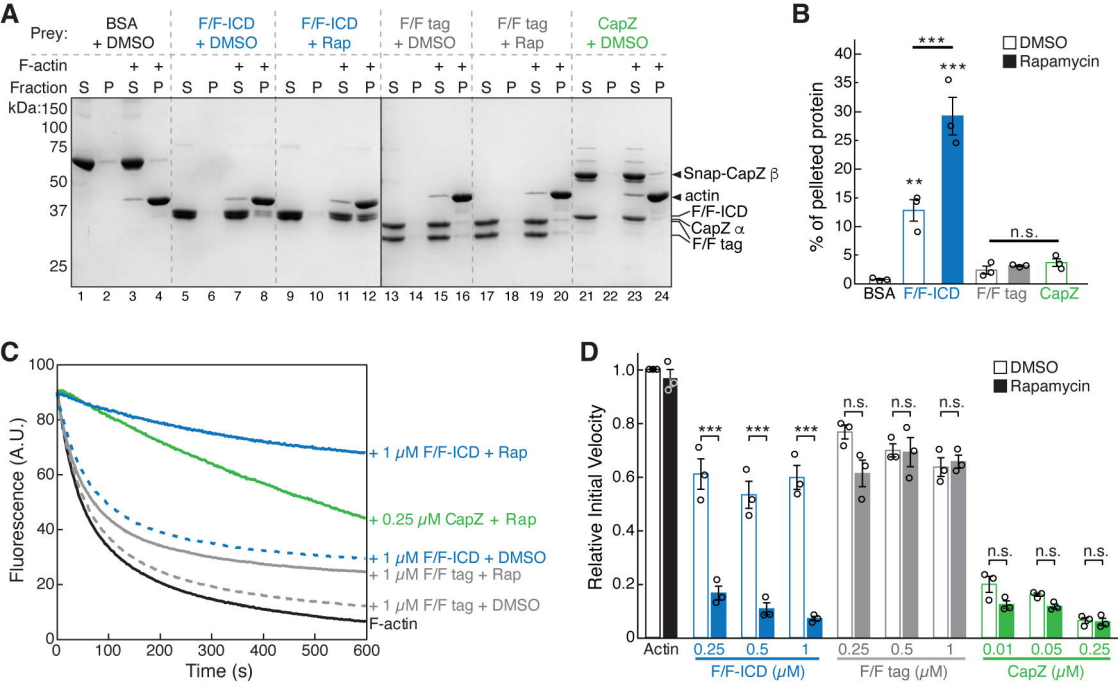
A
Prey:
BSA + DMSO
F/F-ICD + DMSO
F/F-ICD + Rap
F/F tag + DMSO
F/F tag + Rap
CapZ + DMSO
F-actin
Fraction
S P S P S P S P S P S P S P S P S P S P S P S P
kDa:150
100
75
50
37
25
Snap-CapZ β
actin
F/F-ICD
CapZ α
F/F tag
1 2 3 4 5 6 7 8 9 10 11 12 13 14 15 16 17 18 19 20 21 22 23 24
B
DMSO
Rapamycin
% of pelleted protein
***
***
**
n.s.
BSA
F/F-ICD
F/F tag
CapZ
C
Fluorescence (A.U.)
Time (s)
+ 1 μM F/F-ICD + Rap
+ 0.25 μM CapZ + Rap
+ 1 μM F/F-ICD + DMSO
+ 1 μM F/F tag + Rap
+ 1 μM F/F tag + DMSO
F-actin
D
DMSO
Rapamycin
Relative Initial Velocity
Actin
0.25
0.5
1
0.25
0.5
1
0.01
0.05
0.25
F/F-ICD (μM)
F/F tag (μM)
CapZ (μM)

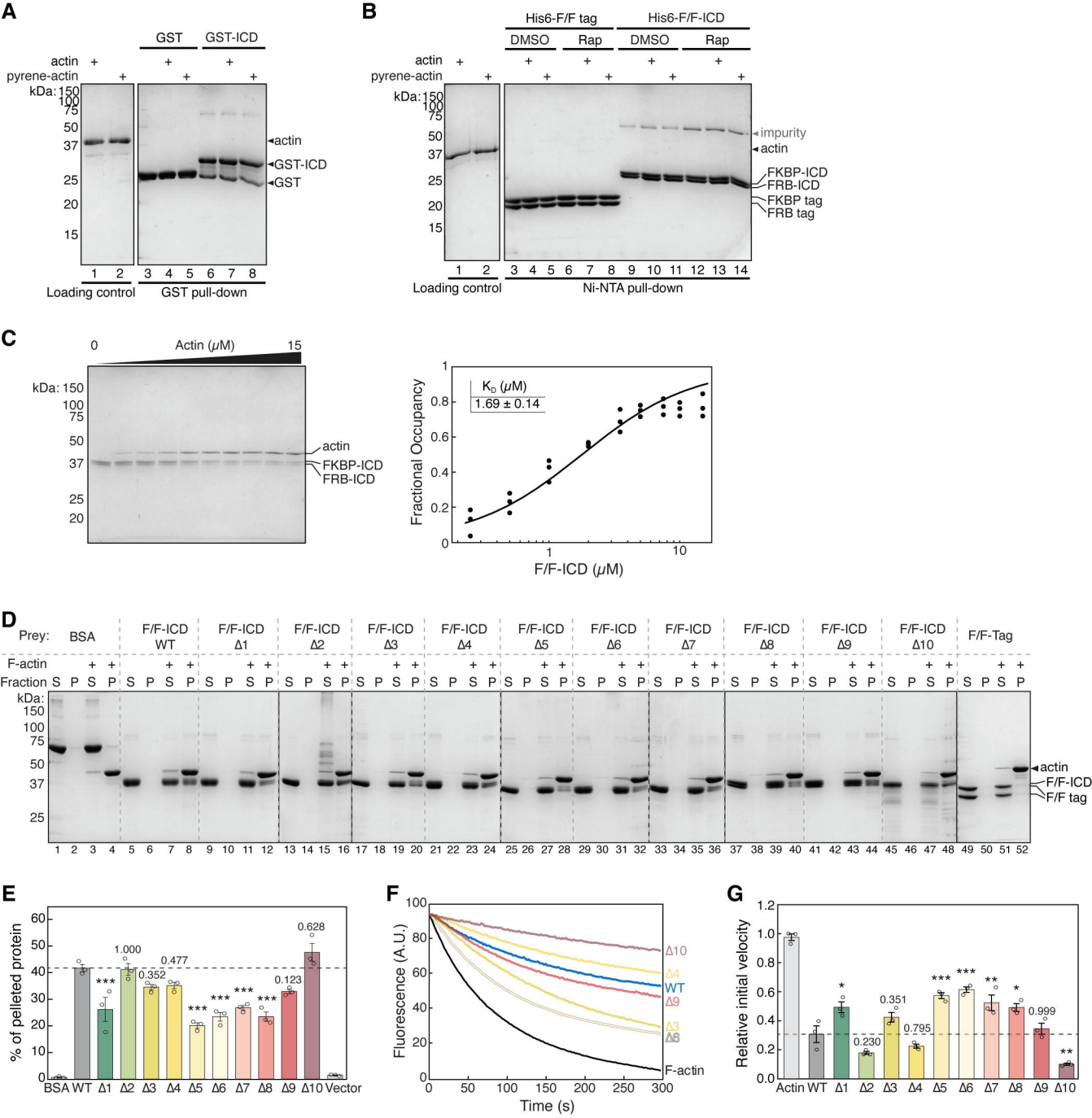
A
GST
GST-ICD
actin
pyrene-actin
kDa: 150 100 75 50 37 25 20 15
actin
GST-ICD
GST
1 2 3 4 5 6 7 8
Loading control
GST pull-down
B
His6-F/F tag
His6-F/F-ICD
DMSO
Rap
DMSO
Rap
actin
pyrene-actin
kDa: 150 100 75 50 37 25 20 15
impurity
actin
FKBP-ICD
FRB-ICD
FKBP tag
FRB tag
1 2 3 4 5 6 7 8 9 10 11 12 13 14
Loading control
Ni-NTA pull-down
C
0
Actin (μM)
15
kDa: 150 100 75 50 37 25 20
actin
FKBP-ICD
FRB-ICD
Fractional Occupancy
K_D (μM)
1.69 ± 0.14
F/F-ICD (μM)
D
Prey:
BSA
F/F-ICD WT
F/F-ICD Δ1
F/F-ICD Δ2
F/F-ICD Δ3
F/F-ICD Δ4
F/F-ICD Δ5
F/F-ICD Δ6
F/F-ICD Δ7
F/F-ICD Δ8
F/F-ICD Δ9
F/F-ICD Δ10
F/F-Tag
F-actin
Fraction S P S P
kDa: 150 100 75 50 37 25
actin
F/F-ICD
F/F tag
E
% of pelleted protein
1.000
0.477
0.352
0.628
0.123
BSA WT Δ1 Δ2 Δ3 Δ4 Δ5 Δ6 Δ7 Δ8 Δ9 Δ10 Vector
F
Fluorescence (A.U.)
Time (s)
Δ10
Δ4
WT
Δ9
Δ3
Δ6
F-actin
G
Relative initial velocity
0.230
0.351
0.795
0.999
Actin WT Δ1 Δ2 Δ3 Δ4 Δ5 Δ6 Δ7 Δ8 Δ9 Δ10

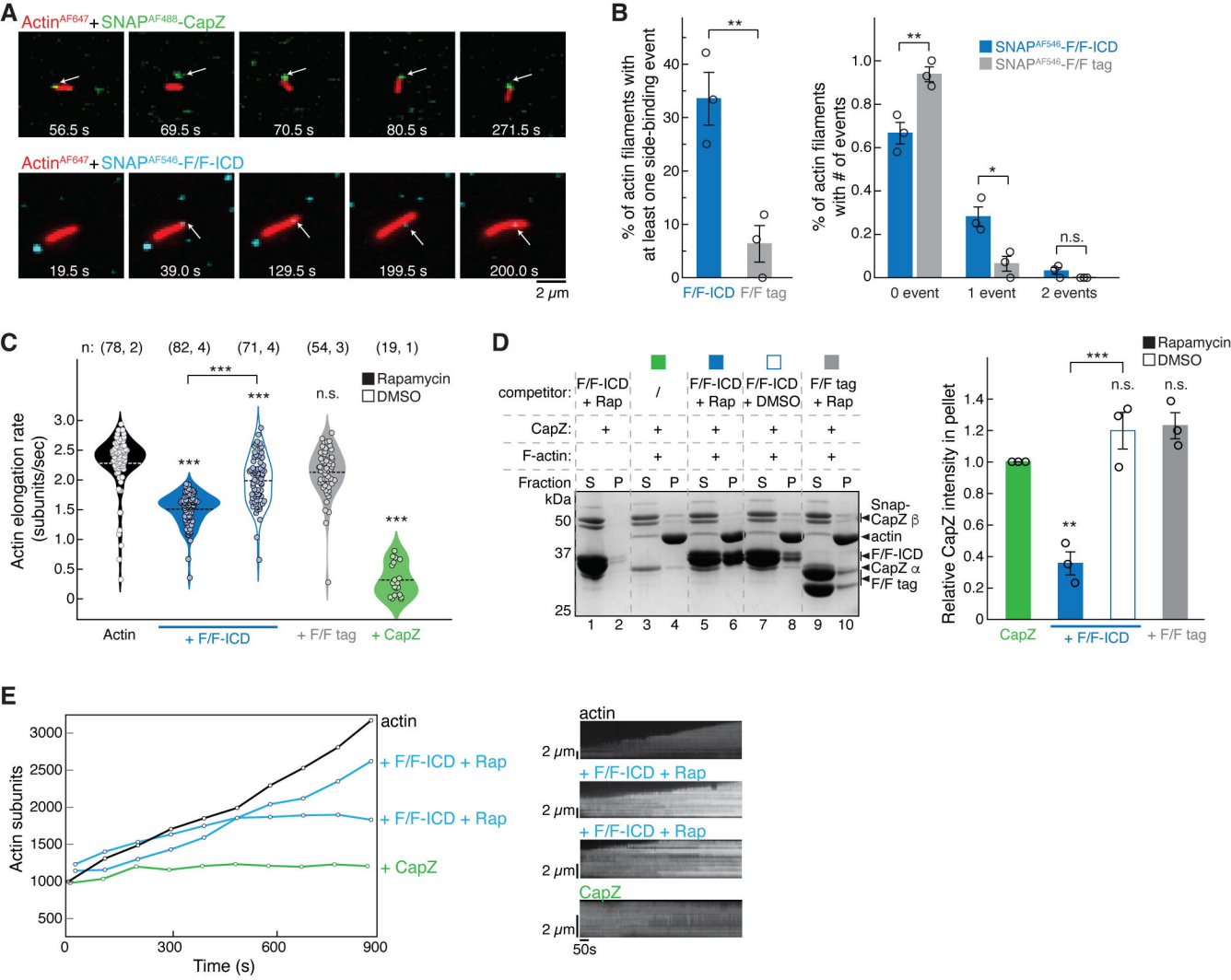
A
Actin^AF647 + SNAP^AF488-CapZ
56.5 s
69.5 s
70.5 s
80.5 s
271.5 s
Actin^AF647 + SNAP^AF546-F/F-ICD
19.5 s
39.0 s
129.5 s
199.5 s
200.0 s
2 μm
B
% of actin filaments with at least one side-binding event
F/F-ICD
F/F tag
% of actin filaments with # of events
SNAP^AF546-F/F-ICD
SNAP^AF546-F/F tag
0 event
1 event
2 events
n.s.
C
n: (78, 2) (82, 4) (71, 4) (54, 3) (19, 1)
Rapamycin
DMSO
Actin elongation rate (subunits/sec)
Actin
+ F/F-ICD
+ F/F tag
+ CapZ
D
competitor:
F/F-ICD + Rap
F/F-ICD + Rap
F/F-ICD + DMSO
F/F tag + Rap
CapZ:
F-actin:
Fraction
kDa
Snap-CapZ β
actin
F/F-ICD
CapZ α
F/F tag
Relative CapZ intensity in pellet
CapZ
+ F/F-ICD
+ F/F tag
E
Actin subunits
Time (s)
actin
+ F/F-ICD + Rap
+ F/F-ICD + Rap
+ CapZ
50s

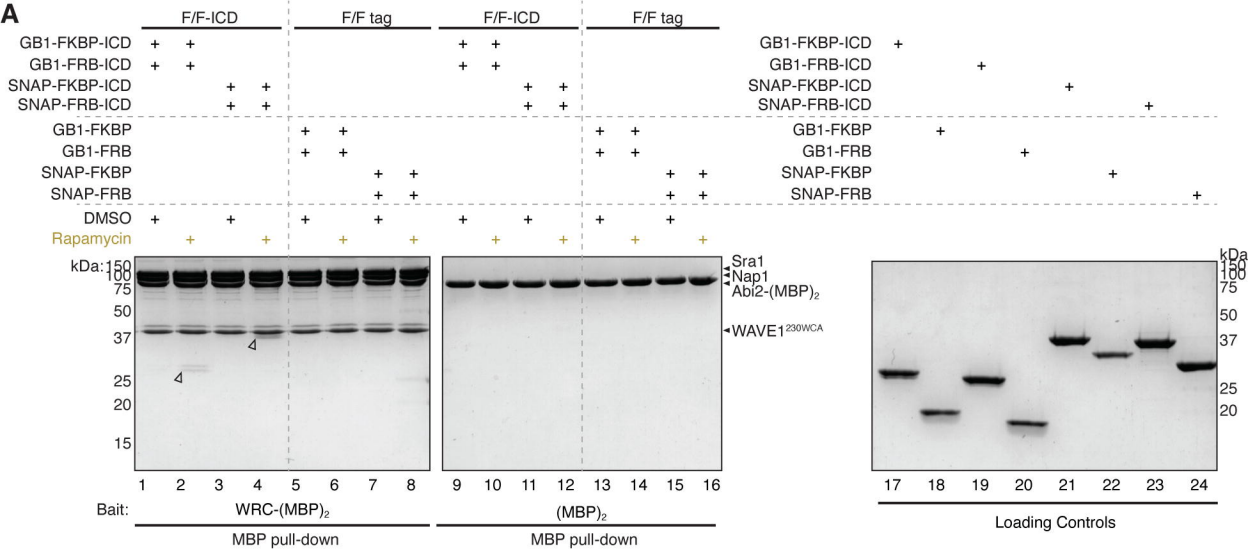
A
F/F-ICD
F/F tag
F/F-ICD
F/F tag
GB1-FKBP-ICD
GB1-FRB-ICD
SNAP-FKBP-ICD
SNAP-FRB-ICD
GB1-FKBP
GB1-FRB
SNAP-FKBP
SNAP-FRB
DMSO
Rapamycin
kDa:
150
100
75
50
37
25
20
15
Sra1
Nap1
Abi2-(MBP)2
WAVE1230WCA
1 2 3 4 5 6 7 8 9 10 11 12 13 14 15 16
Bait:
WRC-(MBP)2
(MBP)2
MBP pull-down
MBP pull-down
17 18 19 20 21 22 23 24
Loading Controls

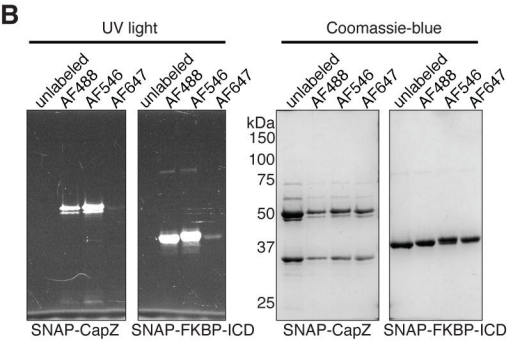
B
UV light
Coomassie-blue
unlabeled
AF488
AF546
AF647
kDa
150
100
75
50
37
25
SNAP-CapZ
SNAP-FKBP-ICD
SNAP-CapZ
SNAP-FKBP-ICD

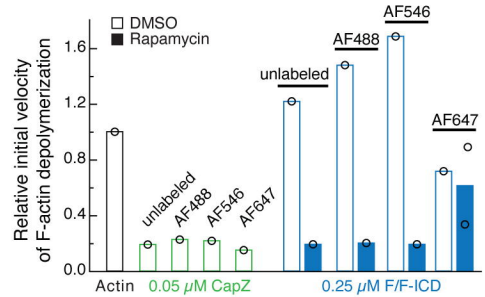
C
DMSO
Rapamycin
Relative initial velocity of F-actin depolymerization
1.6
1.2
0.8
0.4
0.0
unlabeled
AF488
AF546
AF647
Actin
0.05 μM CapZ
0.25 μM F/F-ICD

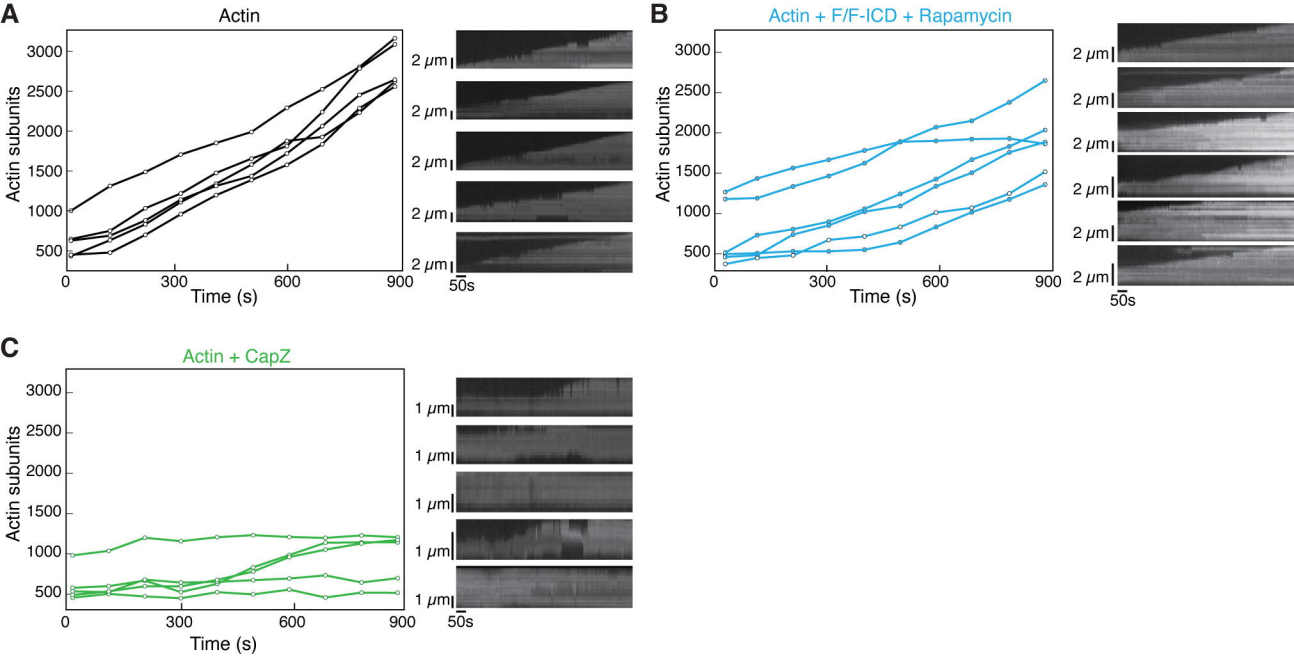
A
Actin
Actin subunits
3000
2500
2000
1500
1000
500
0
300
600
900
Time (s)
2 μm
50s
B
Actin + F/F-ICD + Rapamycin
Actin subunits
Time (s)
2 μm
50s
C
Actin + CapZ
Actin subunits
Time (s)
1 μm
50s

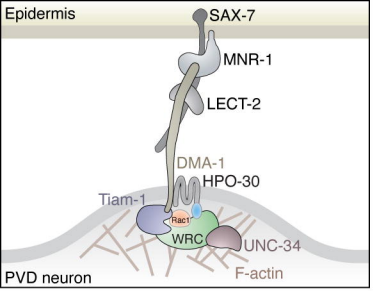
Epidermis
SAX-7
MNR-1
LECT-2
DMA-1
HPO-30
Tiam-1
Rac1
WRC
UNC-34
F-actin
PVD neuron

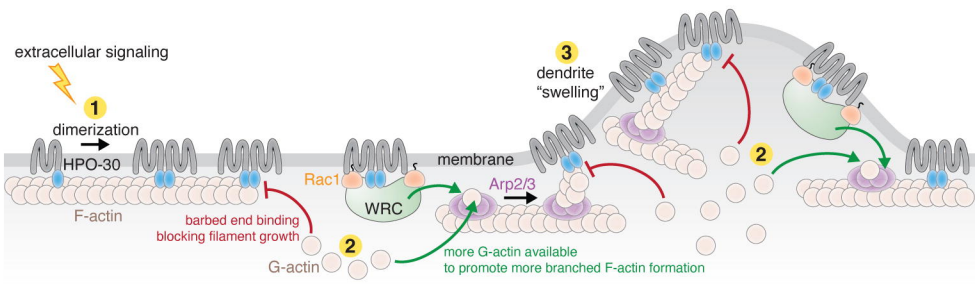
extracellular signaling
1
dimerization
HPO-30
F-actin
barbed end binding
blocking filament growth
membrane
Rac1
WRC
Arp2/3
2
G-actin
more G-actin available
to promote more branched F-actin formation
3
dendrite
"swelling"
2